

New Advances in Phonons: From Band Topology to Quasiparticle Chirality

Tiantian Zhang*

*Institute of Theoretical Physics,
Chinese Academy of Sciences, Beijing 100190,
China*

Yizhou Liu†

*School of Physics Science and Engineering,
Tongji University,
Shanghai 200092,
China*

Hu Miao‡

*Materials Science and Technology Division,
Oak Ridge National Laboratory,
Oak Ridge, TN 37830,
USA*

Shuichi Murakami§

*Department of Applied Physics,
University of Tokyo,
7-3-1 Hongo, Bunkyo-ku,
Tokyo 113-8656,
Japan
International Institute for Sustainability with Knotted Chiral Meta Matter (WPI-SKCM²),
Hiroshima University,
Hiroshima, 739-8526,
Japan*

Phonons, the quantized vibrational modes of a crystal lattice, are ubiquitous quasiparticles in solid-state systems. They play a central role in a wide range of physical phenomena, from thermal transport—as primary carriers of heat in insulators—to their involvement in symmetry-breaking orders such as charge density waves and superconductivity. Traditionally considered as spinless bosons, phonons have recently emerged as a fertile ground for exploring topological physics, spurred by the rapid development of topological band theory initially formulated for fermionic systems. It is now understood that the phonon eigenstates, characterized by their eigenvalues and eigenvectors, can carry nontrivial topological invariants such as Berry curvature and Chern numbers, despite the absence of spin or charge. This new understanding opens up avenues to investigate the interplay between lattice dynamics, topology, and chirality in bosonic systems. In this article, we provide a comprehensive review of recent theoretical and experimental advances in the field of topological and chiral phonons. We begin by introducing the foundational concepts, including the classification of phononic band structures, symmetry-protected topological phases, and the definition of topological invariants in bosonic systems. Special attention is given to the concept of phonon angular momentum and its fundamental connection to Weyl phonons in inversion-symmetry-breaking systems. We then discuss key experimental realizations of topological and chiral phonons across a variety of material platforms. Finally, we outline outstanding challenges and promising directions for future research, such as the role of topology in phonon-mediated quasiparticle interactions and the manipulation of phonon angular momentum in quantum technologies.

CONTENTS

I. Phonons: Theoretical Basis and Experimental Probes	3
A. A Brief Overview of Lattice Dynamics	3
B. Phonon Dynamical Structure Factor	4

C. Experimental Probes	5
1. Raman and Infrared Spectroscopy	5
2. Inelastic x-ray and Neutron Scattering	6
3. Resonant Inelastic x-ray Scattering	6
4. Momentum Resolved Electron Energy Loss Spectroscopy	7
5. Other Techniques	7

II. Topological Phonons: General Topological Band Theory	7
A. Topological Classifications in <i>Gapped</i> Phonon Bands	7
B. Topological Classifications in <i>Gapless</i> Phonon Bands	9
1. Dirac and Weyl Phonons	9
2. Unconventional Weyl Phonons	11
3. Unconventional Dirac Phonons	12

* ttzhang@itp.ac.cn

† yizhouliu@tongji.edu.cn

‡ miaoh@ornl.gov

§ murakami@ap.t.u-tokyo.ac.jp

4. Node-line Phonons	14
C. Diagnosing Topological Phonons at Generic Momenta	14
1. Symmetry-based Indicators for Nodal-line Phonons	16
2. Symmetry-based Indicators for Weyl Phonons	16
D. Comparison Between Different Topological Quasi-particles	17
III. Examples of Topological Phonons: 1D and 2D Lattice Models	17
A. Topological Phonons in 1D: Su-Schrieffer-Heeger Model	18
B. Topological Phonons in 2D: Honeycomb Lattice Model	19
C. Quantum Hall Family of Phonons	20
1. Phononic Quantum <i>Anomalous</i> Hall (QAH)-like States	20
2. Phononic Quantum <i>Valley</i> Hall (QVH)-like States	21
3. Phononic Quantum <i>Spin</i> Hall (QSH)-like States	22
D. Phononic Stiefel-Whitney Insulator	22
IV. Examples of Topological Phonons: 3D Bulk Materials	23
A. Topological Phonons with 0D Degeneracies	23
1. B-20 Type Materials: Double Weyl Phonons	24
2. Face-centered Silicon: Triple Point Phonon	25
3. Body-centered Silicon: \mathbb{Z}_2 Dirac Phonon	27
B. Topological Phonons with 1D Degeneracies	27
C. Obstructed Atomic Insulator-like Topological Phonons	29
D. Topological Phonon Materials Database	30
V. From Topological Phonons to Chiral Phonons	31
A. Basic Concepts Related to Chiral Phonons	31
1. Phonon Angular Momentum	31
2. Phonon Helicity	32
3. Phonon Pseudo-angular Momentum	33
B. Angular Momentum <i>v.s.</i> Pseudo-angular Momentum	33
C. Connections between Topological Phonon & Chiral Phonon	34
1. Weyl Phonons are Both Topological and Chiral	34
2. Diagnosing Weyl Phonons by Pseudo-angular Momentum	34
3. Weyl Phonons are Typical Chiral Phonons: Te As an Example	35
VI. Experimental Progresses of Topological and Chiral Phonons	37
A. Topological Phonons	37
1. Topological Phonons Observed by IXS and INS	37
2. Topological Phonons Observed by EELS	38
B. Chiral Phonons	39
1. Experimental Signature of Phonon PAM	39
2. Experimental Evidence of Chiral Phonons Coupled with Magnetism	40
VII. Conclusions and Perspectives	42
VIII. Acknowledgements	43
References	43

The term “phonon” originates from the Greek word “phonē”, meaning sound or voice (Kojevnikov, 2004). This naming convention reflects the wave-particle duality, akin to “photon” in the context of light waves. In condensed matter physics, phonons are ubiquitous lattice excitations that play a key role in thermal properties of crystalline materials and critical for emergent electronic orders such as superconductivity and charge density waves. However, unlike electrons—which possess a variety of intrinsic degrees of freedom, including charge, spin, and orbital character (as illustrated in Fig. 1)—phonons are traditionally considered to have limited tunability. This intrinsic limitation has historically hindered their active manipulation in physical processes and applications.

In recent years, inspired by conceptual advances in topology and chirality of electronic quantum states—such as topological insulators (Hasan and Kane, 2010; Moore, 2010; Qi

and Zhang, 2010a), superconductors (Ando and Fu, 2015; Qi and Zhang, 2011; Sato and Ando, 2017), and semimetals (Armitage *et al.*, 2018; Lv *et al.*, 2021; Yan and Felser, 2017)—there has been a renewed interest in understanding phonons and their interactions with electronic excitations. Fundamentally, bulk band topology is characterized by topological invariants, such as the Berry phase and Chern number, which are defined on single-particle Bloch wave functions through Berry connection and Berry curvature (Berry, 1984; Thouless *et al.*, 1982a). Importantly, the framework of topological band theory is not exclusive to fermionic quasi-particles—it is equally applicable to bosonic excitations, such as phonons and magnons, provided the system adheres to periodicity and satisfies the conditions of Bloch’s theorem.

A key milestone was achieved in 2008, when Haldane and Raghu extended topological band theory to photonic crystals, proposing an electromagnetic analogue of the quantum Hall effect (Haldane and Raghu, 2008; Raghu and Haldane, 2008), thereby establishing the first realization of non-interacting topological states in a bosonic system. The notion of topological phonons was subsequently introduced by Prodan in 2009, who demonstrated that nontrivial phononic Chern numbers can give rise to topologically protected edge modes—providing a novel mechanism to understand the dynamical instability of microtubules (Prodan and Prodan, 2009a). Later theoretical studies revealed that a nonzero phononic Chern number can arise in systems with broken time-reversal symmetry (Sheng *et al.*, 2006; Zhang *et al.*, 2010) or broken spatial inversion symmetry (Zhang *et al.*, 2018a). These foundational insights paved the way for experimental realizations of topological phononic states across a wide range of platforms, including acoustic metamaterials (Ma *et al.*, 2019a; Xue *et al.*, 2022), complex mechanical lattices (Süsstrunk and Huber, 2016), and crystalline solids (Li *et al.*, 2021a, 2023a; Liu *et al.*, 2022; Miao *et al.*, 2018; Zhang *et al.*, 2023b, 2018a, 2020b).

Although the development of topological phononics was initially inspired by advances in topological electronics, it should not be viewed as a straightforward or trivial extension. From a theoretical standpoint, phonons and electrons are governed by fundamentally different equations of motion. Phonons—manifesting as lattice vibrations—obey Newton’s second law, which involves a second-order time derivative, whereas electrons follow the Schrödinger equation, which is first-order in time. This fundamental difference makes the formulation of geometric phases for phonons less straightforward than for electrons (Berry, 1984). On the practical side, phonons are the primary carriers of heat in semiconductors and insulators, where electronic contributions to thermal transport are minimal or absent. The unique advantages of topological phonon modes—such as robust, defect-immune edge or surface transport channels—open promising avenues for next-generation phononic devices. In particular, they hold potential for information processing applications that require efficient thermal management and rapid heat dissipation.

In parallel with the development of topological phonons,

chiral phonons, which are circularly polarized phonons with finite angular momentum (Bermudez *et al.*, 2008; Kagan and Maksimov, 2008; Komiyama and Murakami, 2021; Lin *et al.*, 1985; McLellan, 1988; Rebane, 1983; Schaack, 1976; Zhang and Niu, 2015; Zhu *et al.*, 2018), have also emerged as a rapidly expanding field of research, attracting significant interest in both microelectronics and quantum information science. Traditionally, phonons have been considered spinless quasiparticles carrying zero angular momentum. However, recent theoretical and experimental breakthroughs have overturned this long-standing assumption, demonstrating that phonons can indeed possess a finite angular momentum and pseudo-angular momentum under certain symmetry conditions. These modes have been shown to drive a variety of exotic physical phenomena, including circularly polarized Raman scattering (Che *et al.*, 2024; Ishito *et al.*, 2023a,b; Zhang *et al.*, 2025a, 2023b, 2025b), circular infrared absorption (Yang *et al.*, 2024b; Zhu *et al.*, 2018), nonreciprocal thermal conductivity (Chen *et al.*, 2020, 2022; Grisson-nanche *et al.*, 2020, 2019; Kasahara *et al.*, 2018; Li *et al.*, 2020d, 2023b; Ohe *et al.*, 2024; Qin *et al.*, 2012; Zhang *et al.*, 2019c), and even spin Seebeck effects (Fransson, 2023; Fu *et al.*, 2019; Kim *et al.*, 2023; Li *et al.*, 2024; Yao and Murakami, 2025). Furthermore, the studies of phonon wavefunctions, which describe collective atomic displacements in real space, have revealed deep connections between topological and chiral phonons (Zhang *et al.*, 2023b, 2025b).

That said, the interpretation of certain experimentally observed phenomena attributed to topological and chiral phonons remain the subject of active debate. In some cases, a careful re-evaluation is necessary to ensure that the interpretations are fully consistent with the underlying physical mechanisms. In this article, we aim to give an overview of theoretical and experimental progresses on topological and chiral phonons in crystalline materials, whose energy spectrum spans from zero to tens of Terahertz. The structure of this review is organized below: Section I will briefly overview theoretical and experimental foundations of phonons in crystalline materials. Section II will introduce topological band theory and topological phonons in 3D. Section III will focus on topological phonons in low-dimensions. Topological phonons in realistic materials will be discussed in Section IV. Section V introduce phonon (pseudo-)angular momentum and consequences of the (pseudo-)angular momentum conservation. We will also introduce the distinctions between two key concepts for chiral phonons in detail, *e.g.*, angular momentum and pseudo-angular momentum. The fundamental connection between topological phonons and chiral phonons will also be discussed. Parallel progress in experimental explorations on topological phonons and chiral phonons will be selected reviewed in Sec. VI. We will close the article with theoretical and experimental perspectives on topological and chiral phonons in Sec. VII.



Figure 1 Comparison between electrons and phonons. Electrons have multiple degrees of freedom, such as charge, spin, orbital, etc. Thus, electrons can be modulated by external fields (*e.g.*, electric fields and magnetic fields) and thereby realizing relevant applications like spin devices. However, phonons are charge neutral, and are traditionally considered to be spin zero and orbital free. Therefore, new degrees of freedom are needed to be introduced to effectively modulate relevant physical properties.

I. PHONONS: THEORETICAL BASIS AND EXPERIMENTAL PROBES

In this section, we describe non-interacting phonons within the framework of the harmonic approximation. Our focus is on physical observables that related to experimental measurements. We will introduce material examples in both Secs. IV and V to illustrate the experimental observation on topological phonons and chiral phonons.

A. A Brief Overview of Lattice Dynamics

Phonons are ubiquitous quasiparticles describing the collective motions of the underlying lattice. The lattice Hamiltonian can be written as the sum of kinetic and potential energy. For simplicity, here we consider a system with only one atom in the unit cell (Kittel and McEuen, 2018):

$$\mathcal{H} = \frac{1}{2} \sum_{i,\alpha} M \dot{u}_i^\alpha \dot{u}_i^\alpha + \frac{1}{2} \sum_{i,\alpha} \sum_{j,\beta} \frac{\partial^2 \Psi}{\partial u_i^\alpha \partial u_j^\beta} \bigg|_0 u_i^\alpha u_j^\beta, \quad (1)$$

where u_i^α represents atomic displacement away from its time-averaged equilibrium position; i and $\alpha = x, y, z$ are labels of unit cell and vibrating degree of freedom, respectively. M is the atomic mass. The Taylor expansion of the potential energy, $\Psi(\mathbf{u})$ follows

$$\Psi(\mathbf{u}) = \Psi(\mathbf{0}) + \sum_{i,\alpha} \Psi_i^\alpha u_i^\alpha + \frac{1}{2} \sum_{i,\alpha} \sum_{j,\beta} \Psi_{ij}^{\alpha\beta} u_i^\alpha u_j^\beta + O(\mathbf{u}^3), \quad (2)$$

where $\Psi(\mathbf{0})$ is the potential energy at zero atomic displacements. Since we assume the lattice is in the equilibrium condition, the atomic force acting on i -th atom should be zero, *i.e.* $\Psi_i^\alpha = -\frac{\partial \Psi}{\partial u_i^\alpha} \bigg|_0 = 0$. Under the harmonic approximation, only the second-order force constants $\Psi_{ij}^{\alpha\beta} = \frac{\partial^2 \Psi}{\partial u_i^\alpha \partial u_j^\beta} \bigg|_0$ are considered.

The lattice dynamics described by Eq. (1) can be obtained by solving the eigenvalue problem:

$$\det|D(\mathbf{q}) - \omega^2 I_{3 \times 3}| = 0, \quad (3)$$

where $I_{3 \times 3}$ is the identity matrix, and $D(\mathbf{q})$ is the dynamical matrix. The matrix elements of $D(\mathbf{q})$ can be written as:

$$D_{\alpha\beta}(\mathbf{q}) \equiv \frac{1}{M} \sum_i \Psi_{ij}^{\alpha\beta} e^{-i\mathbf{q} \cdot (\mathbf{R}_i - \mathbf{R}_j)}, \quad (4)$$

where \mathbf{R}_i is the position vector of the unit cell containing the i -th atom. Since we considered the system with only one atom in a unit cell, Eq. (3) gives rise to three orthogonal eigenvectors, $\epsilon_{q\sigma}$, and eigenvalues, $\omega_\sigma(\mathbf{q})$ ($\sigma = 1, 2, 3$). All three modes are acoustic phonons. The atomic dynamics are superposition of the 3 normal modes:

$$\mathbf{u}_i^\alpha = \frac{1}{\sqrt{NM}} \sum_{\mathbf{q}, \sigma} \epsilon_{q\sigma}^\alpha X_{q\sigma} e^{i\mathbf{q} \cdot \mathbf{R}_i}, \quad (5)$$

where $X_{q\sigma}$ is the normal coordinates. Equation (1) can then be written in the normal coordinates as:

$$\begin{aligned} \mathcal{H} &= \frac{1}{2} \sum_{\mathbf{q}, \sigma} [\dot{X}_{q\sigma}^* \dot{X}_{q\sigma} + \omega_\sigma^2(\mathbf{q}) X_{q\sigma}^* X_{q\sigma}] \\ &= \frac{1}{2} \sum_{\mathbf{q}, \sigma} [P_{q\sigma}^* P_{q\sigma} + \omega_\sigma^2(\mathbf{q}) X_{q\sigma}^* X_{q\sigma}], \end{aligned} \quad (6)$$

where $P_{q\sigma}$ is the canonical momentum. Introducing phonon creation and annihilation operators:

$$a_{q\sigma}^\dagger = \sqrt{\frac{\omega_\sigma(\mathbf{q})}{2\hbar}} \left(X_{-q\sigma} + \frac{P_{q\sigma}}{i\omega_\sigma(\mathbf{q})} \right), \quad (7)$$

$$a_{q\sigma} = \sqrt{\frac{\omega_\sigma(\mathbf{q})}{2\hbar}} \left(X_{q\sigma} - \frac{P_{-q\sigma}}{i\omega_\sigma(\mathbf{q})} \right), \quad (8)$$

and using the commutation relation $[P_{q\sigma}, X_{q'\sigma'}] = -i\hbar \delta_{\sigma\sigma'} \delta_{\mathbf{q}\mathbf{q}'}$, one derives:

$$H = \sum_{\mathbf{q}, \sigma} \left(a_{q\sigma}^\dagger a_{q\sigma} + \frac{1}{2} \right) \hbar \omega_\sigma(\mathbf{q}). \quad (9)$$

The above formalism can be generalized to n -atoms within a unit cell. In this case, there will be $3n$ eigenvectors and eigenvalues. Among the $3n$ phonon modes, 3 of them are acoustic phonons and the rest $3n - 3$ modes are optical phonons. The three acoustic modes have zero frequency at Γ ($\mathbf{q} = 0$) because of the acoustic sum rule $\sum_j \Psi_{ij}^{\alpha\beta} = 0$ which results from the translational invariance of the whole lattice potential energy.

When considering anharmonic effects in a crystal lattice, the traditional harmonic approximation for phonons is no longer sufficient, and corrections must be introduced to account for the interactions between phonons. Anharmonicity arises due to the deviation of atomic potentials from perfect quadratic forms, leading to phonon-phonon scattering, thermal expansion, and temperature-dependent phonon frequencies. These effects can significantly alter the phonon dispersion relations, lifetimes, and thermal properties of materials.

To incorporate anharmonic corrections, one common approach is to use perturbation theory, where the anharmonic terms in the potential energy are treated as perturbations to the harmonic Hamiltonian. This leads to shifts in phonon frequencies (self-energy corrections) and finite phonon lifetimes due to decay processes such as three-phonon and four-phonon interactions. Additionally, anharmonic effects lead to temperature-dependent behavior in phonon properties. For example, the phonon frequency softens with increasing temperature due to lattice expansion and enhanced phonon-phonon interactions. These corrections are crucial for accurately predicting thermal conductivity, specific heat, and other thermodynamic properties of materials at finite temperatures. Advanced computational methods, such as density functional theory (DFT) combined with anharmonic lattice dynamics or molecular dynamics simulations, are often employed to capture these effects quantitatively. In the following, we will ignore the anharmonic effects since they usually do not influence the topological properties of phonons.

B. Phonon Dynamical Structure Factor

Experimentally, the direct physical measurable quantity is the phonon dynamical structure factor, $S(\mathbf{Q}, \omega)$, which is determined by the charge density correlation function (Hansen and Klein, 1976):

$$S(\mathbf{Q}, \omega) = \frac{1}{2\pi\hbar} \int_{-\infty}^{\infty} e^{-i\omega t} \langle \rho(\mathbf{Q}, 0) \rho^\dagger(\mathbf{Q}, t) \rangle dt, \quad (10)$$

$$\rho(\mathbf{Q}, t) = \sum_i f_i(\mathbf{Q}) e^{-i\mathbf{Q} \cdot \mathbf{x}_i(t)}, \quad (11)$$

where $f_i(\mathbf{Q})$ and $\mathbf{x}_i(t)$ are the atomic form factor and time-dependent position of atom i , respectively.

In crystalline materials with periodic condition, the charge operator can be written as:

$$\rho(\mathbf{Q}, t) = \sum_l \sum_i f_i(\mathbf{Q}) e^{-i\mathbf{Q} \cdot [\mathbf{R}_l + \mathbf{r}_i + \mathbf{u}_{l,i}(t)]}, \quad (12)$$

where l represents the primitive cell index, and i labels different atoms within the unit cell. The equilibrium position is given by $\mathbf{x}_0 = \mathbf{R}_l + \mathbf{r}_i$ and $\mathbf{u}_{l,i}(t)$ is the atomic displacement. The dynamical structure factor can then be written as:

$$S(\mathbf{Q}, \omega) = \frac{N_l}{2\pi\hbar} \sum_l e^{i\mathbf{Q} \cdot \mathbf{R}_l} \sum_{i,j} f_i(\mathbf{Q}) f_j^*(\mathbf{Q}) e^{-i\mathbf{Q} \cdot (\mathbf{r}_i - \mathbf{r}_j)} \int_{-\infty}^{\infty} e^{-i\omega t} \langle e^{-i\mathbf{Q} \cdot \mathbf{u}_{l',j}(0)} e^{i\mathbf{Q} \cdot \mathbf{u}_{l,i}(t)} \rangle dt. \quad (13)$$

Under harmonic approximation, the Baker-Hausdorff theorem gives:

$$\langle e^{-i\mathbf{Q} \cdot \mathbf{u}_{l',j}(0)} e^{i\mathbf{Q} \cdot \mathbf{u}_{l,i}(t)} \rangle = e^{-\frac{1}{2} \langle |\mathbf{Q} \cdot \mathbf{u}_{l',j}|^2 \rangle} e^{-\frac{1}{2} \langle |\mathbf{Q} \cdot \mathbf{u}_{l,i}|^2 \rangle} \cdot e^{\langle (\mathbf{Q} \cdot \mathbf{u}_{l',j}(0)) (\mathbf{Q} \cdot \mathbf{u}_{l,i}(t)) \rangle}. \quad (14)$$

We introduce the Debye-Waller factor, $W_l \equiv \frac{1}{2} \langle |\mathbf{Q} \cdot \mathbf{u}_{li}|^2 \rangle \approx \frac{3\hbar^2 |\mathbf{Q}|^2}{2M\beta(k_B\Theta_D)^2}$, where Θ_D is the Debye temperature and $\beta = 1/k_B T$, and define $U \equiv (\mathbf{Q} \cdot \mathbf{u}_{l',j}(0))$, $V \equiv (\mathbf{Q} \cdot \mathbf{u}_{l,i}(t))$. We then obtain:

$$\langle e^{-i\mathbf{Q} \cdot \mathbf{u}_{l',j}(0)} e^{i\mathbf{Q} \cdot \mathbf{u}_{l,i}(t)} \rangle = e^{-W_l} e^{-W_{l'}} (1 + \langle UV \rangle + \langle UV \rangle^2 + \dots). \quad (15)$$

We note that $\langle UV \rangle^n$ is corresponding to the n^{th} order of phonon occupation number $\langle n_{\mathbf{q}\sigma} \rangle$. The phonon dynamical structure factor can thus be expanded as:

$$S(\mathbf{Q}, \omega) = S(\mathbf{Q}, \omega)_{0p} + S(\mathbf{Q}, \omega)_{1p} + S(\mathbf{Q}, \omega)_{2p} + \dots \quad (16)$$

The elastic zero-phonon and inelastic single-phonon terms can respectively be derived as:

$$S(\mathbf{Q}, \omega)_{0p} = N_l^2 \left| \sum_l f_l(\mathbf{Q}) e^{-W_d} e^{i\mathbf{Q} \cdot \mathbf{r}_l} \right|^2 \delta_{\mathbf{Q}=\mathbf{G}} \delta(\hbar\omega), \quad (17)$$

$$S(\mathbf{Q}, \omega)_{1p} = N_l \sum_{\mathbf{q}, \sigma} \frac{1}{\omega_{\sigma}(\mathbf{q})} \left| \sum_i \frac{f_i(\mathbf{Q})}{\sqrt{2M_i}} e^{-W_d} \mathbf{Q} \cdot \mathbf{e}_{\mathbf{q}\sigma} e^{i\mathbf{Q} \cdot \mathbf{r}_i} \right|^2 \delta_{\mathbf{Q}-\mathbf{q}=\mathbf{G}} [\langle n_{\mathbf{q}\sigma} + 1 \rangle \delta(\omega - \omega_{\mathbf{q}\sigma}) + \langle n_{\mathbf{q}\sigma} \rangle \delta(\omega + \omega_{\mathbf{q}\sigma})], \quad (18)$$

where \mathbf{G} is the reciprocal lattice vector and \mathbf{q} is the reduced wave vector in the first Brillouin zone. Using Eq. (18), $S(\mathbf{Q}, \omega)$ can be calculated from first-principles calculations to compare directly with various experimental probes described below. Therefore, it is possible to extract not only the eigenvalues of the dynamical matrix, which correspond to the phonon frequencies, but also the eigenvectors, which are directly related to the intensity of the scattering function $S(\mathbf{Q}, \omega)$.

C. Experimental Probes

Phonons can be probed, directly or indirectly, by absorption and scattering techniques. In this section, we provide a concise overview of spectroscopic techniques. For readers seeking in-depth information on instrumental setups and theoretical foundations, we recommend referring to specialized reviews and literature focused on specific technique.

1. Raman and Infrared Spectroscopy

Raman and infrared (IR) spectroscopy are two well-known methods to probe lattice dynamics with nearly zero momentum transfer (Basov and Timusk, 2005; Devereaux and Hackl, 2007). As we shall see, these techniques have opposite and complementary selection rules, and must be used in combination to measure all phonon modes near the Brillouin zone center.

The physical principle underlying IR spectroscopy is shown in Fig. 2(a). This technique involves measuring the absorption or reflection of IR radiation. Strong IR absorption occurs when the charge oscillations induced by the optical field resonate with lattice vibrations. Since the electrical dipole moment generated by these charge oscillations is parity-odd, only phonon modes with odd parity are IR-active.

In contrast, Raman scattering is a “photon-in-photon-out” scattering process, as depicted in Fig. 2(b). It measures the change in wavelength of light as a phonon is either created or annihilated (Devereaux and Hackl, 2007). Raman scattering involves a change in the polarizability of the crystals. The light-induced dipole moment is:

$$\mathbf{u} = \tilde{\alpha} \cdot \mathbf{E}_i \cos(\mathbf{k}_0 \cdot \mathbf{r} - \omega_0 t), \quad (19)$$

where $\tilde{\alpha}$, a second rank symmetric tensor, is the Raman polarizability tensor. Since the inelastic scattering of the incident light \mathbf{E}_i can excite atomic vibrations, the polarizability tensor has frequency-dependent contributions at the vibration frequencies:

$$\tilde{\alpha} = \tilde{\alpha}_0 + \sum_{\sigma, \mathbf{q}} X_{\mathbf{q}\sigma} \tilde{\alpha}_{\mathbf{q}\sigma} \cos(\mathbf{q} \cdot \mathbf{r} - \omega_{\mathbf{q}\sigma} t). \quad (20)$$

So that

$$\mathbf{u} = \tilde{\alpha}_0 \cdot \mathbf{E}_i \cos(\mathbf{k}_0 \cdot \mathbf{r} - \omega_0 t) + \sum_{\mathbf{q}, \sigma} X_{\mathbf{q}, \sigma} \tilde{\alpha}_{\mathbf{q}\sigma} \cdot \mathbf{E}_i \cos[(\mathbf{k}_0 \pm \mathbf{q}) \cdot \mathbf{r} - (\omega \pm \omega_{\mathbf{q}\sigma}) t]. \quad (21)$$

In Eq. (21), the $+\omega$ and $-\omega$ photon frequency shifts are known as Stokes and anti-Stokes process in the Raman scattering, respectively. For centrosymmetric materials, since both \mathbf{u} and \mathbf{E} are parity-odd, $\tilde{\alpha}_{\sigma}$ must be parity-even to ensure that the Raman-active modes are symmetry-allowed.

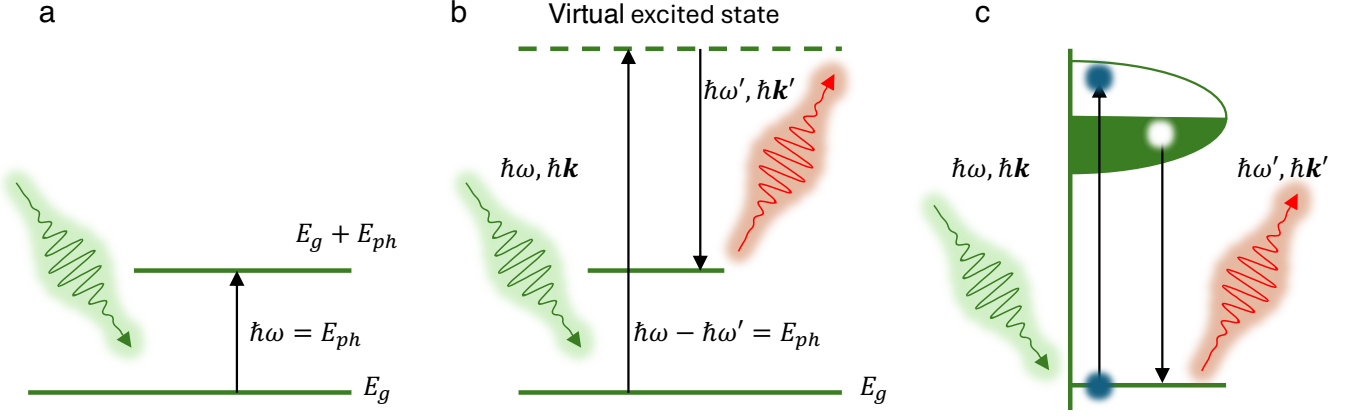


Figure 2 Schematics of photon scattering processes. (a) depicts the IR spectroscopy. When the incident photon energy, $\hbar\omega$, matches the phonon excitation energy, E_{ph} , the incident light will be absorbed, resulting reduced reflection or transmission light intensity. (b) shows the Raman scattering process. The incident photon drives the initial state to a virtual excited state. The system then relax to a final state and emit a photon. Following the energy and momentum conservation, $E_{ph} = \hbar\omega - \hbar\omega'$ and $\mathbf{P}_{ph} = \hbar\mathbf{k} - \hbar\mathbf{k}'$, where $\hbar\mathbf{k}$ and $\hbar\mathbf{k}'$ are incident and scattered photon momentum. (c) illustrates the direct RIXS process. Similar to the Raman scattering, RIXS is also a scattering process. The incident photon energy is tuned to a element specific resonant energy. The core electron is excited to an intermediate state. The core hole is then filled by an electron from the conduction band.

2. Inelastic x-ray and Neutron Scattering

Inelastic x-ray (IXS) and inelastic neutron scattering (INS) are powerful techniques to directly measure the dynamic structure factor $S(\mathbf{Q}, \omega)$ of the bulk phonons across a broad range of energies and momenta (Feigin *et al.*, 1987; Higgins and Maconnachie, 1986; Kotani and Shin, 2001). To begin with, we first introduce the interaction between the photon field and charged particles:

$$\mathcal{H}_I = \frac{e\mathbf{A} \cdot \mathbf{P}}{m} + \frac{e^2 A^2}{2m}. \quad (22)$$

The vector potential \mathbf{A} can be written in photon operators, $b_{u\mathbf{k}}$ and $b_{u\mathbf{k}}^\dagger$, as:

$$\mathbf{A}(\mathbf{r}, t) = \sum_u \sum_{\mathbf{k}} \hat{\epsilon}_u \sqrt{\frac{\hbar}{2\epsilon_0 V \omega_{\mathbf{k}}}} [b_{u\mathbf{k}} e^{i(\mathbf{k} \cdot \mathbf{r} - \omega t)} + b_{u\mathbf{k}}^\dagger e^{-i(\mathbf{k} \cdot \mathbf{r} - \omega t)}], \quad (23)$$

where $\hat{\epsilon}_u$ represents the polarization of the light. In the case of IR spectroscopy, the cross-section is determined by the first term on the right-hand side of Eq. (22), which corresponds to single-photon absorption processes. For Raman scattering, both term contribute to the cross-section. In contrast, for (non-resonant) IXS, the second term dominates the cross-section. The Thomson differential cross-section, for a solid angle $d\Omega$ and energy bandwidth $d\omega$, is given by:

$$\frac{d^2\sigma}{d\Omega d\omega} = \frac{k_f}{k_i} r_0^2 |\hat{\epsilon}_i \cdot \hat{\epsilon}_f|^2 S(\mathbf{Q}, \omega), \quad (24)$$

where i and f denote the initial and final states. $r_0 = \frac{e^2}{mc^2} \sim 2.81$ femtometer (fm) is the classical radius of the electron. For a typical IXS experiment, the energy transfer, ω , is

about 5~6 orders magnitude smaller than the incident photon energy; therefore, $\frac{k_f}{k_i} \sim 1$, and $\frac{d^2\sigma}{d\Omega d\omega} \propto S(\mathbf{Q}, \omega)$.

For INS, incident neutrons interact with atomic nuclei through short-range nuclear forces, which operate within the femtometer length scale. The coherent scattering contribution to the INS cross-section of INS is given by:

$$\frac{d^2\sigma}{d\Omega d\omega} = \frac{\sigma_{coh}}{4\pi} \frac{k_f}{k_i} NS(\mathbf{Q}, \omega). \quad (25)$$

While both IXS and INS are powerful techniques for probing phonon dynamics, they are often complementary in many aspects. For instance, the scattering intensity in IXS approximately scales with Z^2 , where Z is the atomic number, whereas INS displays complex isotope effect. As a result, the choice between the two techniques may depend on the specific chemical elements present in the sample.

In addition, IXS offers higher momentum resolution and the ability to study small-size samples ($\sim 10 \mu\text{m} \times 30 \mu\text{m}$) due to the high brilliance of modern synchrony light source. On the other hand, INS can achieve higher energy resolution and enables the simultaneous collection of data across a large momentum space using time-of-flight spectrometer.

3. Resonant Inelastic x-ray Scattering

Resonant inelastic x-ray scattering (RIXS) is a photon scattering technique that has seen remarkable advancements over the past decade. RIXS is a two-step process involving photoelectric absorption and emission. As shown in Fig. 2(c), a core electron absorbs a photon and is excited into the valence band. This intermediate excited state then decays by emitting an x-ray photon. Due to its resonant nature, RIXS is described

by the Kramers-Heisenberg cross-section (Ament *et al.*, 2011; Healy, 1977), in contrast to the Thompson cross-section used for non-resonant IXS. Compared to IXS and INS, RIXS is sensitive to a wide range of quantum excitations, including spin, charge, orbital, lattice, and fractional quasiparticles. The intensity distribution in RIXS spectra also provides valuable insights into the strength of quasiparticle interactions. However, the RIXS cross-section is not directly proportional to the phonon dynamical structure factor. Additionally, despite significant progress, the state-of-the-art energy resolution of RIXS remains on the order of 20 meV, making it challenging to quantitatively analyze the phonon dynamical structure factor.

4. Momentum Resolved Electron Energy Loss Spectroscopy

IXS and INS are generally bulk sensitive probes due to the deep penetration depth of hard x-rays and neutrons. For the interests in 2D materials and topological surface state, IXS and INS are limited by the small total scattering volume. To address this, high-resolution momentum resolved electron energy loss spectroscopy (HR-MEELS) has been developed as a powerful tool for investigating charge and phonon correlation functions on the surface (Brydson, 2020; Egerton, 2011; Ibach and Mills, 2013). Unlike the transmission EELS, MEELS experiments are typically conducted in reflection geometry with incident electron energy, E_i , less than 200 eV. By setting $E_i=7.4$ eV, energy and momentum resolutions that are better than 1 meV and 0.002\AA^{-1} have been achieved, making MEELS a highly effective techniques for probing charge excitations in 2D materials. For electron scattering with small momentum transfer, \mathbf{q} , the HR-MEELS cross section can be formulated as:

$$\frac{d^2\sigma}{d\Omega d\omega} = \sigma_0 V_{\text{eff}}^2(\mathbf{q}) \int_{-\infty}^0 z_1 z_2 e^{-|\mathbf{q}||dz_1+dz_2|} \cdot S(\mathbf{q}, z_1, z_2, \omega), \quad (26)$$

where

$$V_{\text{eff}}(\mathbf{q}) = \frac{4\pi e^2}{q^2 + (k_i^z + k_s^z)^2}. \quad (27)$$

$k_{i,s}^z$ represent the out-of-plane momentum of the incident and scattered electron. As shown in Eq. (26), the HR-MEELS cross-section is closely related to the surface $S(\mathbf{q}, \omega)$.

5. Other Techniques

Numerous other techniques are also sensitive to phonon excitations. For instance, resonant ultrasound spectroscopy probes the quasi-elastic phonon excitations in the MHz range (Migliori, 2016). Additionally, pump-probe and time-domain spectroscopy (Fischer *et al.*, 2016; Fushitani, 2008; Hangyo *et al.*, 2005; Koch *et al.*, 2023), utilizing tabletop laser

setup or advanced free-electron lasers, provide access to coherent optical and acoustic phonons, as well as their interactions with spin and charge excitations. These methods offer versatile tools for exploring the dynamic behavior of phonons and their coupling to other quantum excitations in materials.

II. TOPOLOGICAL PHONONS: GENERAL TOPOLOGICAL BAND THEORY

Topological band theory (TBT) is an extension of traditional band theory that incorporates the principles of topology. It has been widely applied to various condensed matter platforms, including electrons (Bradlyn *et al.*, 2017; Burkov, 2016; Fu and Kane, 2007; Fu *et al.*, 2007; Hasan and Kane, 2010; Lv *et al.*, 2021; Murakami, 2007; Po *et al.*, 2017; Qi and Zhang, 2011; Tang *et al.*, 2019a; Tokura *et al.*, 2019; Vergniory *et al.*, 2019b; Zhang *et al.*, 2019a), phonons (Li *et al.*, 2021b; Liu *et al.*, 2017a, 2018, 2017b; Sheng *et al.*, 2006; Xu *et al.*, 2024b; Zhang *et al.*, 2010, 2018a, 2019b), magnons (McClarty, 2022; Owerre, 2016; Zhang *et al.*, 2013), photons (Lu *et al.*, 2016a, 2014, 2016b; Ozawa *et al.*, 2019), and artificial systems (Huber, 2016a; Imhof *et al.*, 2018; Kane and Lubensky, 2014; Khanikaev and Shvets, 2017; Lu *et al.*, 2015; Luo *et al.*, 2018; Ma *et al.*, 2019b; Nash *et al.*, 2015; Ningyuan *et al.*, 2015; Ssstrunk and Huber, 2015; Wang *et al.*, 2015a; Yang *et al.*, 2015; Zhang *et al.*, 2019d). In this section, we will first introduce the basics of topological classifications of gapped systems, which is not limited to electronic systems with an energy gap near the Fermi energy. Then, we will expand the topological band theory to phonon systems, which is the mainly focus in this review. We emphasize the different topological classifications for gapless and gapped phonon excitations and discuss their corresponding topological invariants under various symmetries. Since phonon excitations generally preserve time-reversal symmetry (\mathcal{T}), our discussion will focus primarily on time-reversal-invariant systems.

A. Topological Classifications in Gapped Phonon Bands

The ‘‘ten-fold way’’ refers to a classification framework in condensed matter physics and quantum field theory, primarily used to categorize symmetry classes of Hamiltonians, particularly in the study of topological insulators (Ando, 2013; Bernevig, 2013; Fu and Kane, 2007; Hasan and Kane, 2010; Hasan and Moore, 2011; Khanikaev *et al.*, 2013; Qi and Zhang, 2011; Shen, 2012; Tokura *et al.*, 2019) and topological superconductors (Ando and Fu, 2015; Leijnse and Flensberg, 2012; Sato and Ando, 2017). Such classification is grounded in the presence or absence of three foundational discrete symmetries, i.e., time-reversal symmetry (\mathcal{T}), particle-hole symmetry (\mathcal{C}), and chiral (or sublattice) symmetry (\mathcal{S}). The idea of the ten-fold way dates back at least to 1996, when (Altland and Zirnbauer, 1997) discovered that substances can

be divided into 10 kinds (Kitaev, 2009; Ryu *et al.*, 2010). Equations ((28)-(30)) provide the mathematical expressions for these three symmetry operators, as well as the transformation properties of the Hamiltonian under these symmetries.

$$\mathcal{T}^{-1}H(k)\mathcal{T} = H(-k), \quad \mathcal{T} = U_T\mathcal{K}, \quad U_T U_T^* = \pm 1, \quad (28)$$

$$\mathcal{C}^{-1}H(k)\mathcal{C} = -H(-k), \quad \mathcal{C} = U_C\mathcal{K}, \quad U_C U_C^* = \pm 1, \quad (29)$$

$$\mathcal{S}^{-1}H(k)\mathcal{S} = -H(k), \quad \mathcal{S} = U_S, \quad U_S^2 = 1. \quad (30)$$

U_T and U_C are unitary matrix, and \mathcal{K} is the complex conjugate operator.

In a system exhibiting time-reversal symmetry (\mathcal{T}), $\mathcal{T}^2 = -1$ or $+1$, corresponding to half-integer spin systems (including spinful electronic systems) and integer-spin systems (e.g phonons and photons), respectively. When the time-reversal symmetry is broken, phenomena like the quantum anomalous Hall effect (QAHE) emerge (Chang *et al.*, 2023, 2013; Deng *et al.*, 2020; Haldane, 1988; Liu *et al.*, 2008, 2016), and this case is symbolically expressed as $\mathcal{T}^2 = 0$ (where “0” signifies the absence of time-reversal symmetry). Similarly, particle-hole symmetry (\mathcal{C}) is characterized by an anti-unitary operator with $\mathcal{C}^2 = \pm 1$, or $\mathcal{C}^2 = 0$ in the absence of particle-hole symmetry, yielding three possible cases. Chiral symmetry (or sublattice symmetry in certain contexts) can be interpreted as a combination of \mathcal{T} and \mathcal{C} ($\mathcal{S} = \mathcal{T}\mathcal{C}$), which also results in three possibilities, with $\mathcal{S}^2 = \pm 1, 0$. Thus, we have identified 9 distinct types of systems by considering the possible values of \mathcal{T}^2 , \mathcal{C}^2 , \mathcal{S}^2 , each of which can take values of -1 , 1 or 0 . This naturally raises the question: what constitutes the tenth kind in the “ten-fold way”? The answer lies in systems that lack both \mathcal{T} and \mathcal{C} individually, yet still exhibit symmetry under their combined operation, $\mathcal{S} = \mathcal{T}\mathcal{C}$. In such systems, invariance is preserved when particles and holes are interchanged and time is reversed, even though neither symmetry exists alone. This unique scenario completes the ten-fold classification.

Cartan label	T	C	S	Hamiltonian	G/H (ferm. NLM)
A (unitary)	0	0	0	$U(N)$	$U(2n)/U(n) \times U(n)$
AI (orthogonal)	+1	0	0	$U(N)/O(N)$	$Sp(2n)/Sp(n) \times Sp(n)$
AII (symplectic)	-1	0	0	$U(2N)/Sp(2N)$	$O(2n)/O(n) \times O(n)$
AIII (ch. unit.)	0	0	1	$U(N+M)/U(N) \times U(M)$	$U(n)$
BDI (ch. orth.)	+1	+1	1	$O(N+M)/O(N) \times O(M)$	$U(2n)/Sp(2n)$
CII (ch. sympl.)	-1	-1	1	$Sp(N+M)/Sp(N) \times Sp(M)$	$U(2n)/O(2n)$
D (BdG)	0	+1	0	$SO(2N)$	$O(2n)/U(n)$
C (BdG)	0	-1	0	$Sp(2N)$	$Sp(2n)/U(n)$
DIII (BdG)	-1	+1	1	$SO(2N)/U(N)$	$O(2n)$
CI (BdG)	+1	-1	1	$Sp(2N)/U(N)$	$Sp(2n)$

Figure 3 “Cartan label” for “ten-fold way” classes of single-particle Hamiltonians H , based on time-reversal symmetry (\mathcal{T}), particle-hole symmetry (\mathcal{C}) and chiral symmetry ($\mathcal{S} = \mathcal{T}\mathcal{C}$). Adapted from Ref. (Ryu *et al.*, 2010).

Up to this point, we have established ten distinct topological classifications based on three symmetries, as illustrated in

Cartan	d											
	0	1	2	3	4	5	6	7	8	9	10	11 ...
<i>Complex case:</i>												
A	\mathbb{Z}	0	\mathbb{Z}	0	\mathbb{Z}	0	\mathbb{Z}	0	\mathbb{Z}	0	\mathbb{Z}	0 ...
AIII	0	\mathbb{Z}	0	\mathbb{Z}	0	\mathbb{Z}	0	\mathbb{Z}	0	\mathbb{Z}	0	\mathbb{Z} ...
<i>Real case:</i>												
AI	\mathbb{Z}	0	0	0	$2\mathbb{Z}$	0	\mathbb{Z}_2	\mathbb{Z}_2	\mathbb{Z}	0	0	0 ...
BDI	\mathbb{Z}_2	\mathbb{Z}	0	0	0	$2\mathbb{Z}$	0	\mathbb{Z}_2	\mathbb{Z}_2	\mathbb{Z}	0	0 ...
D	\mathbb{Z}_2	\mathbb{Z}_2	\mathbb{Z}	0	0	0	$2\mathbb{Z}$	0	\mathbb{Z}_2	\mathbb{Z}_2	\mathbb{Z}	0 ...
DIII	0	\mathbb{Z}_2	\mathbb{Z}_2	\mathbb{Z}	0	0	0	$2\mathbb{Z}$	0	\mathbb{Z}_2	\mathbb{Z}_2	\mathbb{Z} ...
AII	$2\mathbb{Z}$	0	\mathbb{Z}_2	\mathbb{Z}_2	\mathbb{Z}	0	0	0	$2\mathbb{Z}$	0	\mathbb{Z}_2	\mathbb{Z}_2 ...
CII	0	$2\mathbb{Z}$	0	\mathbb{Z}_2	\mathbb{Z}_2	\mathbb{Z}	0	0	0	$2\mathbb{Z}$	0	\mathbb{Z}_2 ...
C	0	0	$2\mathbb{Z}$	0	\mathbb{Z}_2	\mathbb{Z}_2	\mathbb{Z}	0	0	0	$2\mathbb{Z}$	0 ...
CI	0	0	0	$2\mathbb{Z}$	0	\mathbb{Z}_2	\mathbb{Z}_2	\mathbb{Z}	0	0	0	$2\mathbb{Z}$...

Figure 4 “Ten-fold way” table for topological insulators and superconductors as a function of spatial dimension d and three discrete symmetries, such that the symmetry classes are arranged to reveal a periodic pattern in spatial dimensionality. The “Cartan label” (first column) is shown in Fig. 3. These ten classes are subsequently categorized into two groups: the complex and real ones, mainly contingent upon the complexity of the Hamiltonian. \mathbb{Z} and \mathbb{Z}_2 represent the distinct phases within a specific symmetry class of topological insulators/superconductors, distinguished by an integer invariant. Within a specific \mathbb{Z} group, the topological invariant is isomorphic to the \mathbb{Z} -type Abelian group and can assume any integer value. For the \mathbb{Z}_2 class, the topological invariant is isomorphic to the \mathbb{Z}_2 -type Abelian group, such that the topological invariant can take two classes of values, the odd ones and the even ones. “0” means that no topological insulator/superconductor is present, indicating that all quantum ground states are topologically trivial. Adapted from Ref. (Ryu *et al.*, 2010)

Fig. 3. Here, the notation “ ± 1 ” indicates the presence of a symmetry with \mathcal{T}^2 , \mathcal{C}^2 , $\mathcal{S}^2 = +1, -1$, while “0” signifies the absence of the corresponding symmetry. The topological classification is not only determined by these symmetries, but also the dimension of the system. Figure 4 shows the “ten-fold way” table, which incorporates the interplay between different symmetries and system dimensions. Within given symmetries and dimensions, topological classes can be distinguished by a certain Abelian group, such as \mathbb{Z} , \mathbb{Z}_2 , or topologically trivial (labeled by “0”). A closer examination of the table reveals a periodic pattern that repeats every 8 dimensions. Specifically, the behavior of systems in dimension $d = 9$ mirrors that of $d = 1$, and this periodicity continues as the dimensionality increases further.

To gain a deeper understanding of this table, let us consider the topological class for A class with $d = 2$ as an example. This classification falls under the \mathbb{Z} type, which corresponds to systems such as the Chern insulator case (or the QAHE). The topological invariant in this case is defined as the Chern number (Avron *et al.*, 1983; Hatsugai, 1993; Thouless *et al.*, 1982b):

$$C = \frac{1}{2\pi} \int_{\text{BZ}} \Omega(\mathbf{k}) d^2k, \quad (31)$$

where C is the Chern number, $\Omega(\mathbf{k})$ is the Berry curvature, and the integral is taken over the whole Brillouin zone (BZ) in

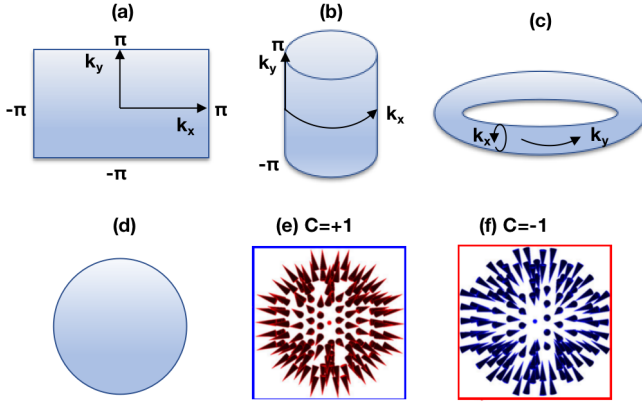


Figure 5 Illustration of the integral curved surface for the Chern number. (a) Depicts a typical Brillouin zone for a two-dimensional system. (b) and (c) Show two configurations of integrated surfaces that are topologically equivalent to the BZ in (a). This equivalence arises due to the periodic boundary conditions of the Brillouin zone, allowing for alternative representations of the integration domain. (d) Illustrates the integrated surface used to calculate the Chern number for Weyl phonons. This surface is typically a sphere enclosing the Weyl phonon, capturing the topological charge associated with it. (e) and (f) display the Berry curvature distributions for Weyl points with Chern numbers $C = +1$ and -1 , respectively. The integration of the Berry curvature over the enclosing surface yields the Chern number, which characterizes the topological nature of the Weyl phonon. (e) and (f) are adapted from Ref. (Weng *et al.*, 2015)

2D systems, as illustrated in Fig. 5 (a). The Chern number can take arbitrary integer values, reflecting the fact that the topological phase may vary across different systems. This variability underscores the richness of topological phases in gapped systems. The classification scheme based on such topological invariants is crucial for understanding the diverse phases of topological matter, enabling the prediction and characterization of novel quantum states.

The “ten-fold way” classification can also be extended to the phonon spectra of solids, where a gap is required in the phonon spectra. Since phonons are bosons, which have $\mathcal{T}^2 = 0, 1$. As a result, topological classifications for gapped phonon systems are restricted to the classes of A, AI, AIII, BDI, D, C, and CI. In condensed matter physics, \mathcal{C} and \mathcal{S} are often difficult to be strictly defined in materials. Therefore, \mathcal{T} plays a central role in determining the topological gapped states for phonons, particularly in the classes of A and AI. Moreover, when crystalline symmetries (such as rotational, mirror, or inversion symmetries) are taken into account, the topological classification of phonon systems becomes significantly richer (Fu, 2011; Kruthoff *et al.*, 2017; Po *et al.*, 2017; Shiozaki and Sato, 2014; Song *et al.*, 2018). These additional symmetries not only expand the range of possible topological phases but also make them easier to identify and diagnose in real materials.

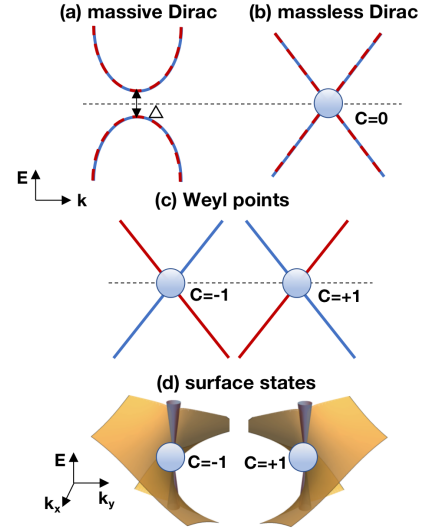


Figure 6 (a) and (b) depict the massive and massless Dirac phonon spectra, respectively. In both cases, the Chern number is zero, indicating the absence of nontrivial topological charge. (c) Weyl phonons with opposite Chern number and chirality. The massless Dirac phonon is composed of two Weyl phonons with $C = \pm 1$. (d) Topological surface states of Weyl phonons are in helicoid shapes. These surface states share the same chirality as the Chern numbers of the corresponding Weyl phonons, highlighting the direct connection between bulk topology and surface topology.

B. Topological Classifications in Gapless Phonon Bands

In contrast to the topological states in gapped phonon spectra, as introduced in the previous subsection, topological phonons in gapless phonon systems have garnered significantly more attention. The classification of topological phonons in gapless systems is primarily based on two key features: the degeneracy of band crossings, which exhibit distinct properties, and their codimension (e.g., point or line nodes). These features are typically protected by symmetry, as shown in Figs. 6 and 11. The interplay between the degeneracy and codimension of these band crossings results in a rich variety of topological phonons (Jin *et al.*, 2022; Li *et al.*, 2021a; Liu *et al.*, 2020b; Miao *et al.*, 2018; Qin *et al.*, 2024; Wang *et al.*, 2022; Yang *et al.*, 2024c; Zhang *et al.*, 2022b, 2023b, 2020a; Zhang and Murakami, 2021, 2023; Zhang *et al.*, 2018a, 2020b, 2019b).

1. Dirac and Weyl Phonons

In particle physics, elementary particles serve as the fundamental building blocks of matter and the universe. The standard model categorizes these particles into three primary categories: quarks, leptons, and gauge bosons (Burgess and Moore, 2007). Dirac fermions play a central role in the standard model of particle physics, encompassing all the known quarks and charged leptons. They are crucial for describing the properties and interactions of these fundamental par-

ticles. Beyond particle physics, Dirac fermions also emerge in condensed matter physics, where they refer to quasiparticles that are governed by the Dirac equation. This equation unites quantum mechanics and special relativity, providing a framework for describing spin- $\frac{1}{2}$ particles.

In the context of condensed matter physics, Dirac phonons are analogous to spinless Dirac fermions in solids. They are described within the framework of band theory, with their universal effective Hamiltonian expressed as:

$$H_D(\mathbf{k}) = \begin{pmatrix} v_0 \boldsymbol{\sigma} \cdot \mathbf{k} & m(\mathbf{k}) \\ m^*(\mathbf{k}) & -v_0 \boldsymbol{\sigma} \cdot \mathbf{k} \end{pmatrix}, \quad (32)$$

where $\boldsymbol{\sigma} = (\sigma_x, \sigma_y, \sigma_z)$ represent the Pauli matrix, $\mathbf{k} = (k_x, k_y, k_z)$ is the crystal momentum vector, v_0 is the group velocity and $m(\mathbf{k})$ is the mass term of the Dirac Hamiltonian. Eigenvalues for Eq. (32) are $E_{\pm}(\mathbf{k}) = \pm \sqrt{m(\mathbf{k})^2 + v_0^2 k^2}$, with each branch of $E_{\pm}(\mathbf{k})$ doubly degenerated in inversion-symmetric systems, as shown by the phonon spectra in Figs. 6 (a) and (b). When $m(\mathbf{k}) = 0$, the Dirac point will be fourfold degenerate and can be decomposed into two Weyl phonons with opposite chirality. The chiral Weyl phonon can be described by:

$$H_{\text{Weyl}}^{\pm}(\mathbf{k}) = v_0 \cdot \begin{pmatrix} k_z & k_x \mp ik_y \\ k_x \pm ik_y & -k_z \end{pmatrix}, \quad (33)$$

where the sign \pm indicates the chirality. For chirality “+” (“-”), the Chern number of a closed surface enclosing the Weyl point is $C_{\pm} = \pm 1$. Thus the nonzero Chern number indicates chirality. In this context, the massless Dirac fermion is achiral due to the vanishing total Chern number $C = 0$. While phonons are analogous to spinless fermions in solids, under certain symmetry the Dirac and Weyl phonons emerge, similar to spin- $\frac{1}{2}$ fermions, as shown in Fig. 6.

The topological invariant for Weyl phonons is defined in a manner analogous to the Chern number, as expressed in Eq. (31). However, instead of integrating over a two-dimensional plane in the Brillouin zone, the integral is performed over a sphere enclosing the Weyl point in three-dimensional momentum space, as shown in Figs. 6 (c) and 5 (a)-(d). Figures 5 (e)-(f) are the Berry curvature distribution on the integral sphere enclosing the Weyl phonon with $C = +1$ and -1 , respectively. When $C \neq 0$, the Weyl phonon exhibits a topological nature, which is closely linked to the emergence of topological surface states. These surface states typically exhibit a helicoid/spiral shape, as illustrated in Fig. 6 (d). The chirality of these surface states follows the sign of the Chern number. Consequently, in systems containing a pair of Weyl phonons, the surface states connecting them display opposite chiralities near each Weyl phonon, as shown in Fig. 7 (a3).

If an isoenergy surface is considered, analogous to the Fermi surface in fermionic systems, a surface arc will emerge in the surface Brillouin zone when a pair of Weyl phonons project onto distinct momenta. This behavior is illustrated in Figs. 7 (a1) and (a2), where the surface arc connects the projections of the Weyl phonons, reflecting their topological na-

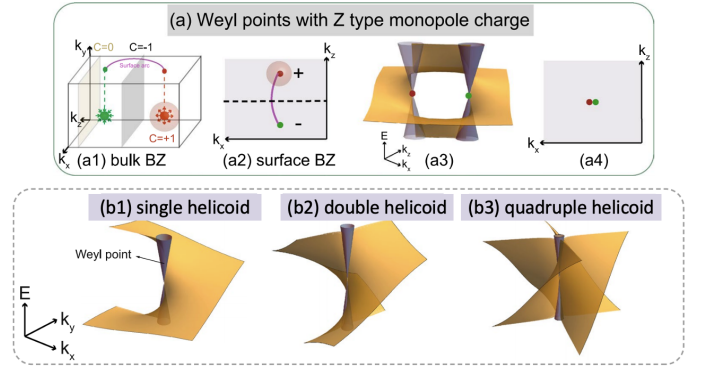


Figure 7 (a) Surface states and surface arcs for Weyl phonons. The Chern number of Weyl phonons can be calculated either on a sphere enclosing the Weyl phonons or the 2D colored plane shown in (a1). In (a2), when two Weyl phonons with opposite chirality project onto different momenta in the surface Brillouin zone (BZ), a surface arc connecting the two Weyl phonons emerges. (a3) depicts the topological surface states linking two Weyl phonons, which exhibit different chiralities near each Weyl phonon. In (a4), when two Weyl phonons with opposite chirality project onto the same momentum in the surface BZ, the surface arc disappears. (b1-b3) Topological surface states for Weyl phonons with Chern number of $C = +1$, $+2$ and $+4$, respectively, all of them are in helicoid/spiral shapes. (a) is adapted from Ref. (Zhang *et al.*, 2022b), (b1)-(b3) are adapted from Ref. (Zhang and Murakami, 2023).

ture. However, if a pair of Weyl phonons with opposite chirality project onto the same momentum in the surface Brillouin zone, the surface arc vanishes, as depicted in Fig. 7 (a4). Consequently, massless Dirac phonons do not exhibit surface arcs, since the two Weyl phonons that constitute a Dirac phonon always map to identical momenta on the surface BZ. This absence of surface arcs is a direct result of the cancellation of chirality and the overlapping projections of the Weyl phonons in the Dirac system.

In Eq. (32), Dirac points are represented using gamma matrices that satisfy the anti-commutation relations of the Clifford algebra. As a result, Dirac points can exhibit two distinct behaviors: they can be massive, associated with a gapped band dispersion, or massless, associated with a gapless band dispersion, depending on the coefficients of the gamma matrices. On the other hand, Eq. (33) involve two bands and are represented using the Pauli matrices. Since the number of the Pauli matrices is three, Weyl points in 3D are topological and robust, as is distinct from the ones in 2D. This feature is common to any particles, such as electrons and phonons.

In 3D systems, Dirac phonons and Weyl phonons can be distinguished by two key features: (1) their band degeneracy and (2) the topological invariant of the system. Dirac phonons are typically topologically trivial due to the combination of two Weyl points with opposite topological charge, while Weyl phonons are characterized by their chiral nature and non-zero topological charge, as reflected in their distinct topological invariants. However, in a special case, Dirac phonons can carry a nonzero monopole charge, known as charge-2 Dirac

phonons (Jin *et al.*, 2022; Miao *et al.*, 2018; Zhang *et al.*, 2018a). This occurs when they are protected by a combination of non-symmorphic symmetries and time-reversal symmetry.

Though conventional Dirac phonons are topologically trivial and do not possess surface states, they play a crucial role as the critical phase that governs topological phase transitions, as emphasized in the electronic systems by Ref. (Murakami, 2007). For example, when $m(\mathbf{k}) \neq 0$, the Dirac point transitions into a massive one, acquiring an energy gap, as shown in Fig. 6 (a). The topology of two massive Dirac systems differs based on the sign of $m(\mathbf{k})$, a consequence of the evolution process, as depicted in Fig. 8. This highlights the significance of Dirac and Weyl phonons as versatile platforms for modulating and exploring a wide range of topological states.

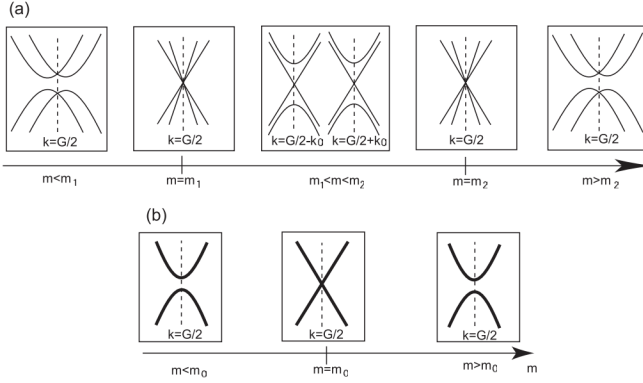


Figure 8 A phase transition can occur between two gapped systems, one topologically nontrivial and the other topologically trivial, by tuning the mass term of the system. This figure shows spin- $\frac{1}{2}$ systems with time-reversal symmetry as an example. The critical point of this transition is marked by a massless Dirac point, which serves as the boundary between the two phases. In Fig. (a), the system lacks inversion symmetry, resulting in non-degenerate bands, while in Fig. (b), the system possesses inversion symmetry, leading to doubly degenerate bands. These scenarios illustrate how symmetry and the mass term influence the topological properties and band structure of the system during the phase transition. The figure is adapted from Ref. (Murakami, 2007).

2. Unconventional Weyl Phonons

In contrast to the real universe, the “material universe” refers to the effective theory of low-energy, long-wavelength excitations in solids. In 2007, (Murakami, 2007) proposed the idea of discovering Weyl fermions, a concept originally from high-energy physics, in condensed matter systems. This groundbreaking idea was later realized in 2015 when (Huang *et al.*, 2015; Weng *et al.*, 2015) independently predicted the existence of Weyl fermions in real materials, a prediction that was experimentally confirmed in TaAs (Huang *et al.*, 2015; Lv *et al.*, 2015a). Building on this, in 2016, (Bradlyn *et al.*, 2016) suggested that crystals could host a variety of “unconventional Weyl fermions” with Chern numbers greater than 1, i.e., $|C| > 1$. Since then, theoretical research into these “new

Space group	Two vertical glide mirrors	Location	Momenta
#73	$\{M_x \frac{1}{2}, \frac{1}{2}, 0\}; \{M_y \frac{1}{2}, 0, 0\}$	W	Γ, T
#110	$\{M_x \frac{1}{2}, \frac{1}{2}, 0\}; \{M_y \frac{1}{2}, \frac{1}{2}, 0\}$	P	Γ, X
#142	$\{M_x \frac{1}{2}, \frac{1}{2}, 0\}; \{M_y \frac{1}{2}, 0, 0\}$	P	Γ, X
#206	$\{M_x \frac{1}{2}, \frac{1}{2}, 0\}; \{M_y \frac{1}{2}, 0, 0\}$	P	Γ, N
#228	$\{M_x \frac{1}{2}, \frac{3}{4}, 0\}; \{M_y \frac{3}{4}, \frac{1}{2}, 0\}$	W	Γ, X
#230	$\{M_x \frac{1}{2}, \frac{1}{2}, 0\}; \{M_y \frac{1}{2}, 0, 0\}$	P	Γ, N

Table I Phonon systems (or any spinless systems) where \mathbb{Z}_2 Dirac points associated with quad-helicoid surface states (QHSSs) can be obtained. Each column represents for the space group number, two vertical glide mirrors which protect the \mathbb{Z}_2 Dirac points together with \mathcal{T} , the momentum where \mathbb{Z}_2 Dirac points are located. Notably, all the listed space groups exhibit a wallpaper group of $p2gg$ on the (001) surface with two vertical glide mirror symmetries. Conversely, surfaces with a wall group of $p4gg$ is forbidden to have QHSSs.

quasiparticle excitations” has broadened to include bosonic systems, such as phonon spectra, with a focus on their topological invariants (Chern number, \mathbb{Z}_2 monopole charge, etc.), degeneracy and dispersion properties. This expansion has opened new avenues for exploring topological phenomena in bosonic systems within the material universe.

For example, the low-energy effective $k \cdot p$ model for a twofold Weyl phonon with Chern number of $C=N (> 0)$ can be written as:

$$H_N(\mathbf{k}) = \begin{pmatrix} Ak_z & B(k_x - ik_y)^N \\ B(k_x + ik_y)^N & -Ak_z \end{pmatrix}, \quad (34)$$

where A and B are real constants. The Chern number N is determined by the rotational symmetry of the system. For example, unconventional Weyl phonons with Chern numbers $C=\pm 2$ can be obtained in systems with $C_{3,4,6}$ rotational symmetries (Fang *et al.*, 2012; Tsirkin *et al.*, 2017), associated with helicoid/spiral surface states shown in Fig. 7 (a2).

Since phonons are spinless, such property can give rise to a new type of twofold Weyl phonon with the protection of both time-reversal symmetry and chiral cubic symmetry. The equivalence of $k_x/k_y/k_z$ under these symmetries leads to a low-energy effective $k \cdot p$ Hamiltonian for the twofold quadruple Weyl (TQW) phonon as (Li *et al.*, 2021a; Zhang *et al.*, 2020b):

$$H_{\text{TQW}}(\mathbf{k}) = - \begin{pmatrix} Ak_x k_y k_z & B(k_x^2 + \omega k_y^2 + \omega^2 k_z^2) \\ B(k_x^2 + \omega^2 k_y^2 + \omega k_z^2) & -Ak_x k_y k_z \end{pmatrix}, \quad (35)$$

where $\omega = e^{-\frac{2\pi i}{3}}$. In this case, an unconventional Weyl phonon with each band carrying the highest Chern number of $C = \pm 4$ can emerge in solids. Since the Weyl phonon described in Eq. (35) possesses a monopole charge of 4, it is referred to as a “twofold quadruple Weyl phonon” in Ref. (Li *et al.*, 2021a; Zhang *et al.*, 2020b). The existence of such twofold quadruple Weyl points was overlooked by topological band theory prior to 2020, as earlier studies did not account for the Bravais lattice degrees of freedom. The twofold quadruple Weyl phonon

requires the protection of chiral cubic symmetry and \mathcal{T} . As a result, it can only occur in specific scenarios, such as being located at the Γ for all chiral cubic space groups or at the $(\frac{\pi}{a}, \frac{\pi}{a}, \frac{\pi}{a})$ point for certain chiral cubic space groups, as detailed in Tab. I. Here, a represents the lattice constant of the cubic lattice.

Figures 7 (a1)-(a3) show three distinct twofold Weyl phonons with the Chern numbers of $C = +1, +2$, and $+4$ respectively. According to the “bulk-surface correspondence” (Hasan and Kane, 2010; Qi and Zhang, 2011), the number and the chirality of the topological surface states associated with Weyl phonons must match the value and sign of the Chern number. Additionally, threefold and fourfold unconventional Weyl phonons can also exist in solids, stabilized by different crystalline symmetries. These cases will be explored in detail in Sec. IV.A.

3. Unconventional Dirac Phonons

As discussed in the previous subsection, surface arcs arise when a pair of Weyl phonons with opposite Chern numbers project to distinct momenta in the surface Brillouin zone (BZ), as illustrated in Figs. 7 (a1)-(a3). Conversely, if two Weyl points with opposite chirality project to the same momentum, the surface arcs vanish, as shown in Fig. 7 (a4). When such a pair of Weyl phonons carrying opposite Chern numbers approaches each other under \mathcal{PT} symmetry, they coalesce into a Dirac node accompanied by two counter-propagating helicoidal surface states. Crucially, this \mathcal{PT} -protected Dirac phonon carries a net monopole charge of zero, rendering it topologically trivial and devoid of protected surface states in Dirac semimetals (Kargarian *et al.*, 2016; Le *et al.*, 2018). Introducing a symmetry-preserving perturbation hybridizes the anti-parallel surface states, lifting their degeneracy and generating gapped, topologically trivial surface states (Kargarian *et al.*, 2016; Le *et al.*, 2018). Despite this straightforward theoretical picture, two critical challenges remain unresolved before the year of 2018:

(p1) In electronic systems, double Fermi arcs have predominantly been proposed in Dirac semimetals like Na_3Bi (Liu *et al.*, 2014b; Wang *et al.*, 2012; Xiong *et al.*, 2015) and Cd_3As_2 , (Borisenko *et al.*, 2014; He *et al.*, 2014; Li *et al.*, 2016; Liu *et al.*, 2014a; Neupane *et al.*, 2014; Wang *et al.*, 2013; Yi *et al.*, 2014), they serve as critical experimental signatures of their topological nature. These arcs arise from the hybridization of two anti-parallel surface states, which remains incomplete due to their weak hybridization. A key unresolved question is identifying the conditions that lead to fully gapped surface states (and the absence of Fermi arcs). In other words, what is the microscopic mechanism for obtaining a strong hybridization of two anti-parallel surface states in Dirac phonon systems?

(p2) While the Dirac phonon is not topological in general and associated with gapped surface states, is it possible to obtain topologically protected Dirac phonons associated with

topological surface states?

To address (p1), (Le *et al.*, 2018) pointed out that the deformation of the anti-parallel surface states (termed double Fermi arcs in their study) arises due to a significant k^3 term that respects all crystal symmetries. They illustrated this with first-principle calculations on $\beta\text{-CuI}$, for which the effective Hamiltonian at the Dirac point can be formulated as $H_{\text{eff}}(\mathbf{k})$:

$$\begin{aligned} H_{\text{eff}}(\mathbf{k}) &= H_0 + H_1 + H_2, \\ H_0 &= \epsilon(\mathbf{k}) + M(\mathbf{k})\sigma_0\tau_3 - A(\mathbf{k}_{\parallel})(k_x\sigma_3\tau_2 + k_y\sigma_0\tau_1), \\ H_1 &= (D_2 + D_3k_z^2)(-k_x\sigma_1\tau_2 + k_y\sigma_2\tau_2), \\ H_2 &= -D_1k_z[(k_x^2 - k_y^2)\sigma_1\tau_2 + 2k_xk_y\sigma_2\tau_2]. \end{aligned} \quad (36)$$

Hence, the parameter D_1 plays a crucial role in the formation of double Fermi arcs in Dirac semimetals, and it corresponds to a three-step hybridization process. First, two I atoms exhibit strong coupling due to substantial atomic spin-orbit coupling (SOC), denoted by λ_1 . Subsequently, a robustly hybridized σ bond between I and Cu atoms, denoted by t_1 . Lastly, the proximity of two Cu atoms contributes to a significant coupling, t_2 . Usually, the cubic term is negligible in Dirac semimetals; however, in $\beta\text{-CuI}$, its relevance stems from the unique crystal structure, where all three parameters are substantial. Consequently, $\beta\text{-CuI}$ exhibits a large D_1 parameter, leading to considerable hybridization of the anti-parallel surface states.

Despite the SOC parameter λ_1 being even more pronounced in Dirac semimetals such as Na_3Bi and Cd_3As_2 compared to $\beta\text{-CuI}$, the second and third parameters, t_1 and t_2 , are significantly smaller because of the weak bonding between cations and anions. This suggests a correspondingly small value for the parameter D_1 in these materials.

In Dirac phonon systems, the SOC parameter λ_1 is zero due to the spin-zero nature of phonons. However, a large parameter D_1 can be achieved in systems that exhibit strong chemical bond hybridization or proximity effects.

To address (p2), a new type of topological invariant termed \mathbb{Z}_2 -type monopole charge Q must be introduced for topological Dirac phonons, since the \mathbb{Z} -type monopole charge C is zero. (Fang *et al.*, 2016; Yukitake *et al.*, 2025b; Zhang *et al.*, 2022b; Zhang and Murakami, 2023) have highlighted that in systems exhibiting \mathcal{TG} symmetry, where \mathcal{G} signifies the glide mirror symmetry, this \mathbb{Z}_2 monopole charge Q can be defined (Cai *et al.*, 2020; Cheng *et al.*, 2020b; Fang *et al.*, 2016; Kim *et al.*, 2021; Lu *et al.*, 2016a; Qian *et al.*, 2023; Su *et al.*, 2022; Yukitake *et al.*, 2025a,b; Zhang *et al.*, 2022b; Zhang and Murakami, 2023). When $Q \neq 0$, double helicoid surface states emerge, as shown in Fig. 10 (a3). Conversely, if $Q = 0$, the Dirac phonon is trivial with gapped surface states. Details are as follows.

(Yukitake *et al.*, 2025b) considered a system that possess a single glide symmetry operation, denoted as $\mathcal{G}_y = \{M_y|00\frac{1}{2}\}$, as shown in Fig. 10 (a). When the time-reversal symmetry, \mathcal{T} , is a symmetry of the system, the operation $\tilde{\Theta}_y = \mathcal{T}\mathcal{G}_y$

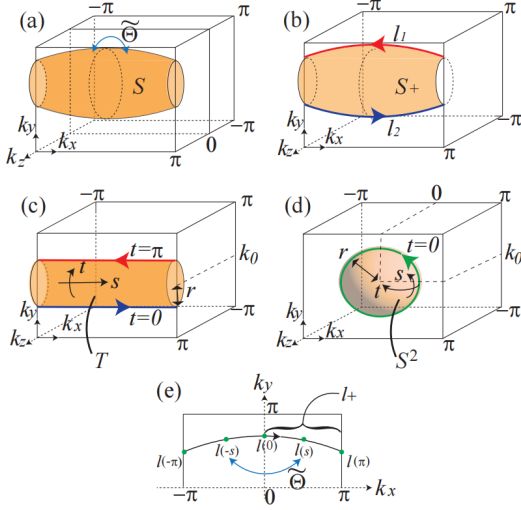


Figure 9 The \mathbb{Z}_2 monopole charge Q is defined using specific surfaces and lines. In (a), Q is defined on a surface S that does not intersect with the plane $k_z = 0$. This surface S is closed under $\hat{\Theta}$, with the half part S_+ ($k_z \geq \pi$) shown in (b). The boundary of S_+ , denoted as $\partial S_+ = l_1 \cup l_2$, consists of two lines. Examples of such surfaces S are provided in (c) and (d), where S is defined by a torus T and a sphere S^2 , respectively. (e) illustrates a closed line l used to define the quantity $P[l]$. Adapted from Ref. (Yukitake *et al.*, 2025b).

is also conserved. It is found that $\tilde{\Theta}_y^2 = e^{-ik_z}$, indicating that the $k_z = \pi$ ($-\pi$) plane is distinctive, as it satisfies the condition $\tilde{\Theta}_y^2 = -1$. In this context, (Yukitake *et al.*, 2025b) examined the \mathbb{Z}_2 -type Dirac points on the $k_z = \pi$ plane in the 3D BZ. These two Dirac points are connected by \mathcal{T} symmetry, precluding their occurrence at time-reversal-invariant momenta (TRIM). Consequently, \mathbb{Z}_2 Dirac points typically emerge along high-symmetry lines in systems possessing a single glide mirror symmetry, and at non-TRIM high-symmetry points in systems with two vertical glide mirror symmetries (Fang *et al.*, 2016; Kim *et al.*, 2021; Yukitake *et al.*, 2025a,b; Zhang *et al.*, 2022b; Zhang and Murakami, 2023). Subsequently, we will review the convention-independent \mathbb{Z}_2 monopole charge $Q[S]$ associated with an oriented closed surface S , which adheres to the following criteria as established by (Yukitake *et al.*, 2025b): (i) The surface S is closed under the operation $\hat{\Theta} : (k_x, k_y, k_z) \mapsto (-k_x, k_y, -k_z)$, (ii) The surface S does not intersect with the plane defined by $k_z = 0$ (iii) The system exhibits a bulk energy gap over the entire surface S .

Analogous to \mathbb{Z} -type monopole charge C , the \mathbb{Z}_2 -type monopole charge Q is defined in terms of wavefunctions over a sphere S that encloses the Dirac point, as described in (Fang *et al.*, 2016). Thus, Q can be expressed as:

$$Q = \frac{1}{2\pi} \int_{S_+} d\mathbf{S} \cdot \nabla_{\mathbf{k}} \times \mathbf{A}(\mathbf{k}) - 2 \sum_{l \in \partial S_+} P[l] \pmod{2}, \quad (37)$$

where S_+ is the divided part with $k_z \geq \pi$ shown in Fig. 9 (b)

and ∂S_+ is the boundary of S_+ on the plane $k_z = \pi$. $P[l]$ is defined as $P[l] = \frac{1}{2\pi} \gamma^\alpha[l] \pmod{1}$, where $\gamma^\alpha[l]$ represents the Berry phase when the occupied bands are divided into two groups α and β , such that $\hat{\Theta}$ transforms the two groups mutually. Since the Berry curvature is gauge-independent and $P[l]$ is gauge-independent up to an integer, the definition of Q in Eq. (37) maintains gauge invariance. Moreover, when a smooth gauge choice is adopted over the surface S , it can be shown that Q assumes integer values, as expressed by:

$$(-1)^Q = \prod_{l \in \partial S_n} \frac{\text{Pf } \omega[l(0)]}{\sqrt{\det \omega[l(0)]}} \frac{\text{Pf } \omega[l(\pi)]}{\sqrt{\det \omega[l(\pi)]}}. \quad (38)$$

When the integration surface is chosen to be a torus T , as depicted in Fig. 9 (c), the \mathbb{Z}_2 monopole charge $Q[T]$ can be expressed as follows:

$$Q[T] = P_{\hat{\Theta}}(t = \pi) - P_{\hat{\Theta}}(t = 0) \pmod{2}. \quad (39)$$

At $t = \pi$ and $t = 0$, we encounter two distinct lines on the $k_z = \pi$ plane, which are positioned on either side of the Dirac point. The operator $P_{\hat{\Theta}}$ is defined as:

$$P_{\hat{\Theta}}(l_i) = \frac{1}{2\pi} (\gamma^\alpha[l_i] - \gamma^\beta[l_i]) \quad (40)$$

Thus, $Q[T]$ is the difference of $\hat{\Theta}$ -polarization, and it serves to establish the bulk-surface correspondence of \mathbb{Z}_2 Dirac points by considering the surface T as a 2D BZ $[-\pi, \pi] \times [-\pi, \pi]$ in the (s, t) parameter space, as shown in Fig. 10 (a1). Given that $\hat{\Theta}^2 = -1$ along the lines where $t = 0$ and $t = \pi$, the anti-unitary operator $\hat{\Theta}$ behaves analogously to time-reversal symmetry in \mathcal{T} -symmetric \mathbb{Z}_2 topological insulators (Fu and Kane, 2007). This implies that the energy bands, both from the bulk and the surface, will exhibit Kramers's degeneracy at the points at $t = 0$ and $t = \pi$. Upon projection onto the (100) surface BZ, the torus T is projected onto a circle path c , as marked by the orange circle in Fig. 10 (a1). If the \mathbb{Z}_2 charge $Q[T]$ is nontrivial, an odd number of \mathbb{Z}_2 Dirac points are enclosed within the torus. Consequently, a pair of helical surface states will emerge on the circle C , as shown by the red and blue bands in Fig. 10 (a2). These two surface states are degenerate at $t = 0$, resulting in a degenerate line along the boundary of the surface BZ. Adjusting the radius of circle C allows for the emergence of two helical surface states, as shown in Fig. 10 (a3). The intersection of these two surface states is protected by the symmetry \mathcal{GT} , leading to the formation of double helical (anti-parallel) surface states. Figure 10 (a4) illustrates the Fermi surface of a system hosting two \mathbb{Z}_2 Dirac points, featuring two Fermi arcs that link the projection of the Dirac points.

\mathbb{Z}_2 -type Dirac points may reside at various momenta, subject only to the constraint of satisfying the $\tilde{\Theta}_y$ symmetry, which is associated with a high-symmetry line in the BZ. When two Dirac points are projected onto distinct momenta

within the surface BZ, a pair of anti-parallel helical surface states emerges. These states are topologically protected by the charge Q , as shown in Fig. 10 (b2). When two $\hat{\Theta}_{i,j}$ symmetries are present, with $i, j \in \{x, y, z\}$, Dirac points are confined to the high-symmetry points within the BZ, as listed in Tab. 10. In this case, if two Dirac points are projected onto the identical momentum within the surface BZ, the quadruple surface states appear, as shown in Fig. 10 (b3).

In certain instances, a \mathbb{Z}_2 Dirac point may split into a pair of Weyl dipoles or transform into a \mathbb{Z}_2 nodal ring, a transformation that depends on the crystalline symmetries inherent to the system. All of the topological band crossings mentioned here can be cataloged by the \mathbb{Z}_2 -type monopole charge Q , associated with topologically protected surface states (Cai *et al.*, 2020; Cheng *et al.*, 2020b; Fang *et al.*, 2016; Kim *et al.*, 2021; Lu *et al.*, 2016a; Qian *et al.*, 2023; Su *et al.*, 2022; Yukitake *et al.*, 2025a,b; Zhang *et al.*, 2022b; Zhang and Murakami, 2023).

4. Node-line Phonons

Phonon topological gapless states mentioned previously feature band crossings at discrete zero-dimensional points in momentum space. In certain instances, these band crossings may transform into one-dimensional curves within the three-dimensional Brillouin zone, referred to as nodal lines or nodal rings (Burkov *et al.*, 2011; Fang *et al.*, 2016; Zhang *et al.*, 2019b). Nodal lines or rings typically require the protection of additional symmetries, such as mirror symmetry, product of spatial inversion and time-reversal symmetry (\mathcal{PT}), and the like. Perturbations that conserve these symmetries cannot eliminate the crossing line and thereby cannot open a complete energy gap. Consider a two-band phonon system that preserves mirror symmetry M_z ; the low-energy effective Hamiltonian for this system can be expressed as:

$$H_{\text{NL}}(\mathbf{k}) = (m - k_x^2 - k_y^2)\sigma_z + k_z\sigma_x, \quad (41)$$

with the eigenvalues of $E(\mathbf{k}) = \pm \sqrt{(m - k_x^2 - k_y^2)^2 + k_z^2}$. Hence, Eq. (41) captures the characteristics of nodal line/ring phonon constrained on the $k_z = 0$ plane (a mirror-invariant plane), and the configuration of the nodal line/ring being influenced by the system's parameters, as shown by the nodal ring in Fig. 11. As m approaches zero, the nodal ring will shrink to a gapless point, evolving into a quadratic Weyl phonon.

The topological invariant characterizing node-line/ring phonons is the Berry phase, denoted as γ , which is defined by an integral on a closed loop as shown in Fig. 11 (b).

$$\gamma = i \oint_C \langle u(\mathbf{k}) | \nabla_{\mathbf{k}} | u(\mathbf{k}) \rangle \cdot d\mathbf{k} \mod 2\pi, \quad (42)$$

wherein the phonon bands are entirely separated by a gap along the k -loop. If the loop encircles the nodal line/ring,

then $\gamma = \pi$; conversely, if the loop does not encircle the nodal line/ring, $\gamma = 0$.

In addition to the mirror-protected node-line/ring phonons, which are fixed to the mirror-invariant plane, the combined spatial inversion and time-reversal symmetry (\mathcal{PT}) can also safeguard nodal lines/rings. These nodal lines/rings may exist in various configurations and at any momentum within the Brillouin zone (Zhang *et al.*, 2019b). Independent of the specific symmetries of the system, node-line/ring phonons with $\gamma = \pi$ host topological surface states. These correspond to the drumhead surface states that link the nodal line/ring band crossings on the surface BZ, as depicted by the blue curve in Fig. 11 (c).

C. Diagnosing Topological Phonons at Generic Momenta

The framework of topological band theory is grounded in the topology of the ground state wave function, which is characterized by a topological number referred to as a topological invariant. This invariant serves to identify and differentiate topological states, thereby providing a diagnostic tool for their classification. Consequently, it is crucial to establish both the topological classifications of systems with varying symmetries and the interconnection between topological states and their corresponding topological surface states. This relationship is fundamentally important and is recognized as the “bulk-edge correspondence”.

In 2007, (Fu and Kane, 2007) proposed that the calculation for topological invariant of \mathbb{Z}_2 topological insulators can be simplified in systems with both inversion (\mathcal{P}) and time-reversal (\mathcal{T}) symmetries. This method involves examining the parity of the electron occupation at time-reversal invariant momenta (TRIM). A significant contribution of this work was the illustration of how the utilization of symmetries can simplify the computation of topological invariant, thereby enhancing the understanding and analysis within the field. In conjunction with the “ten-fold way” theory discussed in Sec. II.A, which suggests that crystalline symmetries can give rise to novel topological phases, it becomes evident that symmetries play a pivotal role in simplifying the classification and diagnosis of topological states. This insight laid the groundwork for subsequent developments in symmetry-based indicators (Po *et al.*, 2017) and the independent advancement of topological quantum chemistry (Bradlyn *et al.*, 2017).

The symmetry-based indicator theory constitutes a conceptual framework that utilizes symmetries to simplify the calculation and classification of topological states across various symmetry classes, particularly within the context of the 230 space groups, and accounting for the presence or absence of time-reversal (\mathcal{T}) and SU(2) symmetries. The key idea of this theory is the construction of a gapped band structure space, denoted as $\{\text{BS}\}$, for a given specified band system within the realm of 230 space groups. This space $\{\text{BS}\}$ is constructed from the symmetry attributes of the occupied bands at each

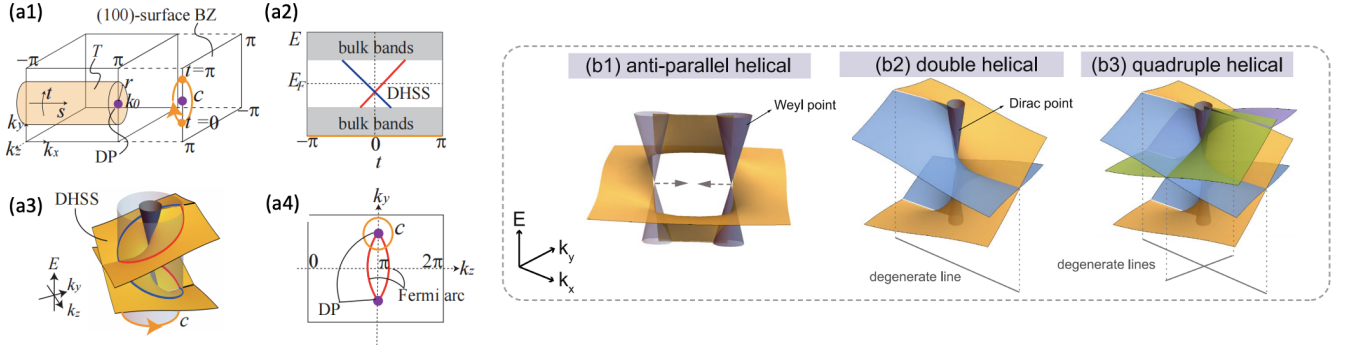


Figure 10 “Bulk-surface correspondence” for the \mathbb{Z}_2 monopole charge $Q[T]$, defined on the torus T . (a1) Bulk and (100) surface Brillouin Zones. A \mathbb{Z}_2 Dirac point is situated within the $k_z = \pi$ plane of the torus T and is projected onto the circle C . The $k_z = \pi$ plane is characterized by $\mathcal{TG}^2 = -1$. The torus may be conceptualized as a 2D Brillouin Zone in the parameter space of (s, t) , where Kramers’ degeneracy appears at $t = \pi, 0$. (a2) When a \mathbb{Z}_2 Dirac point is enclosed within T , the surface states along the loop C exhibit helical characteristics and are degenerate at $t = 0$ ($t = \pi$). (a3) By altering the radius of the loop C , double-helical surface states are obtained, associated with two Fermi arcs shown in (a4). The charge $Q[T]$ is applicable to systems with \mathbb{Z}_2 -charged nodal ring or a Weyl dipole, which can interconvert with Dirac points. (b1) Represents the topological surface state connecting a pair of Weyl phonons with opposite chirality. (b2) and (b3) are the double and quadruple helical surface states, respectively, which are attributed to the \mathbb{Z}_2 Dirac phonons. (a) is adapted from Ref. (Yukitake *et al.*, 2025b) and (b) is adapted from Ref. (Zhang and Murakami, 2023).

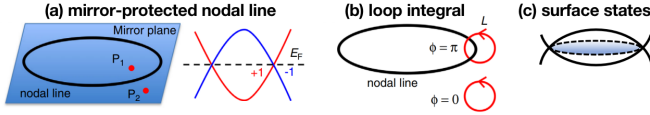


Figure 11 Illustration of node-line phonons. (a) The mirror-protected nodal ring phonon is constrained to the mirror plane and consists of two bands with distinct mirror eigenvalues. (b) The Berry phase is π when the integration loop encircles the nodal ring, and it is zero when the integration loop is positioned away from the nodal ring. (c) The drumhead surface state associated with the nodal ring.

high-symmetry momenta in the Brillouin zone:

$$\text{BS} = \sum_{i=1}^{d_{\text{BS}}} m_i \mathbf{b}_i. \quad (43)$$

Here, d_{BS} represents a positive integer, \mathbf{b}_i serves as the generator of the band insulators, m_i is an integer and is uniquely determined once the basis is chosen. At the same time, an atomic insulator space, denoted as $\{\text{AI}\}$, is also constructed under the 230 space groups. These $\{\text{AI}\}$ are exemplars of band insulators that arise from an initial symmetrical configuration of atomic sites in real space, with the subsequent full occupation of a defined set of orbitals at each atomic position. Consequently, the aggregation of arbitrary sets of atomic insulators will invariably yield another atomic insulator space, as expressed by:

$$\{\text{AI}\} \simeq \mathbb{Z}^{d_{\text{AI}}} = \left\{ \sum_{i=1}^{d_{\text{AI}}} m_i \mathbf{a}_i : m_i \in \mathbb{Z} \right\}, \quad (44)$$

where \mathbf{a}_i is the generator of the atomic insulators. Hereafter, the quotient group for $\{\text{BS}\}$ and $\{\text{AI}\}$ can be straightforward to evaluate:

Table 4 Symmetry-based indicators of band topology for systems with time-reversal symmetry and negligible spin-orbit coupling

X_{BS}	Space groups
\mathbb{Z}_2	3, 11, 14, 27, 37, 48, 49, 50, 52, 53, 54, 56, 58, 60, 66, 68, 70, 75, 77, 82, 85, 86, 88, 103, 124, 128, 130, 162, 163, 164, 165, 166, 167, 168, 171, 172, 176, 184, 192, 201, 203
$\mathbb{Z}_2 \times \mathbb{Z}_2$	12, 13, 15, 81, 84, 87
$\mathbb{Z}_2 \times \mathbb{Z}_4$	147, 148
$\mathbb{Z}_2 \times \mathbb{Z}_2 \times \mathbb{Z}_2$	10, 83, 175
$\mathbb{Z}_2 \times \mathbb{Z}_2 \times \mathbb{Z}_2 \times \mathbb{Z}_4$	2

X_{BS} the quotient group between the group of band structures and that of atomic insulators

Figure 12 The nontrivial symmetry-based indicator groups, denoted as X_{BS} , apply to phonon systems that preserve time-reversal symmetry. X_{BS} represents the quotient group formed by the set of “gapped” band structures and the set of “atomic insulators,” a concept originally derived from electronic systems. This notion can be extended to encompass all physical systems described by band theory. Adapted from Ref. (Po *et al.*, 2017).

$$X_{\text{BS}} = \frac{\{\text{BS}\}}{\{\text{AI}\}}. \quad (45)$$

An element within X_{BS} denotes a comprehensive collection of band structures that are differentiated solely by the addition of an atomic insulator in each instance. By harnessing the various symmetries of a system, this theoretical framework provides a methodical strategy for identifying and categorizing topological states. It offers profound understanding into the underlying physics and facilitates the investigation of topological phases and their associated phenomena.

Figure 12 displays the nontrivial symmetry-based indicator groups X_{BS} for the 230 space groups in the context of phonon

spectra. The notation $\mathbb{Z}_n \times \mathbb{Z}_m$ signifies Abelian groups that are isomorphic to the respective quotient groups (Po *et al.*, 2017). (Song *et al.*, 2018; Zhang *et al.*, 2020a; Zhang and Murakami, 2021) linked the the symmetry-based indicator groups to the specific topological invariants based on rigorous derivations, providing both the general proof and the analytical expression to quantify these indicators. Specifically, a nontrivial symmetry-based indicator group (e.g., with nonzero values) may correspond to multiple distinct topological invariants, such as the Berry phase and the \mathbb{Z}_2 -monopole charge, reflecting a one-to-many mapping inherent to indicator theories. In the subsequent sections, we will use space group #2, #3 and #82 as case studies to illustrate the implications of the symmetry-based indicators in diagnosing topological phonon.

1. Symmetry-based Indicators for Nodal-line Phonons

The symmetry-based indicator group for phonon systems with space group #2 is $\mathbb{Z}_2 \times \mathbb{Z}_2 \times \mathbb{Z}_2 \times \mathbb{Z}_4$. This group indicates a topological semimetal that exhibits nodal-line or nodal-ring band crossings in the Brillouin zone when not all of the four \mathbb{Z}_n components are trivial (to be zero). The explicit formula for the symmetry-based indicator group of space group #2 is provided below:

$$z_{2,1} \equiv \sum_{\mathbf{K} \in \text{TRIM at } \{k_1=\pi\}} \frac{N_-(\mathbf{K}) - N_+(\mathbf{K})}{2} \mod 2, \quad (46)$$

$$z_{2,2} \equiv \sum_{\mathbf{K} \in \text{TRIM at } \{k_2=\pi\}} \frac{N_-(\mathbf{K}) - N_+(\mathbf{K})}{2} \mod 2, \quad (47)$$

$$z_{2,3} \equiv \sum_{\mathbf{K} \in \text{TRIM at } \{k_3=\pi\}} \frac{N_-(\mathbf{K}) - N_+(\mathbf{K})}{2} \mod 2, \quad (48)$$

$$z_4 \equiv \sum_{\mathbf{K} \in \text{TRIM}} \frac{N_-(\mathbf{K}) - N_+(\mathbf{K})}{2} \mod 4, \quad (49)$$

where $N_{\pm}(\mathbf{K})$ represents the count of bands that exhibit even/odd parity under inversion symmetry at the four time-reversal-invariant momenta (TRIM) located on the $k_i \in \{1,2,3\} = \pi$ plane. The quantities $z_{2,1}z_{2,2}z_{2,3}z_4$ serve as the indicators for the symmetry-based indicator group $\mathbb{Z}_2 \times \mathbb{Z}_2 \times \mathbb{Z}_2 \times \mathbb{Z}_4$. The first three \mathbb{Z}_2 indicate the orientation and the location of the node-line/ring band crossings. Specifically, nodal lines are oriented along the reciprocal lattice direction k_i when $z_{2,i} = 1$, or they are situated around $k_i = \pi$. The final z_4 index indicates the count of nodal line/ring band crossings. An even number of nodal lines or rings within the Brillouin zone is signified by $z_4 = 0, 2$, while an odd number is indicated by $z_4 = 1, 3$. Combined the information from these four symmetry-based indicators, one can ascertain the entire

configuration of nodal lines/rings throughout the BZ (Zhang *et al.*, 2020a; Zhang and Murakami, 2021; Zhang *et al.*, 2022c, 2019b,b).

For instance, when the values for the symmetry-based indicator group $\mathbb{Z}_2 \times \mathbb{Z}_2 \times \mathbb{Z}_2 \times \mathbb{Z}_4$ are $z_{2,1}z_{2,2}z_{2,3}z_4 = (0001)$, this indicates that an odd number of nodal lines/rings will be present around the Γ point, corresponding to the most basic configuration featuring a single nodal ring encircling Γ , as depicted in Fig. 13. For the symmetry-based indicator values of $\mathbb{Z}_2 \times \mathbb{Z}_2 \times \mathbb{Z}_2 \times \mathbb{Z}_4$ given by $z_{2,1}z_{2,2}z_{2,3}z_4 = (1002)$, an even number of nodal lines/rings will be aligned along the reciprocal lattice vector k_1 , which is represented by the two nodal lines. For the symmetry-based indicator values of $\mathbb{Z}_2 \times \mathbb{Z}_2 \times \mathbb{Z}_2 \times \mathbb{Z}_4$ specified as $z_{2,1}z_{2,2}z_{2,3}z_4 = (0002)$, an even number of nodal lines/rings will be found in the vicinity of the Γ point, exemplified by the two nodal rings. It is important to note that nodal lines/rings characterized by $z_{2,1}z_{2,2}z_{2,3}z_4 = (0002)$ possess a nonzero \mathbb{Z}_2 monopole charge, and such features can only emerge or disappear in conjunction, that is, in pairs.

2. Symmetry-based Indicators for Weyl Phonons

In non-centrosymmetric systems, the emergence of Weyl phonons also can be diagnosed by symmetry-based indicators. For example, space group #3 only includes a C_2 symmetry. The indicator \mathbb{Z}_2 for this space group is linked to the product of the C_2 eigenvalues at all TRIMs, which serves to diagnose the occurrence of Weyl phonons within a specific plane. \mathbb{Z}_2 is described by the topological invariant α_2 , as presented below:

$$\alpha_2 \equiv \sum_{K_i=0, \mathbf{K} \in \text{TRIM}} N_{\zeta=-1}(\mathbf{K}) \mod 2, \quad (50)$$

where i denotes the rotational axis for the C_2 operation, and ζ represents the eigenvalue corresponding to the C_2 operator. If $\alpha_2 = 1$, the Berry phase accumulated along a loop that encircles half of the Brillouin zone on the $k_i = 0$ plane is π . This condition gives rise to 1 modulo 2 Weyl phonons on the half of the $k_i = 0$ plane and 2 modulo 4 Weyl phonons across the entire $k_i = 0$ plane, as depicted in Fig. 14 (a). Because two Weyl phonons on the $k_i = 0$ plane share the same chirality, the conservation of monopole charge necessitates the existence of two additional Weyl phonons with opposite chirality on the $k_i = \pi$ plane.

For space group #82, which exhibits S_4 symmetry, symmetry-based indicator \mathbb{Z}_2 can be established as follows:

$$\omega_2^0 = N_{\xi=-1}(\Gamma) + N_{\xi=-1}(M) + N_{\xi=-1}(X) \mod 2, \quad (51)$$

$$\omega_2^\pi = N_{\xi=-1}(Z) + N_{\xi=-1}(A) + N_{\xi=-1}(R) \mod 2. \quad (52)$$

ξ is the eigenvalue of the C_4 operator, the quantities ω_2^0 and ω_2^π represent the counts of Weyl phonons located at the $k_i = 0$ and $k_i = \pi$ planes, respectively. Since space group #82

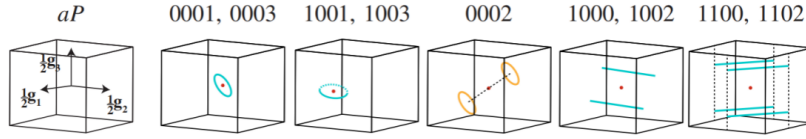


Figure 13 In space group #2, which only preserves the inversion symmetry, the configuration of topological phonon bands is associated with the symmetry-based indicators. Yellow nodal rings with $z_{2,1}z_{2,2}z_{2,3}z_4 = (0002)$ carry a nonzero \mathbb{Z}_2 monopole charge. Adapted from Ref. (Song *et al.*, 2018).

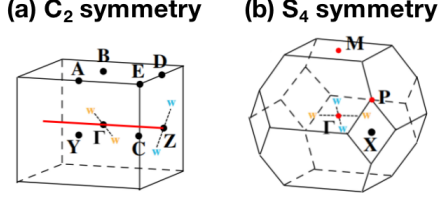


Figure 14 The symmetry-based indicator theory is employed to identify Weyl phonons in space groups #3 with C_2 symmetry and #82 with S_4 symmetry. The blue and yellow markers denote the positions of Weyl phonons with distinct chirality. This theoretical framework enables the diagnosis of Weyl phonons at the $k = 0$ and $k = \pi$ planes in C_2 -symmetric systems, and at the $k = 0$ plane in S_4 -symmetric systems. Adapted from Ref. (Song *et al.*, 2018).

constitutes a body-centered lattice, ω_2^π is null. Consequently, if ω_2^0 equals 1, it signifies the presence of 4 modulo 8 Weyl phonons on the $k_i = 0$ plane. This is illustrated in Fig. 14 (b), where the blue and yellow letters “w” denote the locations of Weyl phonons with distinct chirality (Song *et al.*, 2018; Zhang *et al.*, 2020a; Zhang and Murakami, 2021).

D. Comparison Between Different Topological Quasi-particles

Topological phonons, grounded in the principles of band theory, exhibit parallels with other topological quasiparticles, particularly those within spinless electronic band structures. They share characteristics such as various types of Weyl points, Dirac points, and nodal lines/rings, along with the emergence of topological surface states due to the “bulk-surface correspondence”. Nonetheless, the fundamental distinctions between phonons and electrons could pave the way for the revelation of novel topological phenomena unique to phonons. Moreover, topological phonons are endowed with distinctive attributes that set them apart from their counterparts among other topological quasiparticles.

For instance, in electronic systems, node-line or node-ring states can be destroyed by the spin-orbit coupling effect, which introduces a finite energy gap. In contrast, these states emerge in phonon spectra due to their inherent “zero spin” and “orbital-free” characteristics (Zhang *et al.*, 2019b). In three-dimensional systems, acoustic phonons inherently exhibit threefold degeneracy as Goldstone modes, and they

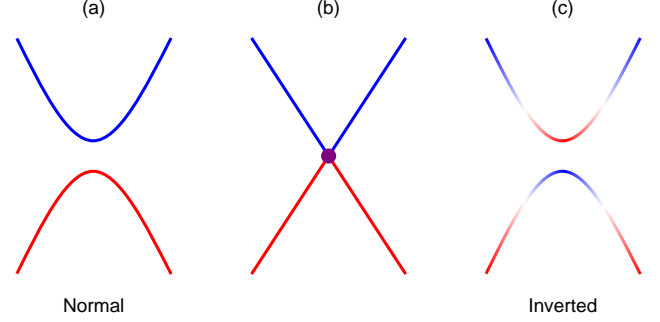


Figure 15 Illustration of the topological band structure featuring different band order, with panels (a) through (c) depicting the conventional, semimetallic, and inverted band configurations, respectively. The inverted band order signifies a nontrivial topological index for the bulk Bloch wave functions.

transform into spin-1 Weyl phonons in chiral systems (Zhang *et al.*, 2018a). Phonons can also possess additional quantum degrees of freedom, such as pseudospin and angular momentum, which endow them with novel physical properties associated with their topological states (Zhang *et al.*, 2023b). The topological nature of phonons is inherently linked to the vibrational modes of the crystal lattice, leading to unique physical phenomena and practical applications (Prodan and Prodan, 2009b). The collective nature of lattice vibrations fosters interactions between phonons and other quasiparticles within the lattice, such as electrons or magnons, resulting in hybridized states and emergent phenomena that differentiate them from those observed solely in electronic or magnetic systems. In addition, topological phonons can be observed through various experimental techniques, including Raman scattering (Zhang *et al.*, 2023b), thermal transport (Mangeolle *et al.*, 2022), inelastic x-ray scattering (Li *et al.*, 2021a; Miao *et al.*, 2018; Zhang *et al.*, 2019b), neutron scattering (Jin *et al.*, 2022), and high-energy electron loss spectroscopy (Li *et al.*, 2023a), offering concrete evidence of their topological characteristics.

III. EXAMPLES OF TOPOLOGICAL PHONONS: 1D AND 2D LATTICE MODELS

The band topology is closely related to the concept of geometric phase, first introduced by M. Berry in the con-

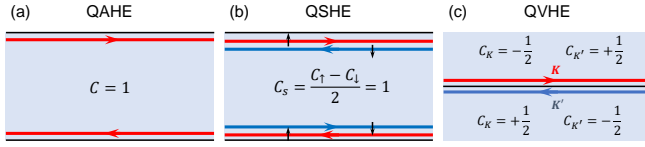


Figure 16 Schematics of various topological states of phonon in 2D lattices. (a)-(c) depict the phononic quantum anomalous Hall effect (QAHE), quantum spin Hall effect (QSHE) and quantum valley Hall effect (QVHE) characterized by nonzero Chern number, spin Chern number, and valley Chern number, respectively.

text of quantum adiabatic evolution within arbitrary parameter space (Berry, 1984). In solid-state systems, the Bloch wave vector \mathbf{k} offers a natural quantum adiabatic parameter space, and the geometric phase based on \mathbf{k} was first introduced by J. Zak (Zak, 1989). Two different kinds of geometric phases can be defined according to different physical dimensions: (i) One is the line integral of Berry connection $\theta_C = \oint_C d\mathbf{k} \cdot \mathbf{A}(\mathbf{k})$, for any closed 1D loop C within the Brillouin zone; (ii) The other is the surface integral of the Berry curvature $\theta_S = \iint_S d\mathbf{S} \cdot \boldsymbol{\Omega}(\mathbf{k})$ for any 2D surface S . $\mathbf{A}(\mathbf{k}) = i\langle u_{\mathbf{k}} | \nabla_{\mathbf{k}} u_{\mathbf{k}} \rangle$ and $\boldsymbol{\Omega}(\mathbf{k}) = \nabla_{\mathbf{k}} \times \mathbf{A}$ are the Berry connection and curvature, respectively (with $|u_{\mathbf{k}}\rangle$ being the cell-periodic part of Bloch wave function). The former can be defined in 1D-3D but the latter exist only in 2D and 3D because the cross derivative is ill-defined in 1D.

In 1D systems, the integration of the Berry connection over the entire Brillouin zone yields a topological invariant known as the Zak phase (Xiao *et al.*, 2010; Zak, 1989):

$$\theta_Z = i \int_{-\pi/a}^{\pi/a} dk \left\langle u_k \left| \frac{\partial u_k}{\partial k} \right. \right\rangle, \quad (53)$$

where a is the lattice constant. The Zak phase, denoted as θ_Z , is intricately linked to the electronic polarization, forming the cornerstone of the modern theory of electric charge polarization (King-Smith and Vanderbilt, 1993). Due to its oddness under inversion symmetry \mathcal{P} , the Zak phase assumes only two possible values, 0 or π , within systems possessing \mathcal{P} symmetry. A θ_Z value of π (or $\theta_Z = 0$) signifies an inverted (or normal) band order, respectively (Fig. 15).

In 2D systems, the integration of Berry curvature over the 2D BZ defines the topological Chern number (Hasan and Kane, 2010; Qi and Zhang, 2011; Thouless *et al.*, 1982a)

$$C = \frac{1}{2\pi} \iint d^2\mathbf{k} \Omega_z(\mathbf{k}) \quad (54)$$

which describes the quantum Hall (QH) family of topological phases of matter as shown in Fig. 16. The phononic quantum (anomalous/valley/spin) Hall like states are representative gapped states of topological phonons in 2D lattices as shown in Fig. 16. The quantum (anomalous) Hall effect (QAHE) support one-way chiral edge states, distinguished by a nonzero phonon Chern number C within the bulk 2D phonon band structure. The chiral edge states are immune to

back scattering thus providing robust phonon transport channels. The quantum spin Hall effect (QSHE) can be viewed as a pair of quantum (anomalous) Hall states with helical (pseudo-)spin-polarized edge states. As the phonon is a spin-zero quasi-particle, a pseudospin degree of freedoms refers to any kind of double band degeneracy which can be effectively characterized by 2×2 Pauli matrices. By integrating the Berry curvature over a subset of the BZ, valley Chern numbers can be defined, which may take on non-integer values. Consequently, the valley Chern number alone does not ensure the presence of topological edge states at bare open edges. However, for an interface across which the change of the valley Chern number is a nonzero integer, the valley-polarized interface states will appear, which is called quantum valley Hall effect (QVHE).

In this section, we will introduce specific models that are used to realize topological phononic states in 1D and 2D systems. Possible materials realizations are discussed in the end.

A. Topological Phonons in 1D: Su-Schrieffer-Heeger Model

The phononic Su-Schrieffer-Heeger (SSH) model is a prototypical example of a topological band structure that can be realized in a diatomic chain with alternating nearest-neighbor force constants, as depicted in Fig. 17. Assuming each atomic site has only one vibrational degree of freedom, the dynamical matrix for this system is given by:

$$D(k) = \frac{1}{m} \begin{pmatrix} K_1 + K_2 & -K_1 - K_2 e^{ika} \\ -K_1 - K_2 e^{-ika} & K_1 + K_2 \end{pmatrix}, \quad (55)$$

with K_1 and K_2 being the intra-cell and inter-cell force constants, respectively, and m is the atomic mass. k and a refer to the Bloch wave vector and the lattice constant, respectively. The model exhibits two distinct phonon branches: an acoustic branch with a lower frequency and an optical branch with a higher frequency. At the Γ point, where $k = 0$, the acoustic mode (A) with zero frequency is represented by the state $|u_1(k=0)\rangle = \frac{1}{\sqrt{2}}(1, 1)^T$, where the superscript T indicates the transpose of the vector. This mode is \mathcal{P} -odd, indicating it changes sign under spatial inversion. In contrast, the optical mode (O) at $k = 0$ is given by $|u_2(k=0)\rangle = \frac{1}{\sqrt{2}}(1, -1)^T$, which is \mathcal{P} -even, meaning it remains invariant under spatial inversion. This distinction in parity defines the conventional band ordering in the SSH model. The A mode resembles electronic bonding state which usually has lower energy compared to the O mode resembling electronic antibonding state. However, at X point, *i.e.* $k = \pi/a$, the band order of A and O modes depends on the model parameters K_1 and K_2 . When $K_1 > K_2$ the band order at X is the same as Γ which represents a normal order [Fig. 17(a)]; when $K_1 = K_2$ the two modes become degenerate at X [Fig. 17(b)]; when $K_1 < K_2$ the band order at X are inverted [Fig. 17(c)] indicating a non-trivial bulk topology.

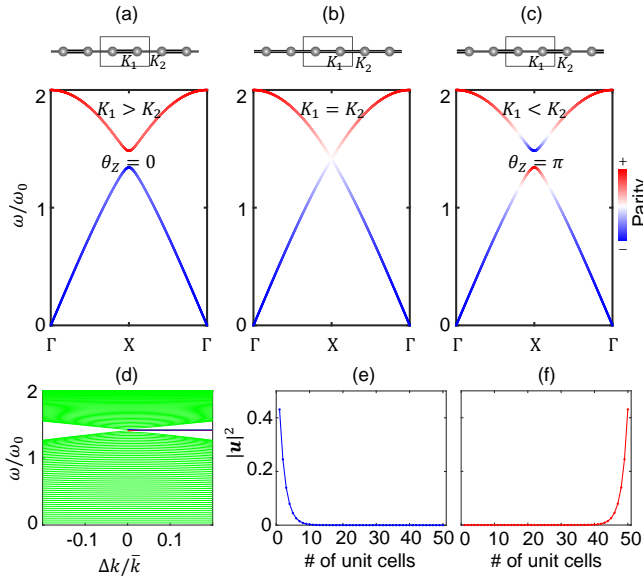


Figure 17 In a diatomic chain with one vibrational degree of freedom per atom, the phononic Su-Schrieffer-Heeger (SSH) model exhibits distinct topological characteristics: (a) For a topologically trivial phonon band structure, the intra-cell force constant K_1 exceeds the inter-cell force constant K_2 . This configuration yields a conventional band ordering where the out-of-phase mode (with parity $+$) is higher in energy than the in-phase mode (with parity $-$). (b) At the X point, a degeneracy occurs between the in-phase and out-of-phase modes when K_1 is equal to K_2 . (c) A topologically nontrivial phonon band emerges when K_1 is less than K_2 , resulting in an inverted band order between the Γ and X points. (d) The eigenmode spectrum ω is plotted for a finite chain comprising 50 unit cells, varying as a function of $\Delta K/\bar{K}$ ($\Delta K = K_2 - K_1$, $\bar{K} = (K_2 + K_1)/2$) under fixed boundary conditions. The reference frequency is given by $\omega_0 = \sqrt{\frac{\bar{K}}{m}}$. The red and blue curves denote the topological end (edge) states, with their respective wave displacement fields illustrated in figures (e) and (f). Adapted from Ref. (Liu *et al.*, 2020b).

According to Eq. (53), the Zak phase can be calculated as

$$\begin{aligned} \theta_Z &= \int_{-\pi/a}^{\pi/a} dk \, i \langle u_1(k) | \partial_k u_1(k) \rangle \\ &= \begin{cases} \pi & (K_2 > K_1) \\ 0 & (K_2 < K_1) \end{cases} \end{aligned} \quad (56)$$

The non-zero topological invariant θ_Z signifies the presence of edge states within the bulk band gap, as depicted in Fig. 17(d). The red and blue curves represent the in-gap edge states, which are localized at the left and right boundaries of the chain, respectively, as shown in Figs. 17(e)-(f). Notably, although such in-gap edge states often appear in various variants of the SSH model, they are not topological in general and their presence/absence depends on boundary conditions. Namely, this quantized Zak phase does have “bulk-boundary correspondence”. Only when the system has chiral symmetry, the bulk-boundary correspondence holds for the Zak phase, which is related to the winding number. The original SSH model for electrons has the chiral symmetry, but the phononic

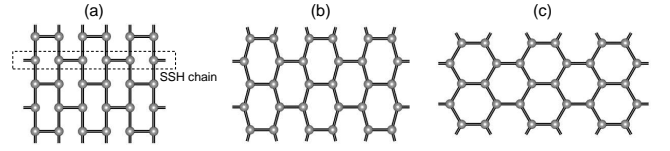


Figure 18 2D lattices that support a Dirac phonon phase include: (a) the brick lattice, which is constructed by stacking SSH chains and is capable of supporting a 2D Dirac phonon phase; (b) the stretched brick lattice, which is a variant of the brick lattice that similarly preserves a Dirac phonon phase; and (c) the honeycomb lattice, another well-known 2D lattice structure that maintains a Dirac phonon phase.

counterpart does not. However, in practice, in-gap edge states often emerge, in the cases of the nontrivial Zak phase, even when the chiral symmetry is absent. The phononic SSH model has been theoretically introduced in isostatic lattices (Kane and Lubensky, 2014) and has been experimentally observed in acoustic systems (Xiao *et al.*, 2015).

B. Topological Phonons in 2D: Honeycomb Lattice Model

In 2D systems, twofold Dirac phonons (different from the fourfold Dirac phonons in 3D systems) exemplify gapless topological states of phonons, characterized by a cone-shaped dispersion with a nonzero Berry phase of π for a closed trajectory encircling the Dirac phonon. These phononic states are typically protected by \mathcal{PT} symmetry or mirror symmetry. In contrast to the twofold Weyl phonons in 3D systems, the topological nature of Dirac phonons relies on symmetry protection; the breaking of such symmetries can lead to the opening of a gap at the Dirac points. A codimension analysis reveals a closer analogy between 2D Dirac phonons and 3D nodal-line phonons. In this section, we will briefly introduce the main results about Dirac phonons in 2D.

In his 1928 seminal work, P. Dirac introduced the relativistic equation for electrons, capable of describing both massive and massless particles. The equation is $i\partial_t|\psi(t)\rangle = H|\psi(t)\rangle$ with the Hamiltonian $H = m\beta + \sum_i^d p_i\alpha_i$ ($\hbar = c = 1$) (Dirac, 1928). m and p_i are the mass and momentum, respectively, and d refers to the spatial dimension. In order that the Dirac equation can reproduce the Klein-Gordon equation $(\mathbf{p}^2 + m^2 - \partial_t^2)|\psi\rangle = 0$, the introduced β and α_i must satisfy $\beta^2 = \alpha_i^2 = 1$, $\{\alpha_i, \alpha_j\} = 2\delta_{ij}$, and $\{\beta, \alpha_i\} = 0$, which is the Clifford algebra. The anticommutation relations of α_i and β indicate that α_i and β must have matrix forms of which the smallest dimension is 2. In 2D case, *i.e.* $d = 2$, the Dirac matrices α_i and β have a simple representation: $\alpha_x = \sigma_x$, $\alpha_y = \sigma_y$, and $\beta = \sigma_z$ where $\sigma_{x,y,z}$ are Pauli matrices. Therefore, the 2D massive Hamiltonian is given as $H = k_x\sigma_x + k_y\sigma_y + m\sigma_z$. The case of $m = 0$ describes the massless Dirac fermions in graphene (Castro Neto *et al.*, 2009) at the Brillouin corners K and K' . The cone-shaped band dispersion, stemming from the honeycomb lattice geometry, is not confined to spinless electronic states, prompt-

ing extensive exploration of topological physical phenomena in photonic crystals (Lu *et al.*, 2014; Wu and Hu, 2015) and magnonic systems (Zhang *et al.*, 2013), and phonon systems (Liu *et al.*, 2020b).

The topological invariant of 2D Dirac phonons is characterized by the quantized Berry phase accumulated along the loop encircling the Dirac point, *i.e.* $\theta_B = \oint_C d\mathbf{k} \cdot \mathbf{A} = \pi$. The 2D Dirac phonon is protected by the combined symmetry of inversion and time-reversal, denoted \mathcal{PT} . Upon symmetry breaking, 2D Dirac phonons can transition into a variety of topologically gapped phases, such as Quantum Anomalous Hall (QAH), Quantum Spin Hall (QSH), and Quantum Valley Hall (QVH), among others.

In electronic systems, the 2D Dirac semimetal with gapless Dirac cones is the parent phase for the QH family (Liu *et al.*, 2020b, 2018) which typically exist in honeycomb lattices. This principle can be extended to phononic systems as well. The 2D Dirac states can be constructed from stacked 1D SSH models, *i.e.* the brick lattice model, as shown in Fig. 18. The honeycomb lattice can be obtained by gradually stretching the brick lattice without closing or opening band gaps.

Figure 19(a) shows a phononic model on a deformed honeycomb lattice with lattice constants $\mathbf{a}_1 = (a_x, a_y) = a(1 + \cos \phi, \sin \phi)$ (a is the nearest-neighbor atomic distance) and $\mathbf{a}_2 = (a_x, -a_y)$. The conventional honeycomb lattice corresponds to the special case of $\phi = \pi/3$. The dynamical matrix of this lattice model is given by

$$D(\mathbf{k}) = \frac{1}{m} \begin{pmatrix} 3K & -K - \tilde{K}e^{-ik_x a_x} \\ -K - \tilde{K}e^{ik_x a_x} & 3K \end{pmatrix}, \quad (57)$$

$$\tilde{K} = 2K \cos(k_y a_y).$$

Building upon the SSH model discussed earlier, the system at a constant k_y exhibits a topologically nontrivial (trivial) band structure, characterized by an inverted (normal) band order along each k_x line when $\tilde{K} > K$ ($\tilde{K} < K$), as shown in Fig. 17(b). The case where $\tilde{K} = K$ represents a critical condition, resulting in a 1D band structure along k_x with a vanishing gap at $k_x = \pi/a_x$, thereby forming a pair of Dirac cones at $(\pi/a_x, \pm\pi/3a_y)$, as shown in Fig. 17(c). These Dirac points are protected by \mathcal{PT} , ensuring that the Berry phase accumulated around any loop encircling a Dirac point is π , as evidenced by the abrupt discontinuity in the Zak phase $\theta_Z^x(k_y) = \int_0^{2b_x} dk_x i \langle u_1(k_x, k_y) | \partial_{k_x} u_1(k_x, k_y) \rangle$ near $k_y = \pm\pi/3a_y$ [Fig. 17(d)]. The nonzero Zak phase can support localized edge modes, as depicted in the edge state spectrum of a 1D periodic ribbon of finite width along the x -direction in Fig. 17(e).

Graphene serves as a typical example of a 2D topological Dirac phonon, distinguished by a nonzero Berry phase of π . The topological nature of the Dirac phonon in 2D differs from that of the Weyl phonon in 3D; whereas the former requires symmetry protection, such as \mathcal{PT} symmetry or mirror symmetry, the latter maintains topological stability irrespective of symmetry, being characterized by a nonzero Chern number. In this context, the 2D Dirac phonons can be conceptualized

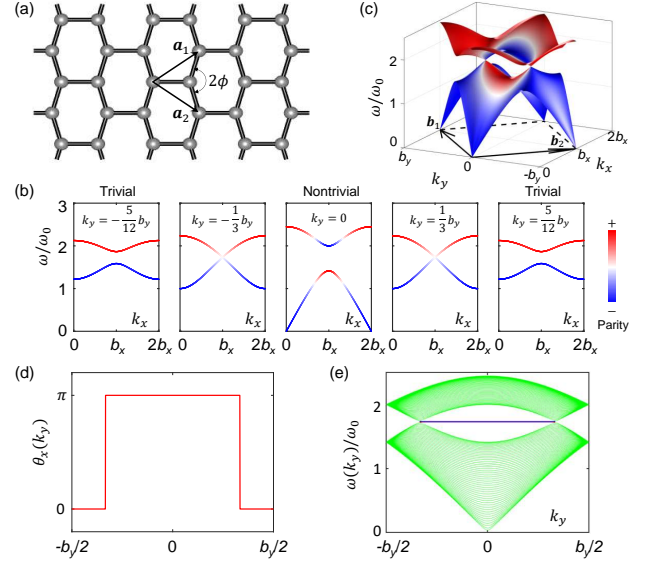


Figure 19 (a) Phononic model on a stretched brick lattice with lattice constants $\mathbf{a}_1 = (a_x, a_y) = a(1 + \cos \phi, \sin \phi)$, and $\mathbf{a}_2 = (a_x, -a_y)$. Its reciprocal lattice vectors are $\mathbf{b}_1 = (b_x, b_y) = (\pi/a_x, \pi/a_y)$ and $\mathbf{b}_2 = (b_x, -b_y)$. The honeycomb lattice corresponds to the case of $\phi = \pi/3$. (b) 1D phononic band structure as function of k_x for different k_y . The 1D phonon band is topologically nontrivial within the range $-b_y/3 < k_y < b_y/3$, and it reverts to a trivial state outside this interval. (c) 2D phononic band showing a pair of Dirac cones at $(b_x, \pm b_y/3)$. (d) Topological Zak phase $\theta_Z^x(k_y)$ calculated as function of k_y for each Wilson loop parallel to k_x axis. (e) Phononic band structure of a system with finite width along the y -axis and periodicity along the x -axis. The red and blue curves denote the topological edge states.

as an extension of the 1D SSH model, as both are classified by the same topological invariant.

C. Quantum Hall Family of Phonons

The quantum Hall family of phonons, encompassing QAH-, QSH-, and QVH- like states, can be realized by breaking specific symmetries in a honeycomb lattice (Liu *et al.*, 2020b), as illustrated in Fig. 20. The honeycomb lattice inherently supports a pair of Dirac cones at the Brillouin zone corners K and K' , characteristic of a 2D Dirac phonon phase, with each Dirac point associated with a quantized Berry phase of π for a loop enclosing it. Through mechanisms such as time-reversal symmetry breaking, inversion symmetry breaking, or Kekulé distortion, the Dirac cones can be gapped, leading to the emergence of topologically distinct phases, including the QAHE, QVHE, and QSHE.

1. Phononic Quantum Anomalous Hall (QAH)-like States

The quantum anomalous Hall (QAH) states in phonon systems, also known as phonon Chern insulators, represent two-

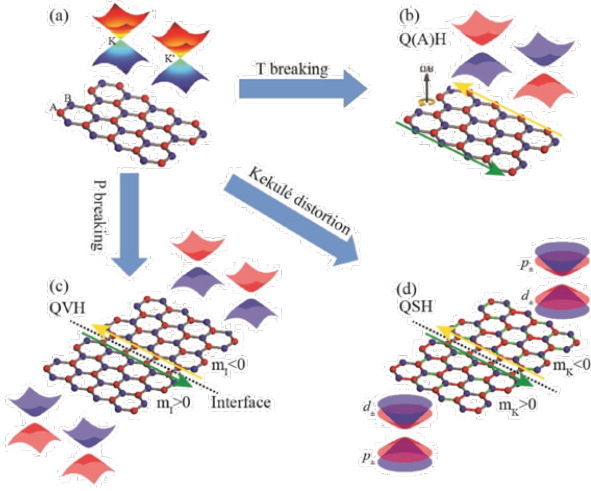


Figure 20 Various topological phonon states in 2D honeycomb lattices. (a) A honeycomb lattice hosts a 2D topological Dirac phonon phase, featuring a pair of Dirac cones at the Brillouin zone corners K and K' . (b)-(d) By breaking different symmetries, the Dirac cones can be gapped, leading to the emergence of topologically distinct phases, including (b) quantum (anomalous) Hall [Q(A)H], (c) quantum valley Hall (QVH), and (d) quantum (pseudo)-spin Hall (QSH) states. These phases arise from specific symmetry-breaking mechanisms, illustrating the rich topological landscape of phonons in 2D systems. Adapted from Ref. (Liu *et al.*, 2020b).

dimensional gapped phases distinguished by nonzero phonon Chern numbers. These topological invariants arise from the integration of the Berry curvature, $\Omega_z(\mathbf{k})$, over the Brillouin zone. Crucially, in the presence of time-reversal symmetry \mathcal{T} , the Berry curvature must be an odd function of momentum [$\Omega_z(-\mathbf{k}) = -\Omega_z(\mathbf{k})$]. This yields a zero Chern number. Consequently, the realization of a two-dimensional phonon Chern insulator inherently requires breaking \mathcal{T} symmetry in the phonon system. Within the ten-fold way classification, the phonon QAH effect belongs to the “A” class, as illustrated in Figs. 3 and 4.

The ordinary lattice Hamiltonian comprises a kinetic energy term $T = \sum_i \frac{1}{2} \dot{u}_i^2$ (where u_i is the mass-weighted displacement of the i -th vibrational mode) and a harmonic potential energy term $V = \sum_{i,j} \frac{1}{2} K_{ij} u_i u_j$, both explicitly preserving time-reversal symmetry \mathcal{T} . To break \mathcal{T} in phonon systems, a velocity-displacement bilinear term $\sum_{i,j} \eta_{ij} \dot{u}_i u_j$ was first introduced in microtubule models by (Prodan and Prodan, 2009a). This interaction term was later employed to study the topological phonon Hall effect (Zhang *et al.*, 2010) and topological phonon band structures (Huber, 2016b; Liu *et al.*, 2017b; Süssstrunk and Huber, 2016; Wang *et al.*, 2015b).

The honeycomb lattice serves as a prototypical topological system, exhibiting rich tunable topological phenomena. Its in-plane vibrational modes host a pair of Dirac cones at the K and K' points of the Brillouin zone. The effective $k \cdot p$ Hamiltonian near these Dirac points mirrors graphene’s low-

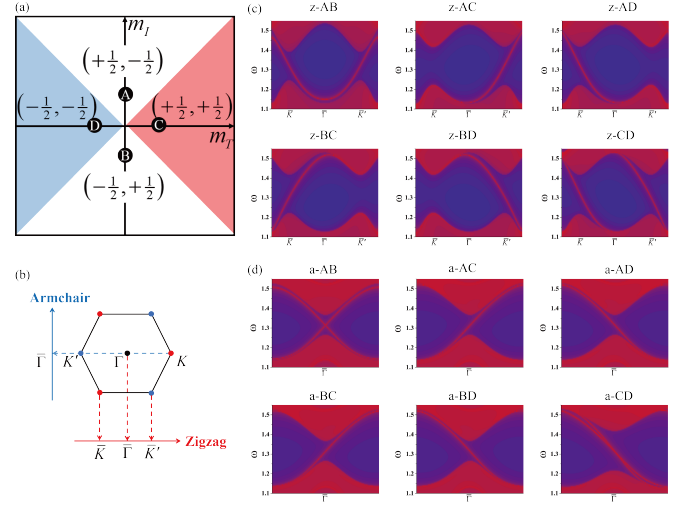


Figure 21 The honeycomb lattice model governed by $H_0 + H_I + H_T$ (Eqs. (58), (60), (59)) hosts valley-polarized topological boundary states due to the interplay of symmetry-breaking terms H_I (e.g., inversion-symmetry-breaking mass) and H_T (e.g., time-reversal-symmetry-breaking flux). (a) Topological phase diagram illustrating the valley Chern number pair $(c_K, c_{K'})$ as function of parameters m_T and m_I . The diagram is partitioned into four distinct regions by the critical lines $|m_I| = |m_T|$. Representative points A, B, C, and D in each region exhibit nearly quantized valley Chern numbers of $\pm \frac{1}{2}$. (b) Schematic of the 2D Brillouin zone and its projection onto the 1D boundaries. For zigzag boundary, the valleys K and K' project to distinct edge k points \bar{K} and \bar{K}' , respectively, while for armchair boundary, both valleys coalesce at the high-symmetry point $\bar{\Gamma}$. (c)-(d) Calculated spectral function of states for (c) zigzag and (d) armchair boundaries, respectively.

energy model and is expressed as:

$$H_0 = v_D(k_y \tau_z \sigma_x - k_x \sigma_y), \quad (58)$$

where v_D refers to the group velocity at the phononic Dirac points; σ and τ are Pauli matrices acting on the sublattice and valley subspaces, respectively. Symmetry-breaking mass terms can be introduced into Eq. (58), opening band gaps and driving the system into distinct topological phases.

The quantum anomalous Hall like states of phonons is described by $H_0 + H_T$ with

$$H_T = m_T \sigma_z \tau_z \quad (59)$$

being the Haldane-type mass term (Liu *et al.*, 2018, 2017b).

2. Phononic Quantum Valley Hall (QVH)-like States

The quantum anomalous Hall (QAH)-like states of phonon, characterized by the nonzero Chern number C , require the breaking of time-reversal symmetry \mathcal{T} in the phonon system. In systems where \mathcal{T} is preserved, the total Chern number must vanish. However, integration of Berry curvature around the Dirac points K and K' can be nonzero when a finite band gap is opened by breaking the spatial inversion symmetry \mathcal{P} .

The effective model of QVH of phonons is given by $H_0 + H_I$ with

$$H_I = m_I \sigma_z \quad (60)$$

being the Semenoff-type mass term. For a small mass m_I , the Berry curvature distribution becomes predominantly concentrated around the two valleys K and K' , which leads to nearly quantized valley Chern numbers $c_K = c_{K'} = \pm \frac{1}{2}$. The contrasting Chern numbers between the valleys facilitate the formation of a pair of valley-polarized topological boundary states. These states are characterized by a sign change in the mass m_I across them, resulting in a shift in the valley Chern numbers c_K and $c_{K'}$ by ± 1 , as illustrated in Fig. 16(c). Such valley-polarized topological boundary states have been the subject of extensive research in various systems, including acoustic systems (Xue *et al.*, 2022; Zhang *et al.*, 2018c; Zheng *et al.*, 2020), mechanical lattices (Lu *et al.*, 2018; Zhang *et al.*, 2018b), phononic crystals (Liu *et al.*, 2020b; Xia *et al.*, 2022; Zhang *et al.*, 2022a), and so on (Liu *et al.*, 2021b; Wu *et al.*, 2017).

When both \mathcal{P} and \mathcal{T} symmetries are simultaneously broken, that is, when both m_I and m_T are nonzero, the variation in m_I and m_T results in the valley Chern numbers c_K and $c_{K'}$ being determined as follows:

$$\begin{aligned} c_K &= \frac{1}{2} \text{sgn}(m_T + m_I), \\ c_{K'} &= \frac{1}{2} \text{sgn}(m_T - m_I), \end{aligned} \quad (61)$$

which gives rise to the topological phase diagram shown in Fig. 21.

3. Phononic Quantum Spin Hall (QSH)-like States

The quantum anomalous Hall (QAH)-like states of phonons or phonon Chern insulators requires the breaking of \mathcal{T} symmetry for phonons. However, achieving \mathcal{T} -symmetry breaking in phonons is inherently challenging due to their charge-neutral nature and weak coupling to external electric or magnetic fields. In contrast, the quantum spin Hall (QSH) effect represents a prominent class of topological states characterized by spin-momentum-locked helical boundary states (Hasan and Kane, 2010; Kane and Mele, 2005; Qi and Zhang, 2010b, 2011). The QSH state can be interpreted as two superimposed copies of QAH states with opposite Chern numbers, ensuring cancellation of the net Chern number while preserving \mathcal{T} . Its effective Hamiltonian is expressed as $H_{\text{QSH}} = H_0 + H_S$ with

$$H_S = m_S \sigma_z \tau_z s_z. \quad (62)$$

s_z denotes the spin Pauli matrix. Historically, numerous pseudospin degrees of freedom have been introduced to emulate the quantum spin Hall (QSH) states within phononic systems. Examples include intricate mechanical structures, as observed

in (Süsstrunk and Huber, 2015), and bilayer lattices, as discussed in (Pal *et al.*, 2016), among others.

The additional spin degree of freedom requires a four-band model as the minimum requirement to realize QSH. In 2015, (Süsstrunk and Huber, 2015) successfully constructed a mechanical topological insulator which mimics the Kane-Mele model (Kane and Mele, 2005) as shown in Eq. (62). (Wu and Hu, 2015) designed a four-band “double Dirac cone” model within a photonic honeycomb lattice characterized by a Kekulé pattern. This “double Dirac cone” arises from the folding of single Dirac cones originating from the K and K' points. (Liu *et al.*, 2017a) discovered phononic pseudospins in the Kekulé lattice, exhibiting quantized pseud-angular momenta and pseudospin-polarized Berry curvature, which support pseudospin-polarized helical boundary modes that are immune to disorder-induced scattering.

D. Phononic Stiefel-Whitney Insulator

The phononic quantum Hall (QH) family originates from the Berry curvature of phonon band structures. In 2D materials, the combined \mathcal{PT} or $C_2\mathcal{T}$ symmetry enforces a vanishing phononic Berry curvature across the entire Brillouin zone. Nevertheless, a topological invariant—the Stiefel-Whitney (SW) number w_2 can still be defined using parity eigenvalues at time-reversal invariant momenta (TRIM) below a phononic band gap. In 3D materials, the second SW number characterize the interlocking topology of \mathbb{Z}_2 nodal lines which must exist in pairs (Ahn *et al.*, 2018; Fang *et al.*, 2015). In contrast, the topological nodal lines with Berry flux π , *i.e.* a nonzero first SW number $w_1 = 1$, can exist alone (Ahn *et al.*, 2019).

Under \mathcal{PT} or $C_2\mathcal{T}$ symmetry, all phononic eigenvectors can be chosen to be real. The topology of such real vectors in Hilbert space is characterized by a \mathbb{Z}_2 index, *e.g.*, the second SW number w_2 , which is determined by

$$(-1)^{w_2} = \prod_{i=1}^4 (-1)^{[N^-(\Lambda_i)/2]}, \quad (63)$$

where Λ_i ($i = 1, 2, 3, 4$) denotes four TRIM in 2D Brillouin zone, and $N^-(\Lambda_i)$ counts the number of negative-parity eigenmodes at Λ_i below a given band gap. $[\cdot]$ refers to the floor function. The 2D gapped phononic band structures with nonzero w_2 is called phononic SW insulator or phononic real Chern insulator (Ding *et al.*, 2024). The value of w_2 can alternatively be determined from the spectrum of the Wilson loop operator:

$$\hat{W}(k_\perp) = \exp \left[-i \oint_C dk_\parallel \hat{\mathcal{A}}_\parallel(k_\parallel, k_\perp) \right] \quad (64)$$

where $\hat{\mathcal{A}}$ refers to the nonabelian Berry connection whose matrix elements is $\mathcal{A}_{nm} = i \langle u_n | \nabla_{\mathbf{k}} u_m \rangle$ with n and m being the band indexes below the gap. C is the Wilson loop parallel to k_\parallel at fixed k_\perp . Since the Wilson operator is unitary, its eigenvalues take the form $\exp[-i\theta(k_\perp)]$. In electronic systems,

$\theta(k_{\perp})$ corresponds to the electric charge polarization, which is proportional to the Wannier centers of charge. The phase $\theta(k_{\perp})$ is only defined modulo 2π , with its principal value within $[0, 2\pi]$. Let the number of times $\Theta = \theta(k_{\perp})$ crosses with $\Theta = \pi$ be N . The parity of N (even for $w_2 = 0$ and odd for $w_2 = 1$) constitutes a \mathcal{PT} or $C_{2z}\mathcal{T}$ -protected topological invariant, yielding the second Stiefel-Whitney number:

$$w_2 = N \bmod 2. \quad (65)$$

The atomic insulator exhibits a trivial band gap with $w_2 = 0$. In contrast, a nontrivial SW insulator can be realized through a double band inversion at certain TRIM as indicated by Eq. (63). Regarding “bulk-boundary correspondence”, the SW insulator is a second-order topological insulator rather than first-order. This is because the protecting symmetry, either \mathcal{P} or C_{2z} , is typically broken at the 1D open boundary, resulting in gapped edge states. Consequently, a 2D SW insulator with $w_2 = 1$ supports topological corner modes, characteristic of its second-order nature. As an example, (Pan and Huang, 2022) demonstrated the phononic SW phase in two-dimensional Xenex and their ligand-functionalized derivatives. Beyond these examples, \mathcal{PT} -symmetric topological phononic modes have also been explored in Kekulé lattices (Liu et al., 2017a), including graphdiyne (Zhang et al., 2023c), hydrogen-substituted graphdiyne (Mu et al., 2022), and C_3N compound (Huang et al., 2023).

IV. EXAMPLES OF TOPOLOGICAL PHONONS: 3D BULK MATERIALS

The application of first-principles calculations in condensed matter physics and materials science has expanded significantly with the routine implementation of phonon calculations over the past decade. Density functional theory (DFT) for solids provides second-order force constants, enabling the determination of phonon spectra and topological properties. However, prior to 2018, research on topological phonons remained largely theoretical, with limited exploration of real materials in solid-state phonon systems. This gap arose because the calculation of phonon spectra requires solving real-space force constants (typically truncated at second order), a far more computationally demanding task than electronic structure calculations. Furthermore, studying phonon surface states necessitates supercell structures that break periodic boundary conditions, adding to the computational burden. As a result, the heavy computational cost has long hindered progress in understanding topological states in phonon systems.

In 2018, (Zhang et al., 2018a) recognized that the solution to this heavy calculation challenge could be adapted from electronic systems. To simplify electronic surface state calculations, tight-binding models based on localized Wannier functions are typically employed. This approach allows topological surface states to be determined by extending the

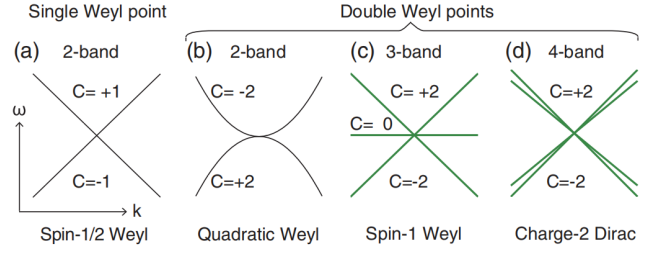


Figure 22 (a) Conventional Weyl phonon. (b-c) Three types of double-Weyl phonons with $|C| = 2$, where (b) is the twofold quadratic Weyl point carrying Chern numbers of ± 2 for each band, (c) is the threefold spin-1 Weyl point with Chern numbers of 0, ± 2 for each band, and (d) is the fourfold charge-2 Dirac point exhibiting Chern numbers of ± 2 for each phonon band pair. (Zhang et al., 2018a) refer to the quadratic Weyl, spin-1 Weyl, and charge-2 Dirac phonons as double-Weyl phonons. Adapted from Ref. (Zhang et al., 2018a).

model Hamiltonian and iteratively solving the Green’s function of a semi-infinite system. (Zhang et al., 2018a) observed that the second-order force constant matrix parameters, derived from real-space atomic displacement forces, exhibit formal similarities to p -orbital hopping terms in electronic systems. This analogy enables the extension of first-principles tight-binding methods from electronic structure calculations to phonon spectra. Consequently, this methodology can be applied to predict topological phonon materials and compute their surface states with significantly reduced computational cost.

This section examines materials exhibiting distinct topological phases in their phonon spectra. All considered systems preserve time-reversal symmetry \mathcal{T} , displaying gapless states with varying band degeneracies, typically protected by crystalline symmetries, as well as gapped topological phases analogous to “obstructed atomic insulators”. We systematically classify these topological phonons in Secs. IV.A and IV.B according to the codimension, dispersion and configuration of the band degeneracy. For each category, we discuss corresponding topological invariants, characteristic surface states and material realizations from first-principles calculations. The subsequent sections will present topological phonons with “obstructed atomic insulators” analogous states in Sec. IV.C and high-throughput computational results and the topological phonon materials database in Sec. IV.D.

A. Topological Phonons with 0D Degeneracies

The simplest topological phonon with a 0D degeneracy is the Weyl phonon, conventionally characterized by a Chern number of $C = \pm 1$, as shown in Fig. 22 (a). Such a Weyl phonon can be described by the two-band Hamiltonian of $H(\mathbf{k}) = \mathbf{k} \cdot \mathbf{S} = \frac{\hbar}{2} \mathbf{k} \cdot \boldsymbol{\sigma}$, where σ_i are the Pauli matrices and \mathbf{S} is the spin-1/2 rotation generator, hence the term spin-1/2 Weyl phonon. When the leading-order k -dependence is

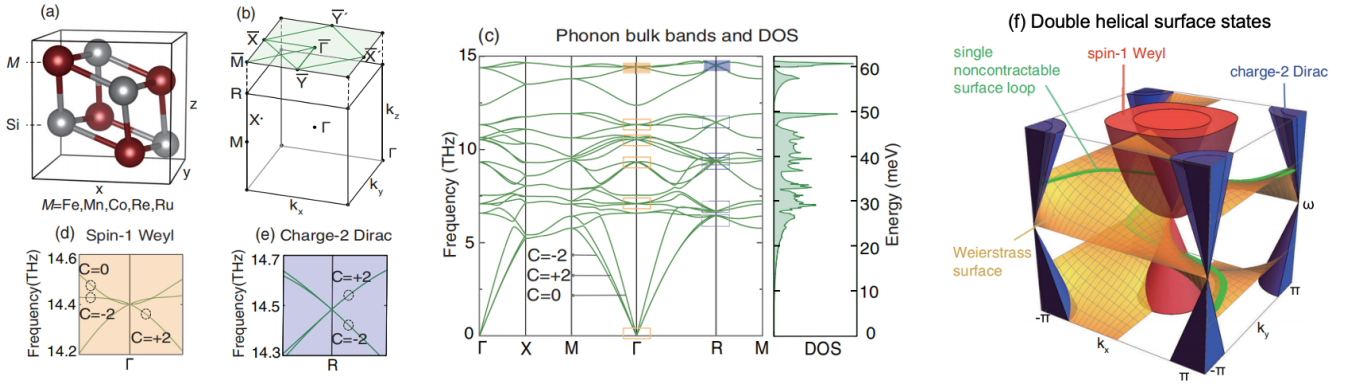


Figure 23 Crystal structure, phonon spectra, and topological phonons in the MSi family ($M = \text{Fe, Mn, Co, Re, Ru}$). (a) Crystal structure of the MSi family. (b) Bulk and (001) surface Brillouin zones. (c) Phonon dispersion of FeSi along high-symmetry lines in the Brillouin zone. The threefold acoustic phonons are spin-1 double Weyl phonons with Chern numbers of 0 and ± 2 . Orange and purple boxes highlight the spin-1 Weyl phonon at Γ and the charge-2 Dirac phonon at R, respectively. (d) The Γ point hosts a spin-1 Weyl phonon. (e) The R point exhibits a charge-2 Dirac phonon. (f) Double-helicoid surface states, described by the Weierstrass elliptic function. The spin-1 Weyl phonon (red cone) corresponds to a double zero point, while the charge-2 Dirac phonon (purple cone) represents a double pole. Two yellow sheets depict topological surface states rotating around these double-Weyl phonons. Adapted from Ref. (Zhang *et al.*, 2018a).

quadratic, unconventional Weyl phonons with Chern numbers of $C = \pm 2$ emerge, as described by Eq. (34) for $N = 2$. Due to their quadratic dispersion in the (k_x, k_y) plane, these are referred to as quadratic Weyl phonons, illustrated in Fig. 22 (b).

In addition to the case described by Eq. (34) with $N = 2$, double Weyl phonons can emerge in a three-band Hamiltonian $H(\mathbf{k}) = \mathbf{k} \cdot \mathbf{L}$, where \mathbf{L} represents the spin-1 rotation generators. The eigenvalues of $L_k = \mathbf{L} \cdot \mathbf{k} = \hbar, -\hbar, 0$ correspond to Chern numbers $+2, -2, 0$, doubling those of the spin-1/2 Weyl phonon. This motivates the term spin-1 Weyl phonon, as illustrated in Fig. 22 (c).

Another approach to generate double Weyl phonons with is by coupling two identical spin-1/2 Weyl phonons, described by the block-diagonal Hamiltonian of $H(\mathbf{k}) \sim \begin{pmatrix} \mathbf{k} \cdot \boldsymbol{\sigma} & 0 \\ 0 & \mathbf{k} \cdot \boldsymbol{\sigma} \end{pmatrix}$, resulting in a fourfold degenerate Weyl phonon, as shown in Fig. 22 (d). Unlike a conventional 3D Dirac point, composed of two Weyl points with opposite Chern numbers, this Dirac point exhibits a monopole charge of 2, thus it is also referred to “charge-2 Dirac phonon”.

1. B-20 Type Materials: Double Weyl Phonons

The first realizations of spin-1 Weyl phonons and charge-2 Dirac phonons were theoretically predicted in the phonon spectra of the MSi family ($M = \text{Fe, Co, Mn, Re, Ru}$), as shown in Fig. 23, with experimental confirmation following in the same year. MSi family belongs to the B-20 structure, a simple cubic crystal structure with space group $P2_13$ (#198), as shown in Fig. 23 (a). Figure 23 (b) is the BZ and surface BZ (green plane) along (001) direction. Using FeSi as a representative example, (Zhang *et al.*, 2018a) identified two types of double Weyl phonons in the MSi family. The phonon

spectrum shown in Fig. 23 (c) reveals that the three acoustic branches form a spin-1 Weyl phonon. Notably, in 3D chiral crystals, all acoustic phonons exhibit spin-1 Weyl character, where the longitudinal acoustic (LA) phonon carries a zero Chern number, and the two transverse acoustic (TA) phonons have Chern numbers of ± 2 . However, the topological surface states of the spin-1 Weyl phonon remain unobservable due to the absence of a bulk gap between the LA phonon branches.

In the optical phonon spectra of FeSi, all threefold-degenerate modes at the Γ point are spin-1 Weyl phonons, while all fourfold-degenerate modes at the R point are charge-2 Dirac phonons, as highlighted by orange and purple boxes in Figs. 23 (c)–(e). The spin-1 Weyl phonons are stabilized by chiral cubic symmetry, whereas the charge-2 Dirac phonon is protected by both crystalline symmetries and time-reversal symmetry \mathcal{T} . (Zhang *et al.*, 2018a) offered an intuitive perspective to understand the charge-2 Dirac phonon at R. MSi family materials possesses twofold screw rotations along each axis, such as $\{C_{2x} | (\frac{1}{2}, \frac{1}{2}, 0)\}$ along x axis, and the other two along y and z axes. These operations anti-commute with each other and satisfy $C_{2x/y/z}^2 = -1$ at R. Since such behavior is analogous to half-integer spin rotation, all irreducible representations at R must have even dimensions. Moreover, R is a time-reversal-invariant momentum and preserves \mathcal{T} , the screw rotations must also commute with \mathcal{T} , enforcing real matrix representations. The smallest allowed representation under these constraints is 4D, forcing all bands at R to form charge-2 Dirac phonons, a direct consequence of the interplay between crystalline symmetries and \mathcal{T} .

According to the “bulk-surface correspondence”, two surface states must connect these double Weyl phonons, topologically equivalent to helicoid noncompact Riemann sheets (Fang *et al.*, 2016). This allows the surface state dispersion near the Weyl phonon projections to be mapped to

Riemann surfaces of analytic functions, treating the surface momentum as a complex variable. As an illustrative example, consider the highest optical branch in FeSi (~ 14.5 THz). Figures 23 (d) and (e) show zoomed-in dispersions of the spin-1 Weyl phonon at Γ (monopole charge +2) and the charge-2 Dirac phonon at R (monopole charge -2), respectively. In the *MSi* family, Weyl phonons carry Chern numbers of $C = \pm 2$, making their (001) surface state dispersion topologically equivalent to the winding phase of the Weierstrass elliptic function (\wp). Specifically, the function has an order- C zero at $\mathbf{k}_- = (0, 0)$, and order- C pole at $\mathbf{k}_+ = (\pi, \pi)$:

$$\omega(k_x, k_y) \sim \wp(z; 2\pi, 2\pi) = \quad (66)$$

$$\text{Im}\left\{\log\left[\frac{1}{z^2} + \sum_{n \neq 0} \left(\frac{1}{(z + 2m\pi + 2n\pi i)^2} - \frac{1}{(2m\pi + 2n\pi i)^2}\right)\right]\right\},$$

where z represents the planar momentum relative to the Weyl phonon projection, defined as $z \equiv k - (1 + i)\pi$. As illustrated in Fig. 23 (f), the spin-1 Weyl phonon (red cone) projects to the center of the (001) surface Brillouin zone, while the charge-2 Dirac phonon (blue cone) projects to the Brillouin zone corner. The double-helicoid surface states of the *MSi* family are depicted as yellow sheets. The isoenergetic contour reveals surface arcs (green curves) with distinct topological features. Unlike conventional Weyl materials where surface arcs are open and terminate at bulk Weyl projections, the *MSi* family exhibits a single non-contractible loop that rotates around both double Weyl phonons as the energy contour varies.

It's worthy to note that all the twofold degeneracies at Γ are another type of Weyl phonons with $C = \pm 4$, referred to as twofold quadruple Weyl phonon (Li *et al.*, 2021a; Zhang *et al.*, 2020b), as mentioned in Sec. II.B.1. In solids, there are three distinct mechanisms to realize Weyl phonons with a monopole charge of 4, i.e., double spin-1 Weyl phonon, spin-3/2 Weyl phonon and twofold quadruple Weyl phonon, as shown in Figs. 24 (a), (b) and (c), respectively.

The sixfold double spin-1 Weyl node consists of two identical spin-1 Weyl phonons, with its monopole charge arising from the two lowest bands, as shown in Fig. 24 (a). The spin-3/2 Weyl phonon is described by a four-band Hamiltonian of $H(\mathbf{k}) = \mathbf{k} \cdot \mathbf{L}$, with \mathbf{L} representing the spin-3/2 rotation generators. This yields Chern numbers of +1, +3, -1, -3 for each band. Regarding twofold Weyl phonons, crystals can host three additional types with Chern numbers ± 1 , ± 2 and ± 3 , respectively. The twofold quadruple Weyl phonon with Chern numbers of ± 3 remained unrealized for an extended period (before 2020) due to the oversight of chiral cubic symmetry in topological band theory analyses. We will discuss the twofold Weyl quadruple phonon in detail in Sec. VII.

Xiao *et al.* pointed out that some kinds of nodal surface can carry integer-valued topological charge similar to Weyl monopoles, i.e. a topological phase transition can occur when the topological charge of the nodal surface changes by simultaneously emitting or absorbing integer numbers of Weyl

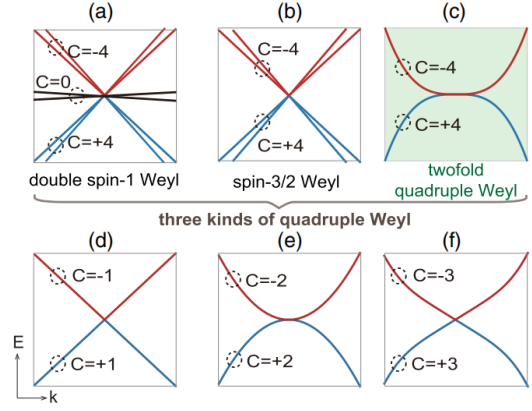


Figure 24 (a-c) Three kinds of Weyl phonons with the monopole charge of 4. (a) Sixfold double spin-1 Weyl phonon, which is a composite of two identical spin-1 Weyl phonons. (b) Fourfold spin-3/2 Weyl phonon with Chern numbers of +1, +3, -1, and -3 for each band. (c) Twofold quadruple Weyl phonon with Chern numbers of +4 and -4 for each band. (d-f) Three types of twofold Weyl phonons with distinct Chern numbers that can exist in crystals, with Chern numbers of ± 1 , ± 2 and ± 3 , respectively. Adapted from Ref. (Zhang *et al.*, 2020b).

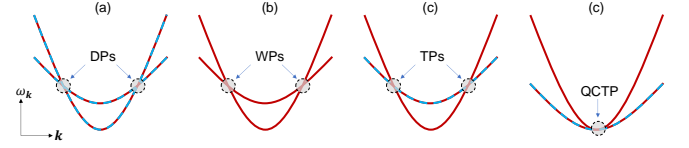


Figure 25 Schematic of phononic topological nodal points: (a) Dirac points (DPs), arising from the band crossings of two sets of doubly degenerate bands, (b) Weyl points (WPs), formed at the band crossing of two non-degenerate bands, (c) Triple points (TPs), formed by the crossing between one non-degenerate band and two doubly degenerate bands, and (d) Quadratic contact triple point (QCTP), characterized by a quadratic dispersion relation in the vicinity of the three-band touching point.

points (Xiao and Fan, 2017). In realistic materials, crystals with two-fold screw rotation symmetry $S_{2\alpha}$ ($\alpha = x, y, z$) can host nodal surface phonons at $k_\alpha = \pi$ when combined with time-reversal symmetry (Liu *et al.*, 2021d; Xie *et al.*, 2022, 2021). Consider a lattice invariant under the nonsymmorphic operation $S_{2x} = \{C_{2x} | [\frac{1}{2}00]\}$. Since $(S_{2x})^2 = \{E | [100]\}$ represents a primitive lattice translation along x (assuming lattice constant $a = 1$), Bloch's theorem gives $(S_{2x})^2 = e^{ik_x}$. At the Brillouin zone boundary $k_x = \pi$, the anti-unitary operator $S_{2x}\mathcal{T}$ satisfies $(S_{2x}\mathcal{T})^2 = (S_{2x})^2 = -1$, enforcing Kramers-like degeneracy across all bands and consequently generating a nodal surface phonon.

2. Face-centered Silicon: Triple Point Phonon

By definition, a topological Dirac point in a 3D system is a fourfold degenerate point formed by the crossing of two pairs of doubly degenerate bands, as illustrated in Fig. 25 (a). In

contrast, a topological Weyl phonon (with Chern number of $C = \pm 1$) arises from the crossing of two non-degenerate bands, shown in Fig. 25 (b). Between these two cases lies the topological triple point (TP) phonon, which emerges from a three-band crossing involving a doubly degenerate band and a single non-degenerate band [Fig. 25 (c)]. When these three bands exhibit quadratic touching, the degenerate point is termed a quadratic contact triple point (QCTP), as depicted in Fig. 25 (d).

In phonon systems, TPs typically emerge along high-symmetry lines with rotational symmetry C_n ($n \geq 3$). Here, the transverse (T) phonon modes form a doubly degenerate pair (corresponding to a 2D irreducible representation of the point group), while the longitudinal (L) phonon mode remains non-degenerate (a 1D representation). The crossing between the doubly degenerate T bands and the L band results in a symmetry-protected TP, which remains robust against gap opening as long as the rotational symmetry is preserved. In contrast, the QCTP is stabilized by cubic crystalline symmetry at certain high-symmetry points, where the L and T modes collectively form a 3D irreducible representation.

For TPs with the rotation axis aligned along the k_z -direction, the L mode can be described by a $|p_z\rangle$ -like orbital state, while the two degenerate T modes correspond to the chiral states $|p_x \pm ip_y\rangle$ states. In basis of $\{|p_x + ip_y\rangle, |p_x - ip_y\rangle, |p_z\rangle\}$, the 3-band effective Hamiltonian near a TP can be expressed as:

$$H_{\text{TP}} = \begin{pmatrix} v_T k_z & 0 & ck_+ \\ 0 & v_T k_z & ck_- \\ c^* k_- & c^* k_+ & v_L k_z \end{pmatrix} + O(k^2). \quad (67)$$

v_T and v_L refer to the group velocity of T and L modes, respectively, along k_z axis. c is a complex coupling constant. We define $k_{\pm} = k_x \pm ik_y$, and k_z are referenced to the TP. Without loss of generality, we suppose $v_T > v_L$, leading to the formation of a topological nexus (Fig. 26), where a nodal line arises between the lower (upper) two bands along the positive (negative) k_z -axis. Unlike conventional closed nodal lines, the nexus features open nodal line segments that terminate at the TPs. Within the degenerate subspace, the two-band effective Hamiltonian can be derived using the Löwdin partitioning method, yielding:

$$H_2 = \begin{pmatrix} 0 & Ak_z^2 \\ Ak_z^2 & 0 \end{pmatrix} = A[(k_x^2 - k_y^2)\sigma_x + 2k_x k_y \sigma_y], \quad (68)$$

up to an irrelevant band bending term and $A = \frac{|c|^2}{(v_T - v_L)k_z}$. This Hamiltonian exhibits a chiral symmetry expressed by the anti-commutation relation $\{\sigma_z, H_2\} = 0$, which enables the definition of the topological winding number:

$$n_W = \oint_C \frac{dl}{4\pi i} \text{Tr} [\sigma_z H_2^{-1} \partial_l H_2] = \pm 2. \quad (69)$$

The winding number n_W can be defined for any closed loop C encircling the k_z -axis at fixed k_z . A nonzero n_W directly

reflects the topological protection of the nodal structure and is further linked to the Euler characteristic of the band crossing, as demonstrated in (Park *et al.*, 2021).

The topology of TPs can also be understood by its topological phase transitions via symmetry breaking terms. When time-reversal symmetry \mathcal{T} is broken while rotational symmetry C_n is preserved, an additional term $H'_2 = \delta_T \sigma_z$ modifies the effective Hamiltonian H_2 . This splits each TP into Weyl point pairs, giving rise to double Fermi-arc-like surface states (Liu *et al.*, 2022). On the other hand, if the rotation symmetry C_n is broken (e.g., by external strain) while \mathcal{T} remains intact, a perturbation $H''_2 = \delta_S \sigma_x$ emerges. Unlike the \mathcal{T} -breaking case, H''_2 preserves line degeneracy but fragments the nexus into a set of nodal lines, whose positions are determined by

$$\begin{aligned} A(k_x^2 - k_y^2) + \delta_S &= 0, \\ k_x k_y &= 0. \end{aligned} \quad (70)$$

These nodal lines are characterized by a winding number $n_W = \pm 1$ and organize into interlocking Hopf-link chains in momentum space.

In cubic lattices with either T_d or O_h point group symmetry, the L and T modes at Γ point jointly form a three-dimensional irreducible representation. The symmetry-constrained effective Hamiltonian for this system takes the form:

$$H_{\text{QCTP}} = \omega_0 + A\mathbf{k}^2 + \begin{pmatrix} Bk_x^2 & Ck_x k_y & Ck_x k_z \\ Ck_y k_x & Bk_y^2 & Ck_y k_z \\ Ck_z k_x & Ck_z k_y & Bk_z^2 \end{pmatrix} \quad (71)$$

with A , B , and C being \mathbf{k} -independent constants. Here, ω_0 represents the frequency at $\mathbf{k} = 0$, which vanishes for acoustic branches due to the acoustic sum rule, resulting in a linear phonon dispersion near the zone center. This three-band crossing constitutes a topological acoustic triple point (TATP) (Park *et al.*, 2021). For optical branches, ω_0 remains finite, leading to quadratic $\mathbf{k} = 0$ -dependence of the dispersion and the formation of a quadratic contact triple point (QCTP). Remarkably, the QCTP hosts extended topological surface phonon states that persist across the entire Brillouin zone (Zhong *et al.*, 2021).

To date, numerous materials hosting phononic TPs and QCTPs have been theoretically predicted through first-principles calculations. (Li *et al.*, 2018) identified three-component Weyl phonons in WC-type compounds (TiS, ZrSe, HfTe) within the THz frequency range. Subsequent work by (Singh *et al.*, 2018) further explored these systems, emphasizing their thermoelectric properties. In CsCl, (Park *et al.*, 2021) demonstrated acoustic TPs with distinct topological invariants: the longitudinal mode carries a Skyrmion number, while the transverse modes are characterized by an Euler number. Phononic QCTPs have been reported in cubic materials such as $\text{Zr}_3\text{Ni}_3\text{Sb}_4$ (Zhong *et al.*, 2021), Ta_3Sn (Yang *et al.*, 2022), etc.

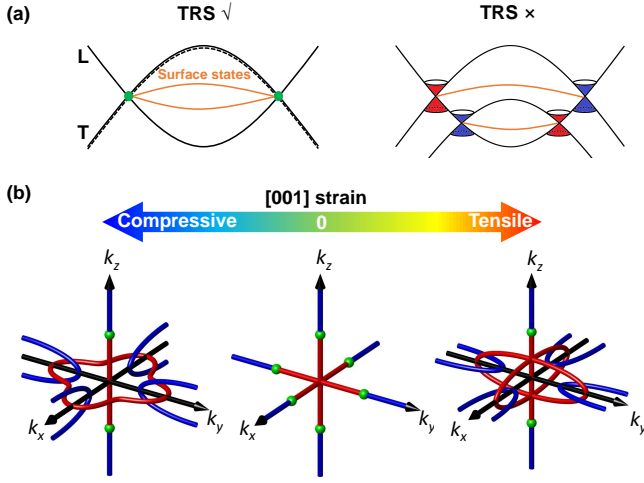


Figure 26 Triple point phonons in diamond-structure silicon. (a) Diamond-structure silicon with space group #227. (b) Phonon band structure of silicon with phononic TPs formed by band crossings between longitudinal optical (LO) and transverse optical (TO) branches along Γ -X. (c) Distribution of topological nodal lines (red solid) and TPs in momentum space. (d) Schematics of TPs and double-fermi-arc-like surface states under time-reversal symmetry (TRS). By breaking the TRS, the TPs are splitted into pairs of WPs which support single-fermi-arc surface states. (e) Under [001] uniaxial strain, TPs transform into interlocking nodal Hopf links. Adapted from Ref. (Liu *et al.*, 2022).

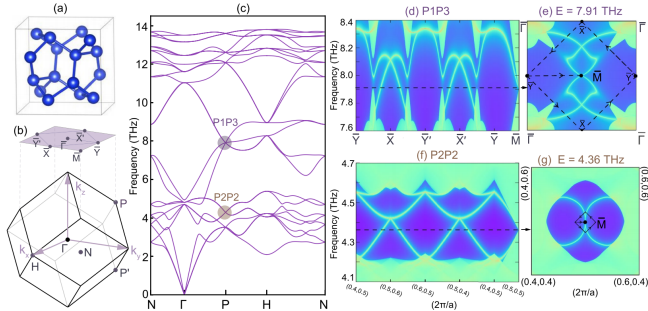


Figure 27 \mathbb{Z}_2 Dirac phonon in body-centered silicon with space group $Ia\bar{3}$. (a) Crystal structure of silicon. (b) Bulk Brillouin zone (BZ) and (001) surface BZ. (c) Phonon band structure, where the colored dots denote two distinct \mathbb{Z}_2 Dirac phonons, P_1P_3 and P_2P_2 , characterized by different irreducible representations (irreps). (d)-(e) Surface states and Fermi arcs associated with the \mathbb{Z}_2 Dirac phonons of irreps P_1P_3 . (f)-(g) Surface states and Fermi arcs corresponding to the \mathbb{Z}_2 Dirac phonons of irreps P_2P_2 . Adapted from Ref. (Zhang and Murakami, 2023).

3. Body-centered Silicon: \mathbb{Z}_2 Dirac Phonon

As discussed in Sec. II.B, conventional Dirac phonons are topologically trivial because they consist of two Weyl phonons with opposite Chern numbers, which do not guarantee gapless helicoid surface states. To provide an intuitive understanding of \mathbb{Z}_2 Dirac phonons and their characteristic anti-parallel helical surface states, we will take an experimentally synthesized material candidate as an example in this subsection, showing

their topological properties (Zhang and Murakami, 2023).

Figures 27 (a)–(c) show the crystal structure, Brillouin zone, and phonon spectra of silicon in its experimentally synthesized phase (space group #206). The system hosts two perpendicular glide mirrors, i.e., $G_x = \{M_x|0\frac{1}{2}0\}$ and $G_y = \{M_y|0\frac{1}{2}0\}$, which enforce fourfold degenerate bands at the T -related high-symmetry points P and P' . All the fourfold degenerate phonons shown in Fig. 27 (c) are \mathbb{Z}_2 Dirac phonons with irreducible representations of either P_2P_2 or P_1P_3 , carrying a nonzero monopole charge Q .

Figure 27 (d) displays the (001) surface states for the P_1P_3 Dirac points identified in Fig. 27 (c), with the corresponding k -path shown in the surface arc calculation. The (001) surface Brillouin zone possesses two \mathcal{TG} symmetries, where $(\mathcal{TG}_x)^2 = -1$ and $(\mathcal{TG}_y)^2 = -1$ along the BZ boundaries $\bar{M}-\bar{X}$ and $\bar{M}-\bar{Y}$. These symmetries enforce Kramers-like degeneracy, resulting in doubly degenerate surface states along these boundaries. The \mathbb{Z}_2 Dirac phonons at P and P' project onto the BZ corner (\bar{M}), generating two pairs of anti-parallel surface states along the path $\bar{Y}-\bar{X}-\bar{Y}'-\bar{X}'-\bar{Y}$ in Fig. 27 (d). Four anti-parallel helical surface states cross along $\bar{X}-\bar{M}-\bar{X}'$, with their gapless intersection protected by \mathcal{TG}_x . All topological surface states ultimately merge into the \mathbb{Z}_2 Dirac cone at \bar{M} .

Similarly, Figs. 27 (f) and (g) show the surface states and arcs for the P_2P_2 Dirac phonon, which also exhibit two pairs of anti-parallel helical surface states around \bar{M} . Thus, both the P_2P_2 and P_1P_3 Dirac phonons in silicon's phonon spectrum are \mathbb{Z}_2 Dirac phonons, each hosting two pairs of anti-parallel helical surface states (termed anti-parallel quad-helical surface states in (Zhang and Murakami, 2023)). The (anti-)parallel quad-helical surface states represent the maximal number of surface states achievable for (Dirac) Weyl phonons in solids, as constrained by onsite and crystalline symmetries.

B. Topological Phonons with 1D Degeneracies

Conceptually, phonons exhibit topological properties analogous to those of spinless electrons. However, in electronic systems, topological degeneracies are typically lifted by finite spin-orbit coupling (SOC) unless protected by additional symmetries. In contrast, phononic systems can host robust topological nodal lines/rings because SOC is inherently absent. In this subsection, we take MoB_2 as a prototypical example to illustrate nodal line phonons and their unique features in solids. Other nodal line/ring phonons, as well as their extensions, will be discussed in the next subsection.

MoB_2 crystallizes in the centrosymmetric space group $R\bar{3}m$ (# 166), with its crystal structure and primitive cell illustrated in Fig. 28 (a). The system features two distinct boron layers: B_1 forms a planar quasi-2D honeycomb lattice, while B_2 constitutes a buckled honeycomb network. The phonon spectrum and density of states (DOS), presented in Fig. 28 (b), confirm the dynamical stability of MoB_2 , as evidenced by the

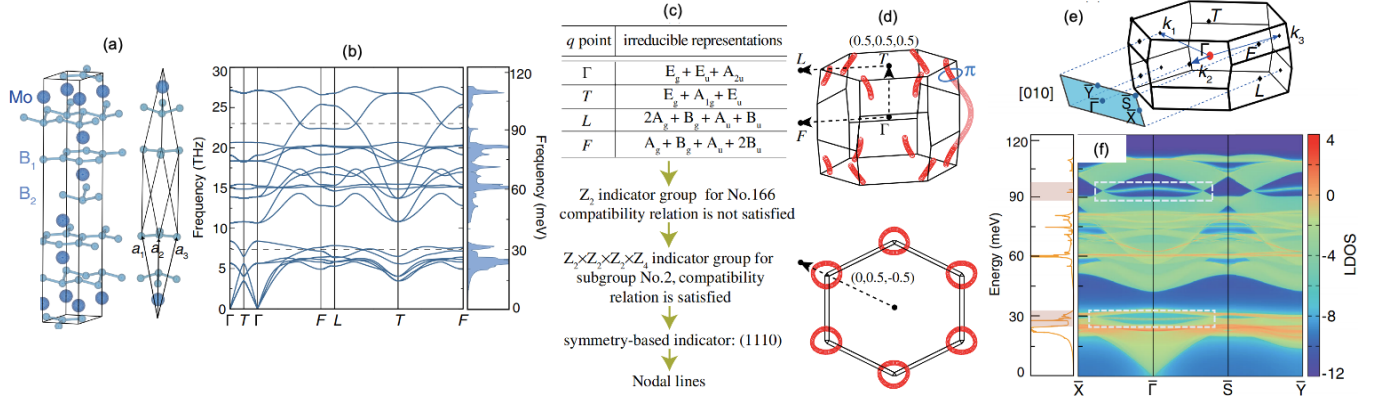


Figure 28 (a) Conventional and primitive unit cells of MoB₂. (b) Phonon spectra of MoB₂. (c) Topological nodal line identification in MoB₂, determined through compatibility relations and symmetry-based indicator analysis. (d)-(e) Side view and [111]-oriented top view of the nodal lines near 30 meV in MoB₂, exhibiting a quantized π Berry phase. (f) Bulk Brillouin zone and [010]-projected surface BZ of MoB₂. (010) surface local density of states (LDOS), showing both bulk-derived modes and surface-unique modes (left panel: integrated intensity). Drumhead surface phonon states (within white dashed rectangles) connecting nodal line crossings display maximal LDOS, as evidenced by sharp intensity peaks at nodal-line energies (shaded regions). Adapted from Ref. (Zhang *et al.*, 2019b).

absence of imaginary frequencies. While band crossings appear throughout the spectrum, two particularly interesting features emerge at approximately 7.25 THz and 23 THz (marked by black dashed lines). These crossings correspond to \mathcal{PT} -protected nodal lines carrying a \mathbb{Z}_2 monopole charge, forming six helical nodal lines that extend through the Brillouin zone along the k_z direction. Notably, the phonon DOS exhibits local minima at these characteristic frequencies, consistent with the expected nodal dispersion feature.

We focus on the band crossings at 7.25 THz (30 meV) to reveal their topological nature and full configuration. Following the symmetry-based indicator theory and related frameworks (Po *et al.*, 2017; Song *et al.*, 2018; Zhang *et al.*, 2020a) introduced in Sec. II.C, we analyze these features as shown in Fig. 28 (c). For space group No. 166 ($R\bar{3}m$), which possesses a nontrivial symmetry-based indicator group, we first determine the irreducible representations (irreps) of all five phonon bands below 7.25 THz at high-symmetry points Γ , T , F , and L through first-principles calculations. However, the compatibility relationships for these irreps in space group # 166 are not satisfied, indicating band inversions between the 5th and 6th phonon modes. This renders the symmetry-based indicator theory inapplicable for the parent space group.

We therefore identify subgroups of # 166 that satisfy two key criteria:

- The irreps must fulfill the compatibility relations within the subgroup
- The subgroup must have a nontrivial symmetry-based indicator group

Space group # 2 ($P\bar{1}$) meets these requirements, allowing us to apply its symmetry-based indicator formulas:

$$z_{2,i} = \sum_{q \in \text{TRIM at } \{q_i = \pi\}} \frac{N_-(q) - N_+(q)}{2} \bmod 2, i = 1, 2, 3 \quad (72)$$

$$z_4 = \sum_{q \in \text{TRIM}} \frac{N_-(q) - N_+(q)}{2} \bmod 4 \quad (73)$$

For MoB₂, our symmetry analysis yields the indicator $z_{2,1}z_{2,2}z_{2,3}z_{2,4}z_4 = (1110)$. Following the theory outlined in Sec. II.C (Eqs. 72 and 73) (Song *et al.*, 2018; Zhang *et al.*, 2020a), this indicator predicts:

1. The existence of $2 \bmod 4$ nodal lines along the [111] direction in the Brillouin zone
2. The π Berry phase of each nodal line, as shown in Fig. 28 (d)
3. The \mathbb{Z}_2 monopole charge of each nodal line

These topological features manifest as nodal lines that extend throughout the Brillouin zone. Crucially, their topological protection ensures robustness against any small perturbations that preserve \mathcal{PT} symmetry.

To demonstrate the topological surface states associated with these \mathcal{PT} -protected nodal lines, we present the local density of states (LDOS) along the (010) direction in Fig. 28 (f), corresponding to the surface Brillouin zone shown in Fig. 28 (e). Unlike Weyl points that exhibit helicoid surface modes (Fang *et al.*, 2016; Miao *et al.*, 2018; Zhang *et al.*, 2022b; Zhang and Murakami, 2023; Zhang *et al.*, 2018a, 2020b), the nodal lines generate characteristic drumhead-shaped surface states, as indicated by the white dashed box.

Notably, while the bulk phonon density of states shows minima near ~ 7.25 THz and ~ 23 THz, the surface modes display a pronounced peak in LDOS at these energies (Fig. 28 b). The flat surface states could induce electronic anomalies through electron-phonon coupling, potentially leading to unique surface phenomena.

For any generic two-band system, the low-energy effective Hamiltonian can be expressed in terms of Pauli matrices as:

$$H_{2\text{band}} = \varepsilon(\mathbf{k}) + h_1(\mathbf{k})\sigma_x + h_2(\mathbf{k})\sigma_y + h_3(\mathbf{k})\sigma_z, \quad (74)$$

where $h_{1,2,3}$ are arbitrary real functions of \mathbf{k} . For phononic systems with \mathcal{PT} symmetry, the dynamical matrix and eigenvectors can be made real at any \mathbf{k} point, which means $h_2(\mathbf{k}) = 0$. The location of nodal line is thus determined by the condition:

$$h_1(\mathbf{k}) = h_3(\mathbf{k}) = 0 \quad (75)$$

In 2D systems, Eq. (75) typically defines isolated \mathbf{k} -points, corresponding to 2D Dirac semimetals (Jin *et al.*, 2018b; Li *et al.*, 2020a). In 3D systems, however, the same condition can be satisfied along closed \mathbf{k} -space contours, giving rise to topological phononic nodal lines. Numerous material candidates hosting such nodal lines have been theoretically predicted and experimentally observed. Based on their geometric configurations, these nodal lines can be categorized into several distinct types: helical nodal lines (Zhang *et al.*, 2019b), straight nodal lines (Li *et al.*, 2020b; Liu *et al.*, 2021a), nodal rings (Jin *et al.*, 2018a), nodal chains (Chen *et al.*, 2021b), and nodal net (Liu *et al.*, 2021c). Phononic topological nodal lines exist ubiquitously in centrosymmetric solids (Liu *et al.*, 2022).

Straight nodal lines along high-symmetry lines (HSLs) with C_n rotational symmetry can be categorized into two fundamental types based on their transverse dispersion: linear and quadratic types (Liu *et al.*, 2021c, 2022; Qin *et al.*, 2024). This classification applies particularly to systems with threefold rotational symmetry ($n = 3$), where the low-energy effective Hamiltonian takes the general form:

$$H = \begin{pmatrix} 0 & Ak_- + Bk_+^2 \\ A^*k_+ + B^*k_-^2 & 0 \end{pmatrix} \quad (76)$$

where $k_{\pm} = k_1 \pm ik_2$ with k_1 and k_2 being the wave vector perpendicular to the rotational axis. A and B are complex constants that do not depend on k_1 and k_2 . The location of nodal line is determined by $Ak_- + Bk_+^2 = 0$ which give rise to 4 nodal lines: One located at the rotation axis along k_3 with Berry phase $+\pi$, while the other three located at generic positions which are related by C_3 rotation and have Berry phase

$-\pi$, *i.e.*,

$$\begin{aligned} (0, 0, k_3) : & \text{Berry phase } +\pi \\ \left(k_0 \cos \frac{\theta_0}{3}, k_0 \sin \frac{\theta_0}{3}, k_3\right) : & \text{Berry phase } -\pi \\ \left(k_0 \cos \frac{\theta_0 + 2\pi}{3}, k_0 \sin \frac{\theta_0 + 2\pi}{3}, k_3\right) : & \text{Berry phase } -\pi \\ \left(k_0 \cos \frac{\theta_0 - 2\pi}{3}, k_0 \sin \frac{\theta_0 - 2\pi}{3}, k_3\right) : & \text{Berry phase } -\pi \end{aligned} \quad (77)$$

where $k_0 = |-\frac{A}{B}|$ and $\theta_0 = \arg(-\frac{A}{B})$. Nodal lines can be classified into two fundamental types based on their transverse dispersion: (i) linear nodal lines with π Berry phase (topologically nontrivial) and (ii) quadratic nodal lines with 2π Berry phase (Liu *et al.*, 2022; Qin *et al.*, 2024). The topological character is determined by the dominant term in the effective Hamiltonian: when the linear term dominates ($|A/B| \gg 1$), the system exhibits a π Berry phase, whereas dominance of the quadratic term ($|A/B| \ll 1$) yields a -2π Berry phase. For systems with C_4 or C_6 symmetry, the linear term in Eq. (76) vanishes, allowing only a single straight nodal line along the rotational axis. In these cases, quadratic nodal lines emerge with Berry phase $\pm 2\pi$, corresponding to a winding number $n_W = \pm 2$ (Liu *et al.*, 2022). This distinct topological signature arises from the doubled winding of the pseudospin texture around the nodal line.

C. Obstructed Atomic Insulator-like Topological Phonons

Topological phonons can be defined not only in gapless systems but also in gapped systems under specific symmetry conditions, as classified by the “ten-fold way” table in Fig. 4 and discussed in Sec. III.C. Unlike conventional topological gapped states, typically arising from band inversions in phonon spectra, a distinct class termed “obstructed atomic insulator-like phonon modes” exists in gapped systems. These modes exhibit a mismatch between the atomic center and the vibrational center of phonon modes, leading to localized vibrations at boundaries. In this section, we review recent progress on obstructed phonon modes, with emphasis on the prototypical material tellurium (Te), where such modes have been experimentally observed.

Phonons represent quantized collective vibrations of atomic lattices, where each mode corresponds to a distinct pattern of atomic displacements. However, certain phonon modes exhibit unconventional origins: they may arise from vibrations localized at empty atomic sites or involve non-atomic orbital symmetries (e.g., non- p -orbital-like vibrations), as illustrated in Figs. 29 (a)–(b). These anomalous modes, termed obstructed phonon modes (Ma *et al.*, 2023; Xu *et al.*, 2024b; Zhang *et al.*, 2023a,b), defy conventional descriptions of lattice dynamics. The unconventional nature of these modes can be identified through either real-space invariants or open-boundary calculations (Zhang *et al.*, 2023a,b). The former

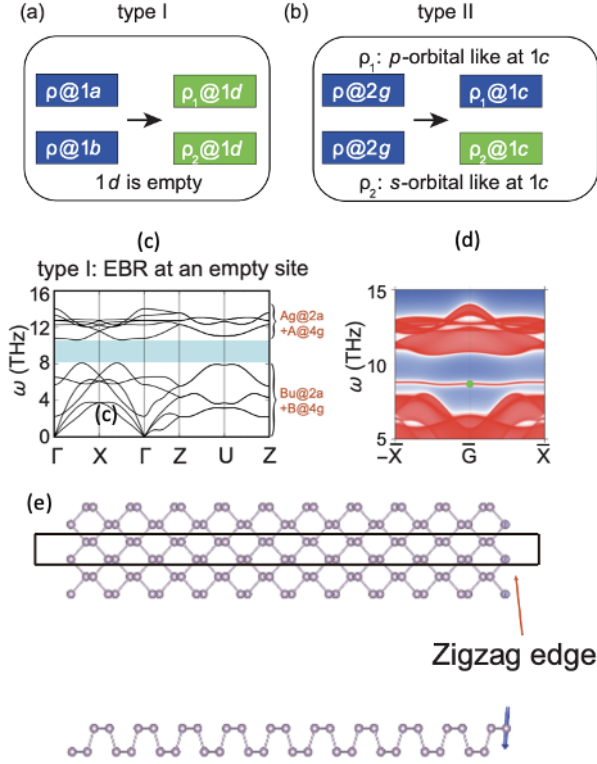


Figure 29 Two types of unconventionality. Atomic vibrations act as p orbitals. (a) Phonon modes contributed by the vibration center at an empty site. (b) Phonon modes contributed by the vibration center at an atom site, yet show a non-atomic vibration orbitals (non- p orbital symmetry). (c) Phonon spectra of the monolayer black phosphorus. (d) Phonon spectra for the monolayer black phosphorus with an open boundary condition, where there are floating obstructed surface phonon modes ~ 9 THz. The real space vibration for the surface phonon mode marked by the green hexagon is shown in (e). Adapted from Ref. (Zhang *et al.*, 2023a).

one quantifies the mismatch between atomic positions and vibrational centers, while the latter one reveals localized surface modes (“floating states”) detached from bulk phonon spectra. Such modes typically emerge from dangling-bond vibrations on crystal surfaces and are intimately linked to the material’s symmetry and electronic structure. Their spectral isolation and spatial localization make them promising for controlling phonon-mediated phenomena at interfaces or defects.

As a concrete example, Figs. 29 (c) and (d) display the phonon spectra of monolayer black phosphorus under periodic and open boundary conditions, respectively (Zhang *et al.*, 2023a). Notably, the open-boundary spectrum reveals floating obstructed surface phonon modes near 9 THz, which are absent in the periodic calculation. The real-space vibrational pattern of one such surface mode (indicated by the green hexagon in Fig. 29 (d)) is shown in Fig. 29 (e), clearly demonstrating its localized character at the edge.

Figure 30 (a) shows the phonon spectra of tellurium under open boundary conditions. The black solid lines near ~ 100 cm^{-1} correspond to obstructed surface phonons, arising from

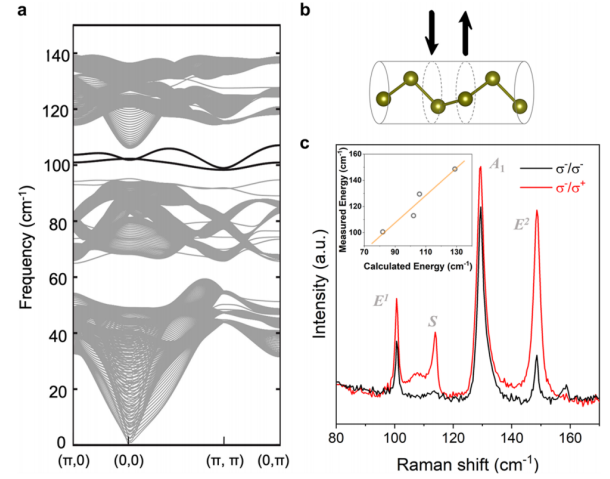


Figure 30 (a) First-principles calculations of right-handed tellurium (Te) with open-boundary conditions along [010] direction. The black solid lines ~ 100 cm^{-1} correspond to obstructed atomic-insulator-like phonon modes, arising from dangling-bond vibrations at the surface. (b) Experimental configuration for circularly polarized Raman spectroscopy in backscattering geometry. (c) Raman spectrum of Te showing an additional surface (S) mode. The inset displays the fitting results, confirming the S-mode’s origin from surface dangling-bond vibrations. Adapted from Ref. (Zhang *et al.*, 2023b).

dangling bonds on the [010] surface. Although the symmetry data (irreducible representations at high-symmetry momenta) of the lowest six phonon bands match those of an “atomic insulator”, these modes originate from empty atomic positions, classifying Te as an obstructed phonon material. The obstructed surface phonons persist across the entire surface Brillouin zone and lie within the bulk phonon gap, making them detectable via helicity-resolved Raman scattering.

Figure 30 (c) presents the Raman shifts of Te under circularly polarized incident/scattered light. In addition to the three Raman-active modes (E^1 , E^2 , and A_1), an extra S mode appears. The frequencies of all four modes align well with first-principles calculations (inset), confirming the S mode as the obstructed surface phonon (Zhang *et al.*, 2023b).

D. Topological Phonon Materials Database

The method of symmetry-based indicator theory and topological quantum chemistry (TQC) (Bradlyn *et al.*, 2017; Elcoro *et al.*, 2021; Po *et al.*, 2017) provides a powerful framework for identifying topological materials. Its classification hinges on the elementary band representations (EBRs) (Cano and Bradlyn, 2021; Michel and Zak, 2001), which distinguish topologically trivial and nontrivial phases: A band structure adiabatically connected to an “atomic insulator” is trivial, whereas the absence of such a connection typically signals nontrivial topology (Cano and Bradlyn, 2021). This classification is rigorously formalized using symmetry-based indicators (Po *et al.*, 2017; Song *et al.*, 2018; Tang *et al.*, 2019b,c,d; Tang and Wan, 2024; Vergniory *et al.*, 2019a; Zhang *et al.*,

2019a).

To date, extensive high-throughput searches for topological materials, encompassing both electronic and phononic systems, have been conducted using first-principles methods (Chen *et al.*, 2021a; Li *et al.*, 2021c; Tang *et al.*, 2019b; Vergniory *et al.*, 2019a; Xu *et al.*, 2020, 2024a; Zhang *et al.*, 2019a). From the symmetry perspective, phonons behave analogously to spinless electrons, with their three vibrational degrees of freedom resembling $p_{x,y,z}$ orbitals (Liu *et al.*, 2018). Consequently, the complete classification of topological phononic materials can be achieved within the framework of single-valued representations of the 230 space groups. Pioneering this effort, (Li *et al.*, 2021c) performed a high-throughput screening of topological phononic materials, identifying systems hosting phononic nodal lines and Weyl points, as shown in Fig. 31 (a). By computing phononic band structures along high-symmetry paths, they systematically classified materials with these topological features. More recently, (Xu *et al.*, 2024a) expanded this approach by screening phononic obstructed atomic bands using topological quantum chemistry, paving the way for further experimental studies, as shown in Fig. 31 (b).

V. FROM TOPOLOGICAL PHONONS TO CHIRAL PHONONS

“Chirality”¹ in phonons is multifaceted and can be interpreted diversely across various disciplines. For example, it can be defined by the Chern number in the field of topological band theory, and in this case, chiral phonons are the Weyl phonons with nonzero Chern number, which have been identified through various experimental observations (Jin *et al.*, 2022; Li *et al.*, 2021a; Miao *et al.*, 2018; Zhang *et al.*, 2023b, 2018a, 2020b, 2019b). In another example, angular momentum (AM, $l_{\nu q}$) is introduced to describe the chiral atomic motions in the real space (Hamada *et al.*, 2018; Hamada and Murakami, 2020b; McLellan, 1988; Ueda *et al.*, 2023; Zhang and Niu, 2014; Zhang *et al.*, 2024b), and the ones with nonzero AM was also referred to as chiral phonons, or circularly polarized phonons. The sign of AM also reflects the chirality of phonons, but this definition is convention-dependent because AM is a pseudo-vector. To address this issue, an alternative definition of chiral phonons based on helicity has been introduced, as discussed in (Zhang *et al.*, 2025a). Phonon helicity is a pseudo-scalar, making it convention-independent under SO(3) operations. The sign of the helicity directly indicates

the chirality of circularly polarized phonons, providing a more robust and unambiguous characterization of their chiral nature. The relationship between helicity and angular momentum $l_{\nu q}$ is illustrated in Fig. 32, where ν indicates the phonon mode and q is the momentum. Figure 32 shows that chiral phonons defined by the helicity can be nonchiral, even in the cases where the AM is nonzero.

According to topological band theory, the Chern number is related to the eigenvalue of (screw) rotational symmetry C_n , which is also known as pseudo-angular momentum (PAM) (Fang *et al.*, 2012; Tsirkin *et al.*, 2017; Yao *et al.*, 2008; Zhang and Niu, 2015; Zhang and Murakami, 2022). That is, PAM can diagnose topological phonons. Recently, PAM also has been widely used to identify chiral phonons (Ishito *et al.*, 2023c; Zhang *et al.*, 2023b; Zhu *et al.*, 2018). However, (Zhang *et al.*, 2025a) highlights that there is no intrinsic connection between PAM and AM unless symmetry analysis and first-principles calculations are incorporated as supplementary tools. For instance, (Zhang *et al.*, 2023b) demonstrates that Weyl phonons and chiral phonons defined by AM/helicity are connected (Li *et al.*, 2021a; Zhang *et al.*, 2023b, 2020b), but this connection relies on a combination of topological band theory, symmetry analysis, and first-principles calculations (Zhang *et al.*, 2025b).

In this section, we will review several new fundamental concepts related to the chirality of circularly polarized phonons, including their relationships and corresponding experimental benchmarks illustrated with material examples. Additionally, we will review chiral phonon-driven physical phenomena and explore their potential applications in various fields.

A. Basic Concepts Related to Chiral Phonons

1. Phonon Angular Momentum

Under the harmonic approximation, a phonon mode $\epsilon_{\nu q}$, which describes a specific collective motion of ions, is an eigenvector of the mass-weighted dynamic matrix. Mathematically, this can be expressed as:

$$\sum_{\beta \kappa'} D_{\kappa \kappa'}^{\alpha \beta}(\mathbf{q}) \epsilon_{\nu \mathbf{q}}^{\beta \kappa'} = \omega_{\nu \mathbf{q}}^2 \epsilon_{\nu \mathbf{q}}^{\alpha \kappa}, \quad (78)$$

with the mass-weighted dynamic matrix to be:

$$D_{\kappa \kappa'}^{\alpha \beta}(\mathbf{q}) = \sum_{l'} \frac{\Phi_{\alpha \beta}(0\kappa, l'\kappa')}{\sqrt{m_\kappa m_{\kappa'}}} e^{i\mathbf{q}[\mathbf{r}(l'\kappa') - \mathbf{r}(0\kappa)]}, \quad (79)$$

where $\epsilon_{\nu \mathbf{q}}^{\alpha \kappa}$ is the α -th ($\alpha \in \{x, y, z\}$) component of the ν -th eigenvector for the dynamic matrix at momentum \mathbf{q} , m_κ is the mass of the κ -th atom in the primitive unit cell, and $\mathbf{r}(l\kappa) = \mathbf{R}_l + \boldsymbol{\tau}_\kappa$ represents the equilibrium position of the κ -th atom in the l -th primitive unit cell \mathbf{R}_l . The eigenvectors $\epsilon_{\nu \mathbf{q}}$ serve as the unitary transformation for the Bloch summation

¹ In some references, e.g. (Barron, 2021), the concept of chirality is classified into two categories: the true chirality and false chirality. The true chirality refers to the existence of two enantiomer states that are interchanged only by spatial inversion operation \mathcal{P} but NOT by time-reversal operation \mathcal{T} ; however, for the false chirality, the two enantiomer states are interchanged by both \mathcal{P} and \mathcal{T} . The distinction between true and false chirality is essential to the problem of homochirality origin of our natural world including DNA. The homochiral phenomenon must have a true chiral origin.

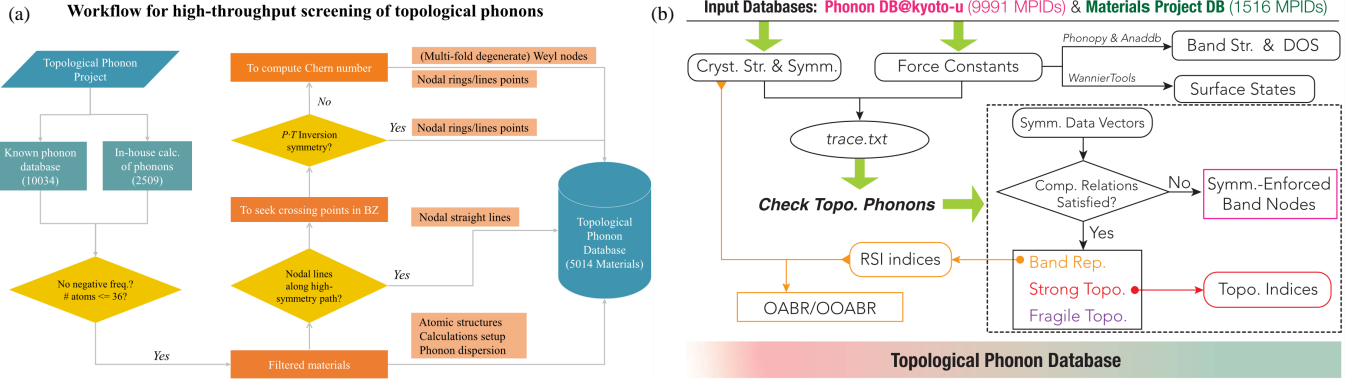


Figure 31 Construction of database for topological phononic materials. (a) High-throughput computational screening of topological phononic nodal lines/rings/points. Adapted from Ref. (Li *et al.*, 2021c). (b) Topological phonon database for obstructed atomic band representations (OABRs) and orbital-selected OABRs (OOABR). Adapted from Ref. (Xu *et al.*, 2024a).

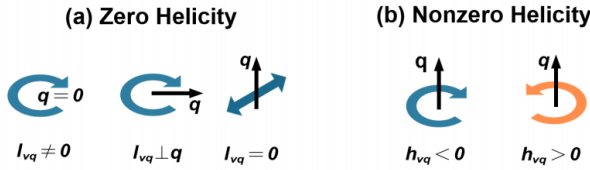


Figure 32 The previous definition of chiral phonons based on angular momentum is convention-dependent and not well-defined, as angular momentum is a pseudo-vector. To address this issue, an alternative definition based on phonon helicity is proposed (Zhang *et al.*, 2025a). Phonon helicity is a pseudo-scalar and thus convention-independent and well-defined. The relationships between angular momentum, helicity, and representative atomic motions are illustrated as follows: (a) Phonon modes with zero helicity can exhibit three possibilities. The first two cases represent nonchiral phonons under the helicity-based definition, whereas they would be classified as chiral phonons under the angular momentum-based definition. (b) Phonon modes with nonzero helicity must have nonzero angular momentum, and the sign of the helicity directly indicates the chirality of the circularly polarized phonon modes. Adapted from Ref. (Zhang *et al.*, 2025a).

of the atomic displacements away from their equilibrium positions. Consequently, the phonon mode $\mathbf{u}_{\nu q}$ can be explicitly expressed in the Bloch summation form as:

$$\mathbf{u}_{\nu q}(\mathbf{l}\kappa) = \epsilon_{\nu q}^{\kappa} e^{i\mathbf{q} \cdot (\mathbf{R}_l + \boldsymbol{\tau}_{\kappa})}, \quad (80)$$

where $\mathbf{u}_{\alpha}(\mathbf{R}_l, \boldsymbol{\tau}_{\kappa})$ represents the displacement of the κ -th atom in the l -th unit cell along α direction. With this, one can define phonon AM, i.e., $l_{\alpha, \nu q}$, for a specific phonon mode $\epsilon_{\nu q}$ at momentum \mathbf{q} in the equilibrium state as (Kishine *et al.*, 2020; McLellan, 1988; Zhang and Niu, 2014; Zhang *et al.*, 2025a):

$$\begin{aligned} l_{\alpha, \nu q} &= \hbar \epsilon_{\nu q}^{\dagger} M_{\alpha} \epsilon_{\nu q} \\ &= \sum_{\kappa}^N l_{\alpha, \nu q}^{\kappa} = \sum_{\kappa}^N \hbar \epsilon_{\nu q}^{\kappa \dagger} \mathfrak{M}_{\alpha} \epsilon_{\nu q}^{\kappa}, \end{aligned} \quad (81)$$

where $M_{\alpha} = \oplus_{\kappa=1}^N \mathfrak{M}_{\alpha}$, $\alpha, \beta, \gamma \in \{x, y, z\}$, $\mathfrak{M}_{\alpha(\beta\gamma)} = (-i)\epsilon_{\alpha(\beta\gamma)}$ forms the Lie algebra of the $O(3)$ group.

From a semi-classical perspective, $l_{\nu q}$ can be interpreted as the summation of the circular polarization of atoms in the primitive unit cell. Consequently, a phonon mode with $l_{\alpha, \nu q} \neq 0$ corresponds to atomic motions where the net circular polarization of all atoms in the unit cell is nonzero. The total AM of the system, denoted as J^{ph} , is defined as the ensemble average of the AM of each phonon mode across the entire Brillouin zone. Mathematically, this can be expressed as: $J^{\text{ph}} = \sum_{\alpha, \nu, \mathbf{q}} \langle l_{\alpha, \nu \mathbf{q}} \rangle$, where $\langle l_{\alpha, \nu \mathbf{q}} \rangle$ represents the average angular momentum of the phonon mode ν at momentum \mathbf{q} . This framework provides a comprehensive understanding of the phonon Edelstein effect and phonon angular momentum in crystalline materials (Hamada *et al.*, 2018; Hamada and Murakami, 2020b; Xu *et al.*, 2018; Zhang *et al.*, 2024a).

2. Phonon Helicity

Figure 32 (a1) illustrates phonon modes with nonzero AM, where at least one atom exhibits circular motion. When all atoms rotate circularly, different atoms can have varying circular polarizations, including opposite signs. In the cases where $l_{\alpha, \nu q} = 0$, three possible scenarios arise: (1) atoms undergo linear vibrations, (2) atoms remain static, or (3) two sublattices rotate in opposite directions.

Previously, chiral phonons (circularly polarized phonons), were referred to as phonon modes with nonzero AM and were extensively studied in 2D systems. However, chirality inherently requires three degrees of freedom: two for circular motion and one for the propagation direction. Additionally, AM is a pseudovector, making its definition convention-dependent under $SO(3)$ operations. For example, the algebraic sign of the AM undergoes inversion when adopting left-handed versus right-handed coordinate system conventions. This limitation underscores the need for a more robust and convention-independent definition of chiral phonons, such as one based on phonon helicity (Zhang *et al.*, 2025a).

Phonon helicity describes the chirality of the phonon mode $\epsilon_{\nu\mathbf{q}}$, as shown in Fig. 32, in terms of phonon AM ($\mathbf{l}_{\nu\mathbf{q}}$) and the propagation direction \mathbf{q} :

$$\mathbf{h}_{\nu\mathbf{q}} = \mathbf{q} \cdot \mathbf{l}_{\nu\mathbf{q}}. \quad (82)$$

For phonon modes with zero helicity, the phonon AM can either be perpendicular to \mathbf{q} or zero, as illustrated in Fig. 32 (a). Consequently, phonon modes defined as chiral based on nonzero AM can be achiral under the definition of phonon helicity. This ambiguity highlights that chiral phonons are not well-defined in purely 2D systems, as the propagation direction will always be perpendicular to the AM. In previous studies, to address the lack of a third degree of freedom in 2D systems, the z + direction was often assumed as the propagation direction to define the chirality of phonons. In 3D systems, however, chiral phonons are well-defined as phonon modes with nonzero helicity, where the phonon AM is not perpendicular to \mathbf{q} . Thus, chiral phonons are characterized by nonzero helicity, which inherently implies nonzero AM, and the sign of the helicity reflects the chirality of the circularly polarized phonons, as shown in Fig. 32 (b). This definition provides a more robust and convention-independent framework for identifying and studying chiral phonons in 3D systems, and it is also closely related to the chiral charge density waves (Luo and Dai, 2023; Romao and Juraschek, 2024; Yang *et al.*, 2024a; Zhang *et al.*, 2024b).

3. Phonon Pseudo-angular Momentum

Because neither the phonon AM nor the helicity is easily observable in experiments, the pseudo-angular momentum (PAM) is introduced as a practical benchmark for identifying chiral phonons (Bourgeois *et al.*, 2025; Ishito *et al.*, 2023a,b; Komiyama *et al.*, 2022; Yao *et al.*, 2008; Zhang and Niu, 2015; Zhang *et al.*, 2025a, 2023b; Zhang and Murakami, 2022; Zhang *et al.*, 2025b; Zhu *et al.*, 2018). For a phonon mode $u_{\kappa\alpha,\mathbf{q}}$ at momentum \mathbf{q} with little group \mathcal{C}_n , the representation matrix of \mathcal{C}_n can be derived as follows:

$$\begin{aligned} \mathcal{C}_n u_{\kappa\alpha,\mathbf{q}} &= \mathcal{C}_n \sum_{\mathbf{l}} e^{i\mathbf{q} \cdot (\mathbf{R}_{\mathbf{l}} + \boldsymbol{\tau}_{\kappa})} u_{\kappa\alpha}(\mathbf{R}_{\mathbf{l}} + \boldsymbol{\tau}_{\kappa}) \\ &= \sum_{\mathbf{l}'} e^{i\mathcal{C}_n \mathbf{q} \cdot (\mathbf{R}_{\mathbf{l}'} + \boldsymbol{\tau}_{\kappa'})} \times \\ &\quad \sum_{\beta} \mathcal{C}_{n,\alpha\beta} u_{\kappa'\beta}(\mathbf{R}_{\mathbf{l}'} + \boldsymbol{\tau}_{\kappa'}) \\ &= e^{i\mathbf{G} \cdot \boldsymbol{\tau}_{\kappa'}} P_{\kappa'\kappa} \sum_{\beta} \mathcal{C}_{n,\alpha\beta} u_{\kappa'\beta,\mathbf{q}}, \end{aligned} \quad (83)$$

The inner product between $u_{\kappa'\beta,\mathbf{q}}$ and $\mathcal{C}_n u_{\kappa\alpha,\mathbf{q}}$ yields the representation matrix for the rotational symmetry \mathcal{C}_n . Mathematically, this can be expressed as:

$$D(\mathcal{C}_n)_{\kappa'\beta,\kappa\alpha} = e^{i\mathbf{G} \cdot \boldsymbol{\tau}_{\kappa'}} P_{\kappa'\kappa} \mathcal{C}_{n,\alpha\beta}. \quad (84)$$

$P_{\kappa'\kappa}$ is a permutation matrix describing the transformation between the sublattice κ and κ' . $\mathbf{G} = \sum_{i=1}^3 n_i \mathbf{b}_i$, where \mathbf{b}_i is the

reciprocal lattice vector and n_i is an integer. The matrix $P_{\kappa'\kappa}$ is a permutation matrix that describes the transformation between the sublattices κ and κ' under the symmetry operation. Meanwhile, \mathbf{G} is a reciprocal lattice vector defined as:

$$\mathbf{G} = \sum_{i=1}^3 n_i \mathbf{b}_i,$$

where \mathbf{b}_i are the reciprocal lattice vectors and n_i are integers. The phonon mode $u_{\nu\mathbf{q}}$ is constructed as a linear combination of the atomic displacement components $u_{\kappa\alpha,\nu\mathbf{q}}$, and it must be an eigenvector of the rotational symmetry operator \mathcal{C}_n . Mathematically, this can be expressed as:

$$D(\mathcal{C}_n) u_{\nu\mathbf{q}} = e^{-i2\pi l_{ph}/n} u_{\nu\mathbf{q}}. \quad (85)$$

The pseudo-angular momentum (PAM) l_{ph} reflects the eigenvalue $e^{-i2\pi l_{ph}/n}$ of the representation matrix $D(\mathcal{C}_n)$ for the rotational symmetry \mathcal{C}_n , thus l_{ph} can take arbitrary integer values (modulo n).

In systems with screw rotational symmetry $\mathcal{C}_{n,\tau_{m/n}} = \mathcal{C}_n T_{\tau_{m/n}}$, where $\tau_{m/n}$ is the m/n fractional translation vector along the rotational axis and $T_{\tau_{m/n}}$ is the translation operator, the representation matrix for the screw rotation is modified to account for the fractional translation. Specifically, the representation matrix becomes $D(\mathcal{C}_{n,\tau_{m/n}}) = e^{-i\mathbf{q} \cdot \boldsymbol{\tau}_{m/n}} \cdot D(\mathcal{C}_n)$. Thus we have:

$$\begin{aligned} D(\mathcal{C}_{n,\tau_{m/n}}) u_{\nu\mathbf{q}} &= \mathcal{C}_n T_{\tau_{m/n}} u_{\nu\mathbf{q}} \\ &= e^{-i2\pi \frac{l_{rot}}{n} - i\mathbf{q} \cdot \boldsymbol{\tau}_{m/n}} u_{\nu\mathbf{q}}. \end{aligned} \quad (86)$$

In this case, PAM is expressed as:

$$l_{ph} = l_{rot} + \frac{\mathbf{q} \cdot \boldsymbol{\tau}_{m/n}}{2\pi/n}.$$

l_{rot} represents the pure rotational part of the PAM, corresponding to the eigenvalue of the rotational symmetry \mathcal{C}_n . $l_{\tau} = \frac{\mathbf{q} \cdot \boldsymbol{\tau}_{m/n}}{2\pi/n}$ accounts for the contribution from the fractional translation $\boldsymbol{\tau}_{m/n}$ along the rotational axis. This decomposition reveals that the PAM l_{ph} becomes \mathbf{q} -dependent in systems with screw rotational symmetries $\mathcal{C}_{n,\tau_{m/n}}$. As a result, l_{ph} can take non-integer values, in contrast to systems with pure rotational symmetries where it is quantized to integers modulo n (Zhang *et al.*, 2025a; Zhang and Murakami, 2022).

B. Angular Momentum *v.s.* Pseudo-angular Momentum

Previous studies have used PAM as a benchmark for circularly polarized phonons defined by AM, suggesting an intrinsic relationship between these two. However, PAM has no intrinsic connection to either phonon angular momentum

or phonon helicity, meaning it cannot serve as an experimental benchmark for observing chiral phonons. Nevertheless, in certain cases, PAM can be used for identifying nonzero AM, combined with symmetry analysis, first-principles calculations, etc., as shown in (Bourgeois *et al.*, 2025; Che *et al.*, 2024; Ishito *et al.*, 2023a,b; Yang *et al.*, 2024b; Zhang *et al.*, 2025a, 2023b, 2025b; Zhu *et al.*, 2018). (Zhang *et al.*, 2025a) provides a comprehensive explanation of the distinction between PAM and AM from a definitional perspective. The rotation operator in the $O(3)$ group with an arbitrary angle ϕ along the α -th direction can be expressed as:

$$R(\alpha, \phi) = e^{-i\mathcal{M}_\alpha \phi}, \quad (87)$$

Since phonon AM is the expectation value of \mathcal{M}_α , it can be defined in any system, regardless of its symmetry. The definition in Eq. (81) demonstrates that AM solely encapsulates information about the phonon polarization and atomic motion within the primitive cell. It is independent of the relative phases between different atoms, reflecting the local property of the phonon mode, as discussed in (Zhang *et al.*, 2025a).

Meanwhile, pseudo-angular momentum (PAM) reflects the eigenvalue of $\mathcal{C}_{n, \tau_{m/n}}$ operator, making it both an observable and a conserved physical quantity during phonon-related scattering processes in systems invariant under $\mathcal{C}_{n, \tau_{m/n}}$. When considering systems with translation symmetry, only discrete rotational symmetries $\mathcal{C}_{n, \tau_{m/n}}$ appear in crystals, where $n \in \{2, 3, 4, 6\}$. Consequently, the rotational operator is expressed as:

$$\mathcal{C}_n = e^{-i\mathcal{M}_\alpha 2\pi/n}. \quad (88)$$

Phonon PAM is defined by the eigenvalue of \mathcal{C}_n , as shown in Eq. (85), and thus can only be defined at \mathcal{C}_n -invariant momenta. Furthermore, PAM encodes information about the relative phase between \mathcal{C}_n -related atoms, potentially extending across multiple primitive cells. From this perspective, PAM can be regarded as a global property of a specific phonon mode (Zhang *et al.*, 2025a).

In conclusion, phonon AM can be defined in any systems and reflects the local properties of a phonon mode. In contrast, PAM is defined only at (screw) rotation-invariant \mathbf{q} points, as it reflects the eigenvalues of \mathcal{C}_n , revealing global information about the phonon mode. There is no intrinsic one-to-one relationship between AM and PAM. Therefore, to observe chiral phonons by detecting PAM, first-principles calculations and symmetry analysis are essential, as demonstrated in studies on Te (Zhang *et al.*, 2023b) and α -HgS (Ishito *et al.*, 2023b). The selection rules for circularly polarized Raman scattering in systems with rotational symmetries are illustrated in Fig. 35.

C. Connections between Topological Phonon & Chiral Phonon

In this subsection, we will explore the intricate relationship and distinct characteristics of topological phonons and specifically defined chiral phonons, i.e., circularly polarized phonons defined by AM, as illustrated in Fig. 33. Our focus will be on Weyl phonons, which exhibit both topological and chiral properties, and we will provide a detailed analysis of their features from the definition point of view.

1. Weyl Phonons are Both Topological and Chiral

Topological phonons are defined and classified by their topological invariants, leading to a rich variety of categories, including Weyl phonons, Dirac phonons, and nodal-line phonons, among others. Each classification is associated with distinct topological surface states and bulk properties, as governed by the principle of “bulk-surface correspondence.” Weyl phonons, in particular, represent a unique class of quasiparticles that are both topological and chiral. They are characterized by a topological invariant, namely the Chern number. When the Chern number is nonzero, the phonon mode is topological, exhibiting helicoid surface states and unique pseudospin textures around the Weyl phonon degeneracy, as shown in Sec. IV.A.

The left panels of Fig. 33 illustrate an example of a twofold-degenerate quadruple Weyl phonon in the material BaPtGe (Li *et al.*, 2021a; Zhang *et al.*, 2025b, 2020b). This phonon mode features four parallel helicoid surface states due to its Chern number of 4, showcasing the interplay between topology and chirality in such systems.

The right panels show previous definitions of chiral phonons relied on the concept of nonzero AM, which has been shown to be insufficiently well-defined. A more rigorous definition based on phonon helicity is proposed, which is a pseudoscalar and thus convention-independent and well-defined. When the helicity of a phonon mode is nonzero, it exhibits circular vibrations in real space, providing a clear and unambiguous signature of chirality. The right panels also illustrate an example of the twofold-degenerate quadruple Weyl phonon in the material BaPtGe, which exhibits nonzero helicity and circular atomic motions for the phonon mode with a Chern number of 4. This example highlights the connection between topological properties and chiral behavior in phononic systems.

2. Diagnosing Weyl Phonons by Pseudo-angular Momentum

Topological classifications for Weyl quasiparticles with (screw) rotational symmetry \mathcal{C}_n have been established (Fang *et al.*, 2012; Tsirkin *et al.*, 2017; Zhang *et al.*, 2025a). The monopole charge of a Weyl phonon on high-symmetry lines or at high-symmetry points depends on the symmetry of the

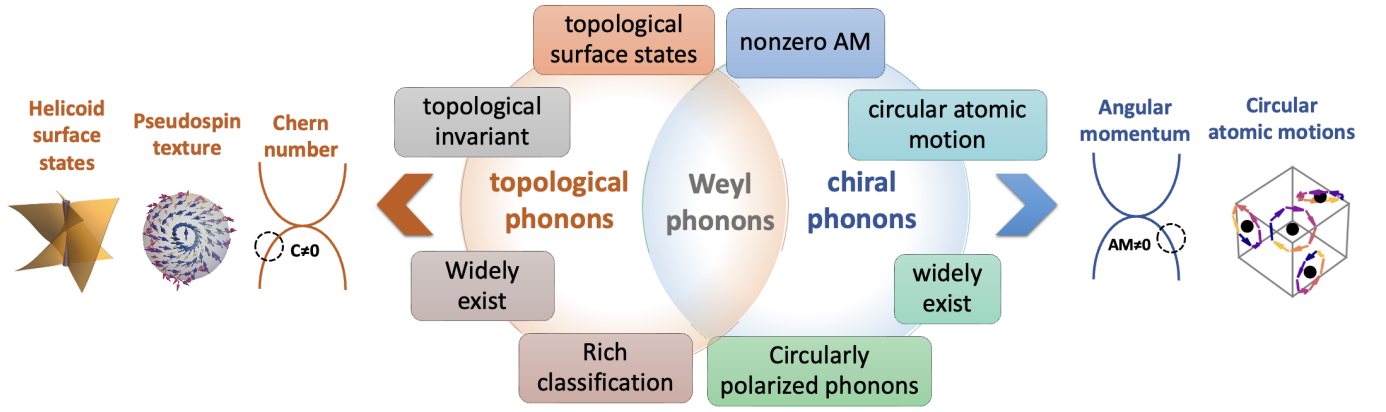


Figure 33 The connection and differences between topological phonons and specifically defined chiral phonons (circularly polarized phonons defined by AM) can be summarized as follows: Weyl phonons are both topological and chiral. Topological phonons are characterized by topological invariants, leading to rich classifications based on the type of invariant, such as Weyl phonons, Dirac phonons, and nodal-line phonons. When the topological invariant is nonzero, the phonon mode is topological, exhibiting features like topological surface states (“bulk-surface correspondence”) and unique pseudospin textures around the degeneracy points. Weyl phonons, for instance, are both topological and chiral, with a notable example being the twofold-degenerate quadruple Weyl phonon in BaPtGe. Chiral phonons, or the circularly polarized phonons, on the other hand, have been defined in various ways. Earlier studies defined them based on nonzero AM, but this definition is not well-defined. More recently, chiral phonons have been redefined using nonzero phonon helicity, which is a more robust and convention-independent criterion. When a phonon mode has nonzero helicity, atoms in real space exhibit circular vibrations, reflecting the chiral nature of the mode. Thus, while topological phonons are defined by their topological invariants, chiral phonons are defined by their helicity, with Weyl phonons serving as an example of modes that are both topological and chiral. Adapted from Ref. (Zhang *et al.*, 2025b).

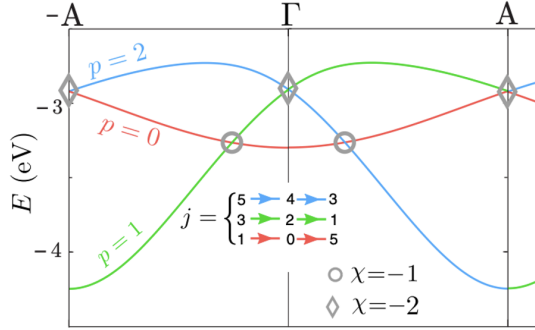


Figure 34 A group of band structures for a system along the $-A-\Gamma-A$ path, which preserves C_3 rotational symmetry. Here, p denotes the pseudo-angular momentum (PAM) value for each band, and χ represents the monopole charge of the Weyl phonons. It is important to note that the PAM for a specific phonon mode can be non-integer in systems with C_n screw rotational symmetry. Adapted from Ref. (Tsirkin *et al.*, 2017).

bands forming the Weyl phonon, specifically the PAM in C_n -invariant systems, as well as the little point group where the Weyl point is located (Zhang *et al.*, 2025a). Consequently, PAM can be used to diagnose Weyl phonons in C_n -invariant systems. In some previous studies, PAM has been used to identify chiral phonons defined by AM, as neither helicity nor AM is easily observable in experiments, yet there is no intrinsic relationship between PAM and AM (or helicity). (Zhang *et al.*, 2023b) pointed out that, in certain chiral systems, chiral phonons can be identified by detecting PAM in the circularly polarized Raman scattering, since Weyl phonons are

chiral phonons in such systems.

Figure 34 provides an example in C_3 -invariant systems, where p represents the pure rotation part of PAM and χ denotes the Chern number (monopole charge) (Tsirkin *et al.*, 2017). The Weyl phonons at both Γ and A , which are time-reversal invariant momenta, are double Weyl phonons with a monopole charge of -2 , while those along the $\Gamma-A$ path are conventional Weyl phonons with a monopole charge of -1 . Thus, relationship between PAM and the Chern number for Weyl phonons can be established, providing a systematic framework for detecting chiral phonons in the circularly polarized Raman scattering process. Moreover, the selection rules for circularly polarized Raman scattering in systems with rotational symmetries C_n are illustrated in Fig. 35.

Experimental observations of chiral phonons in C_3 screw rotation systems have been demonstrated in both Te (Zhang *et al.*, 2023b) and α -HgS (Ishito *et al.*, 2023b), supported by first-principles calculations and symmetry analysis. These studies provide concrete evidence of chiral phonons in materials with rotational symmetry, highlighting the interplay between symmetry, topology, and phonon circular polarization. In the next subsection, we will use Te as an example to demonstrate that Weyl phonons are chiral phonons and explore how to observe such phonons using PAM.

3. Weyl Phonons are Typical Chiral Phonons: Te As an Example

Chiral crystals such as Te exist in two enantiomeric structures, as illustrated in Figs. 36 (a1) and (b1). These enan-

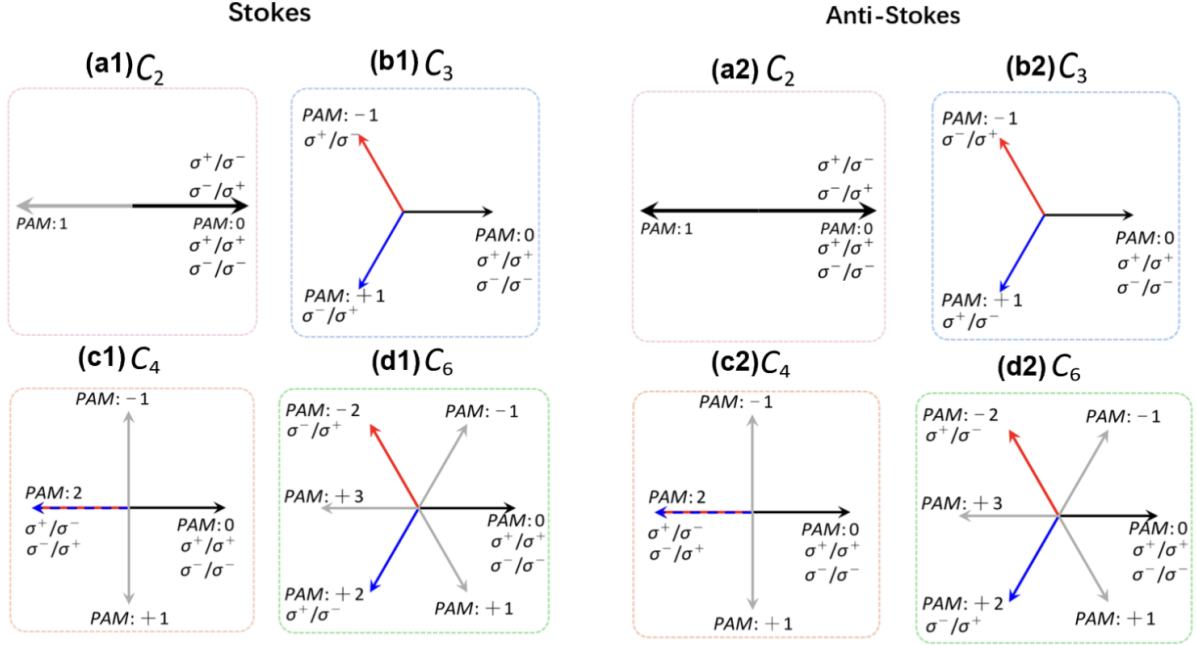


Figure 35 The selection rules for circularly polarized Raman scattering in the Stokes [(a1-d1)] and anti-Stokes [(a2-d2)] process for the systems with $C_n = 2, 3, 4, 6$ rotation symmetries, where the incident and scattered light propagate along the rotation axis. Each arrow represents the eigenvalue of a phonon mode in the complex plane, corresponding to its PAM value. In each figure, phonon modes marked by the black arrow are Raman active in both the σ^+/σ^+ and σ^-/σ^- processes, phonon modes marked by the blue (red) arrows are active in the σ^+/σ^- (σ^-/σ^+) process. These selection rules highlight the dependence of Raman activity on the PAM values and the circular polarization of the incident and scattered light. Adapted from Ref. (Zhang *et al.*, 2025a).

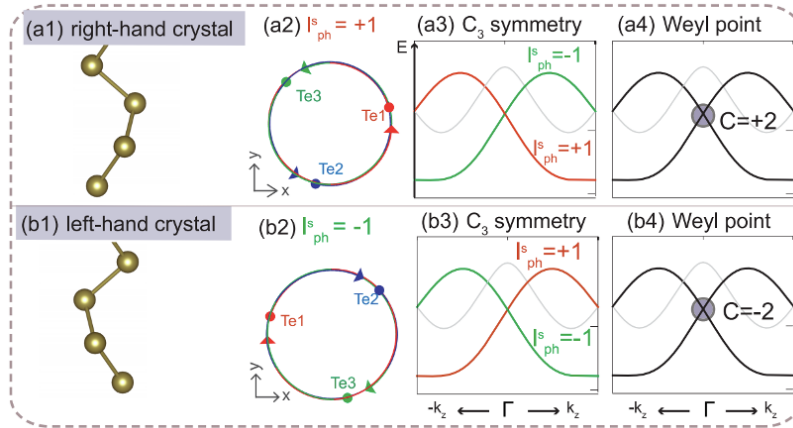


Figure 36 (a) and (b) are the different physical quantities for Te with the right-hand and left-hand structure, respectively. (a2) and (b2) shows the circular atomic motion for the same phonon modes but with different chiral crystal structures, showing opposite chiral motions in real space. (a3) and (b3) shows the pseudo-angular momentum for the same phonon modes with different chiral crystal structures. (a4) and (b4) shows the Chern number of the Weyl phonon in different chiral crystal structures. Thus, there is a close relationship between the chirality of crystal structure, the polarization of the atomic motion in the real space, the sign of pseudo-angular momentum, and the Chern number. Adapted from Ref. (Zhang *et al.*, 2025a).

tiomers exhibit threefold screw rotational symmetry along the atomic chain direction. Using the Weyl phonons in these two enantiomers as an example, we will demonstrate how to diagnose their topological and chiral properties through helicity-resolved Raman scattering, or circularly polarized Raman scattering. This approach will highlight the distinct character-

istics of Weyl phonons in chiral systems and their connection to both topology and chirality.

Figures 36 (a2) and (b2) depict the atomic motions for the lower branch of the Weyl phonon along the Γ -A direction in right- and left-handed crystals, respectively. Figures 36 (a3) and (b3) are the PAM, (a4) and (b4) are the Chern number of

the Weyl phonon in Te with right- and left-handed structures. If the chirality of the crystal structure changes, the circularly polarization (obtained from the atomic motion), the sign of PAM and the Chern number will also be altered. Therefore, the chirality of the crystal structure is intrinsically linked to the sign of the AM (and thus the helicity), the PAM, and the Chern number, demonstrating the profound connection between structural chirality and the topological and chiral properties of phonons (Bousquet *et al.*, 2024; Zhang *et al.*, 2025a, 2023b, 2025b).

The observation of topological phonons and chiral phonons will be reviewed in the next section.

VI. EXPERIMENTAL PROGRESSES OF TOPOLOGICAL AND CHIRAL PHONONS

While theoretical advances have significantly expanded the classification of topological phonons, parallel progress in understanding chiral phonons has also driven momentum in the field. In this section, we review selected experimental explorations to provide recent breakthroughs and challenges.

A. Topological Phonons

1. Topological Phonons Observed by IXS and INS

Soon after theoretical predictions of topological phonons in crystalline materials (Zhang *et al.*, 2018a), these states are experimentally observed by in FeSi (Miao *et al.*, 2018). As described in Section IV, FeSi has B-20 structure that breaks the inversion-symmetry. Its phonon excitations host spin-1 Weyl phonon at the Γ point and charge-2 Dirac phonon at the R point as shown in Fig. 23. These topological quasiparticles are experimentally determined using IXS. Figure 37 (a) shows the phonon dynamical structure factor of FeSi near the R point. The second derivative plot of Fig. 37 (a) is shown in Fig. 37 (b). Green and red curves are DFT calculated phonon band dispersion. The overall excellent agreement between DFT calculation and IXS spectra supports the effective low-energy model for charge-2 Dirac phonon at the R point (Zhang *et al.*, 2018a). A detailed fitting of the IXS curve shown in Figs. 37 (c)-(f) further confirm the degenerate point and Dirac-like phonon band dispersion near the R -point. Following the same experimental protocol, the \mathcal{PT} -symmetry protected phononic nodal lines were observed in MoB₂ (Zhang *et al.*, 2019b), where the IXS spectra have shown phonon band degenerate points that form an endless helical string along the L -direction.

For topological quasiparticles, including Weyl fermions (Lv *et al.*, 2015b; Murakami, 2007; Pal, 2011; Wan *et al.*, 2011; Weng *et al.*, 2015; Xu *et al.*, 2015), phonons (Ding *et al.*, 2022; Li *et al.*, 2021a, 2018; Liu *et al.*, 2019, 2020a, 2021e; Miao *et al.*, 2018; Xia *et al.*, 2019; Zhang *et al.*, 2023b, 2018a, 2020b), magnons (McClarty, 2022), and fractionalized excitations (Chen *et al.*, 2015; Ghaemi

et al., 2012; Levin and Stern, 2009, 2012; Maciejko and Fiete, 2015; Oshikawa and Senthil, 2006; Senthil and Fisher, 2001a,b; Seradjeh *et al.*, 2009; Shirley *et al.*, 2019; Song and Hermele, 2015; Stern, 2016; Sun and Mao, 2021; Vaezi, 2013; Wen, 1995), the topological invariants are defined on bulk wave functions. This has motivated experimental studies beyond the phonon band structure. As shown in Eq. (18), the phononic wave function enters $S(\mathbf{Q}, \omega)$ through the term $\mathbf{Q} \cdot \mathbf{e}_{\mathbf{q}\sigma}^i$. For a topological chiral wave function, the three components of $\mathbf{e}_{\mathbf{q}\sigma}^i$ are complex numbers with different phase factors, describing how atoms move out-of-phase with one another. Therefore, the chiral phonon wave function will result in a non-trivial interference of the real and imaginary component of $\mathbf{e}_{\mathbf{q}\sigma}^i$, which strongly modify the momentum dependent intensity distribution of $S(\mathbf{Q}, \omega)$. One can visualize this effect by calculating $S^{\text{DFT}}(\mathbf{Q}, \omega)$, $R(\mathbf{Q}, \omega)$ and $I(\mathbf{Q}, \omega)$ (Li *et al.*, 2021a). Here $R(\mathbf{Q}, \omega)$ and $I(\mathbf{Q}, \omega)$ consider only the real and imaginary part of $\mathbf{e}_{\mathbf{q}\sigma}^i$ in Eq. (18). The chiral phononic wave function can therefore be revealed by quantitatively comparing the experimental $S(\mathbf{Q}, \omega)$ and $S^{\text{DFT}}(\mathbf{Q}, \omega)$. This approach has been applied in the IXS study of BaPtGe that hosts twofold quadruple Weyl (TQW) phonons (see Fig.24) (Li *et al.*, 2021a). It has been shown that the wave functions near the twofold quadruple Weyl are primarily real along the $X_1 - \Gamma - X_2$ and $M_1 - \Gamma - M_2$ high-symmetry directions. In contrast, the phononic wave function along the $R_1 - \Gamma - R_2$ direction is mainly imaginary (Li *et al.*, 2021a).

To understand the direction-dependent wave function near the twofold quadruple Weyl point at Γ point, (Li *et al.*, 2021a) developed a simplified model that considers only four Pt atoms in the unit cell with locations $\mathbf{r}_{\text{Pt1}} = (c, c, c)$, $\mathbf{r}_{\text{Pt2}} = (-c + \frac{1}{2}, -c, c + \frac{1}{2})$, $\mathbf{r}_{\text{Pt3}} = (-c, c + \frac{1}{2}, -c + \frac{1}{2})$, $\mathbf{r}_{\text{Pt4}} = (c + \frac{1}{2}, -c + \frac{1}{2}, -c)$, where c is an arbitrary value satisfying $c \leq 1$. Based on the group theory, the atomic motions at the Γ point can be described as three non-degenerate basis states with irreducible representations of $\Gamma_1^{(1)}$, $\Gamma_2^{(1)}$, $\Gamma_3^{(1)}$, and three threefold degenerate basis states with irreducible representations of $\Gamma_4^{(3)}$. The basis states of $\Gamma_2^{(1)}$ and $\Gamma_3^{(1)}$ that form the TQW can be derived by imposing chiral cubic crystal symmetry and time-reversal symmetry:

$$\begin{aligned} \phi_{\Gamma_2} &= (e_{\text{Pt1}}^{\Gamma_2}, e_{\text{Pt2}}^{\Gamma_2}, e_{\text{Pt3}}^{\Gamma_2}, e_{\text{Pt4}}^{\Gamma_2}) \\ &= \frac{(1, \omega, \omega^2, -1, -\omega, \omega^2, -1, \omega, -\omega^2, 1, -\omega, -\omega^2)}{\sqrt{12}} \quad (89) \\ &, \\ \phi_{\Gamma_3} &= (e_{\text{Pt1}}^{\Gamma_3}, e_{\text{Pt2}}^{\Gamma_3}, e_{\text{Pt3}}^{\Gamma_3}, e_{\text{Pt4}}^{\Gamma_3}) \\ &= \frac{(1, \omega^2, \omega, -1, -\omega^2, \omega, -1, \omega^2, -\omega, 1, -\omega^2, -\omega)}{\sqrt{12}} \quad (90) \end{aligned}$$

where $\omega = e^{i2\pi/3}$. ϕ_{Γ_2} and ϕ_{Γ_3} have opposite chirality following $\phi_{\Gamma_2} = \phi_{\Gamma_3}^*$. In the vicinity of the Γ point, low-energy

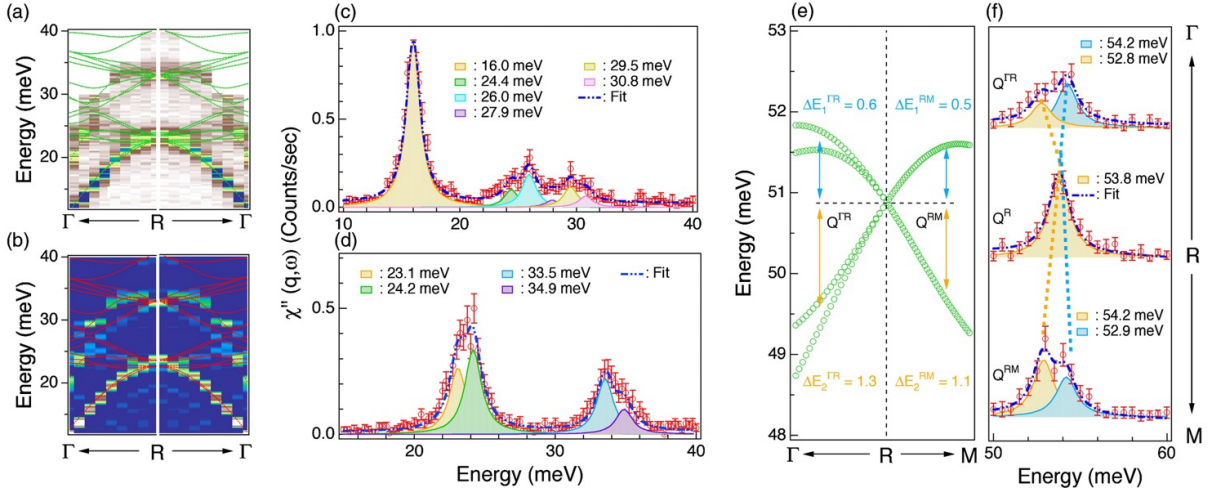


Figure 37 Evidence of charge-2 Dirac phonon in FeSi. (a), (b) Color plot and second derivative plot of phonon dynamical structure factor near the R point. (c) and (d) show high-statistic IXS spectra at $\mathbf{Q}=(4.26, 0.26, 0.26)$ and $(4.5, 0.5, 0.5)$, respectively. The dashed blue curves are the fitted result. (e) The charge-2 Dirac phonon in the 50 meV energy range. (f) shows the high statistic IXS spectra at $\mathbf{Q}^{\Gamma R}$, \mathbf{Q}^R , and \mathbf{Q}^{RM} . Adapted from Ref. (Miao *et al.*, 2018).

effective Hamiltonian for the twofold quadruple Weyl:

$$H(\mathbf{q}) = \begin{pmatrix} Aq_xq_yq_z & B^*(q_x^2 + \omega^2q_y^2 + \omega q_z^2) \\ B(q_x^2 + \omega^2q_y^2 + \omega q_z^2) & -Aq_xq_yq_z \end{pmatrix}, \quad (91)$$

where $\omega = e^{2\pi i/3}$, A is a real constant, and B is a complex constant. The q -dependent wave functions can be obtained by diagonalizing Eq. (91) in the ϕ_{Γ_2} and ϕ_{Γ_3} basis states. Along the [100] and [011] directions, the diagonal components of Eq. (91) are zero, imposing purely real wave functions, $\psi_1 = (e^{i\theta/2}\phi_{\Gamma_2} + e^{-i\theta/2}\phi_{\Gamma_3})/\sqrt{2}$ and $\psi_2 = -i(e^{i\theta/2}\phi_{\Gamma_2} - e^{-i\theta/2}\phi_{\Gamma_3})/\sqrt{2}$, where $\theta = \arg(B)$. In contrast, along the [111] direction, the off-diagonal components are zero yielding $\psi_1 = \phi_{\Gamma_2}$ and $\psi_2 = \phi_{\Gamma_3}$, which have large imaginary components. This simplified model analysis thus explains the directional wave function reported in (Li *et al.*, 2021a).

Following the similar spirit, (Jin *et al.*, 2022) showed that by quantitatively analysing the phonon dynamical structure, the Chern number can also be extracted. As an example, (Jin *et al.*, 2022) considered a twofold Weyl Hamiltonian:

$$H_{2 \times 2}(\mathbf{q}) = \sum_{i=x,y,z} f_i(\mathbf{q}) \cdot \sigma_i + f_0(\mathbf{q})\sigma_0 \quad (92)$$

where σ_i are the Pauli matrix. They then define a pseudospin:

$$S(\mathbf{q})_{1,2} = \frac{f(\mathbf{q})}{|f(\mathbf{q})|} = \langle \phi_{1,2} | \boldsymbol{\sigma} | \phi_{1,2} \rangle \quad (93)$$

where $\phi_{1,2}$ is the eigenvector of Eq. 92. The subscript 1 and 2 denote the upper and lower bands that form the Weyl node. The coherent scattering contribution for the inelastic neutron

scattering intensity (Eq. (25)) can then be written in the pseudospin quantities:

$$S_{coh} \propto |\mathbf{V}|(1 + \cos(\mathbf{S}(\mathbf{q}) \cdot \mathbf{V}(\mathbf{G}))) \quad (94)$$

where $\mathbf{V}(\mathbf{G})$ is a constant vector that does not sensitively depend on \mathbf{q} but varies by changing \mathbf{G} . Equation 94 shows that the INS intensity is sensitive to the projection of $\mathbf{S}(\mathbf{q})$ on $\mathbf{V}(\mathbf{G})$. This effect has been confirmed by an INS study of MnSi (Jin *et al.*, 2022). As shown in Fig. 39, the averaged INS intensity over solid \mathbf{q} spheres show maximum and minimum consistent with Eq. (94).

2. Topological Phonons Observed by EELS

Before 2023, experimental studies on topological phonons has remained restricted to select 3D single crystals analyzed via inelastic X-ray or neutron scattering techniques. Crucially, experimental confirmation of topological phonons in 2D materials has been lacking. Hereafter, (Li *et al.*, 2023a) employ surface sensitive high-resolution electron energy loss spectroscopy (HR-EELS) to directly map the phonon spectra of atomically thin graphene across its entire 2D Brillouin zone, as shown in Fig. 38. By comparing the experimentally determined phonon dispersion with the DFT calculations in the entire 2D Brillouin zone, (Li *et al.*, 2023a) identified two nodal-ring phonons and four Dirac phonons, as shown in Fig. 38 (c). Figure 38 (d) further show the 3D mapping of phonon spectra, which integrates 2D momentum space and energy dimensions, establishes a transformative framework for systematically identifying topological phononic states.

While topological phonons in the 3D and 2D bulk state have been extensively studied, the bulk-edge correspondence of

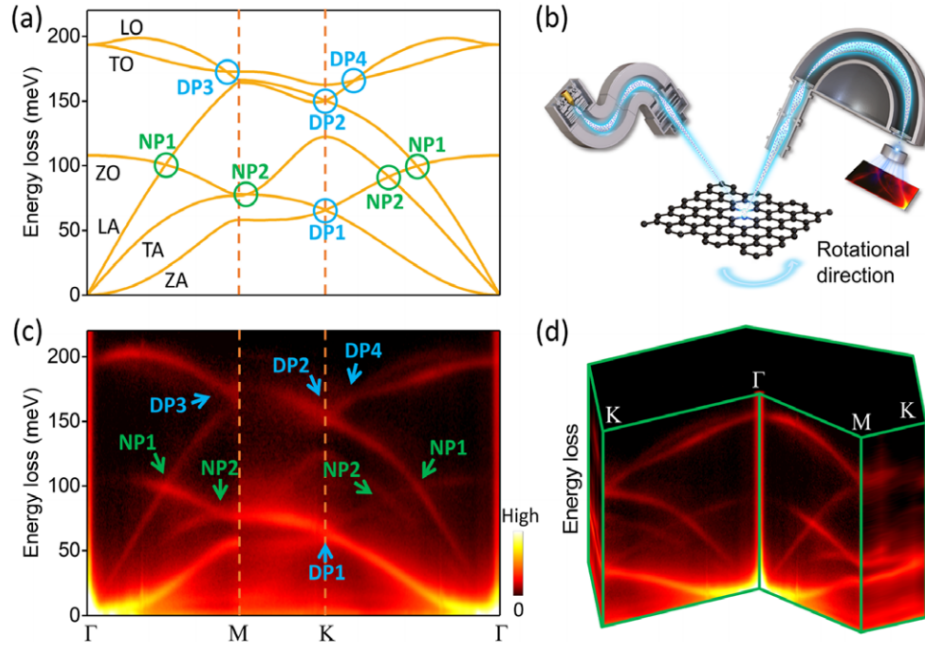


Figure 38 Phonon spectra and experimental setup for graphene. (a) Phonon bands obtained by first-principle calculations. Topological nodal-ring phonons (NPs, green circles) and Dirac phonons (DPs, blue circles) are highlighted. (b) Schematic illustration of the high-resolution electron energy loss spectroscopy (HR-EELS) experimental setup. (c) Experimental phonon spectra of graphene along the same high-symmetry paths as (a), with NPs and DPs marked by green and blue arrows, respectively. (d) 3D HR-EELS mapping of graphene phonon spectra, integrating momentum-space and energy-resolved measurements. Adapted from Ref. (Li *et al.*, 2023a).

topological phonons remain to be experimentally established. For this purpose, surface and local probes of phonon excitations are required. The ability to reveal the phonon spectrum of graphene in large momentum space making HR-EELS a promising tool to uncover phononic surface state in 3D systems (Miao *et al.*, 2018; Zhang *et al.*, 2018a, 2019b). The phononic surface mode may also be encoded in electronic spectral functions through quasiparticle interactions. For instance, the drumhead surface phonon mode has been predicted in MoB_2 and high- T_c conventional superconductor MgB_2 . Due to the strong electron-phonon coupling, the topological phonon edge mode can couple with the conducting electrons on the surface, giving rise to electronic kinks that can be revealed using angle-resolved photoemission spectroscopy.

B. Chiral Phonons

As we discussed in previous sections and showed in Fig. 33, topological and chiral phonons are deeply connected in the context of Weyl phonons (Zhang *et al.*, 2025b). In this respect, the observations of Weyl phonons and chiral phononic wave functions (Li *et al.*, 2021a; Miao *et al.*, 2018) also represent evidence of chiral phonons with circularly polarization. On the other hand, since chiral phonons are defined on AM of QPs, they are naturally connected to magnetism (Baydin *et al.*, 2022; Che *et al.*, 2024; Cheng *et al.*, 2020a; Fransson, 2023; Hernandez *et al.*, 2023; Hu *et al.*, 2021; Juraschek *et al.*, 2022;

Kim *et al.*, 2023; Li *et al.*, 2024; Mankovsky *et al.*, 2022; Nova *et al.*, 2017; Peters *et al.*, 2022; Ren *et al.*, 2021; Saparov *et al.*, 2022; Wu *et al.*, 2023; Xue *et al.*, 2025; Yang *et al.*, 2024b), thermal Hall effect (Chen *et al.*, 2020, 2022; Grissonnanche *et al.*, 2020, 2019; Kasahara *et al.*, 2018; Li *et al.*, 2020d, 2023b; Ohe *et al.*, 2024; Qin *et al.*, 2012; Zhang *et al.*, 2019c) and light-matter scattering processes (Bourgeois *et al.*, 2025; Che *et al.*, 2024; Ishito *et al.*, 2023a,b; Ueda *et al.*, 2023; Yang *et al.*, 2024b; Zhang and Niu, 2015; Zhang *et al.*, 2025a, 2023b; Zhang and Murakami, 2022; Zhang *et al.*, 2025b; Zhu *et al.*, 2018) and hence attracted significant interests in the community. In this section, we discuss recent experimental progresses that are specifically related to chiral phonons.

1. Experimental Signature of Phonon PAM

The circular dichroism (CD) in the light-matter scatterings has been used to probe chiral phonons. Due to the PAM conservation, the microscopic light-matter scattering processes involving chiral phonons display large CD effect. Interestingly, it has been found that (Bourgeois *et al.*, 2025; Ishito *et al.*, 2023a,b; Zhang and Niu, 2015; Zhang *et al.*, 2025a, 2023b; Zhang and Murakami, 2022; Zhang *et al.*, 2025b; Zhu *et al.*, 2018) the light-matter scattering can display new selection rules when the incident photon momentum, k_i , and scattered photon momentum, k_f , are along the rotational axis. Figure 40 (a) shows Stokes and anti-Stokes Raman spectra of

a truly chiral phonon system α -HgS. The red and blue curves correspond to the $\Gamma_3^{(2)}$ doublet phonon modes and are obtained in $(\epsilon_i, \epsilon_f)=(L, R)$ and (R, L) polarization conditions, respectively. Here L and R stand for circular left and circular right polaritons with photon PAM $\sigma_L=-1$ and $\sigma_R=+1$. Notably, the PAM conservation for a C_3 -symmetric direction enforces a selection rule: $\sigma_f - \sigma_i = -l_q^{ph} \bmod 3$, in agreement with experimental observations. The chiral-phonon-driven CD has also been observed in a resonant inelastic x-ray scattering (RIXS) study of chiral quartz crystals as shown in Fig. 40 (b). It is important to note that the CD in RIXS is not a direct consequence of PAM conservation as k_i and k_f are not along the rotational axis. Instead, it arises from the coupling between chiral phonons and the RIXS intermediate states, which shows different scattering cross-section under L and R polarizations. Chiral phonons have also been observed in 2D using ultrafast pump-probe techniques (Britt and Siwick, 2023; Zhang *et al.*, 2025c; Zhu *et al.*, 2018). Figure 40 (c) shows the indirect optical transitions in a transition metal dichalcogenides WSe₂. The absence of inversion symmetry in WSe₂ lifts the degeneracy of chiral phonon modes at the K and K' valleys. The photon excited hole, $h_A(K)$, at the valence band of the K -valley are scattered, through its polarization dependent interactions with chiral phonons, to the spin-split conduction band, $h_B(K')$, of the K' -valley, yielding CD in the time domain [Fig. 40 (b2)] and a characteristic chiral phonon energy, 29 ± 8 meV, at delay time $t = 0.8$ ps [Fig. 40 (b3)].

Although CD provides important signature of chiral phonons, it should be emphasized that CD is sensitive to chirality rather than AM. It thus calls for experimental protocols to directly reveal the AM of phonons. Historically, the AM of microscopic quantum objects, such as the AM of electron spin, has been determined through the Einstein-de Hass (EdH) effect (Einstein, 1915; Frenkel, 1979; Gans, 1916): due to total AM conservation, the suspended ferromagnet displays a macroscopic mechanical rotation under external magnetic field to compensate the total AM of microscopic spins. Motivated by this concept, it is proposed that the AM of chiral phonon can induce mechanical rotations under a thermal gradient that breaks the time-reversal symmetry (Hamada *et al.*, 2018). In the equilibrium condition, the phonon-AM can be expressed as:

$$\mathbf{J}_{ph} = \sum_{\mathbf{k}, \sigma} \mathbf{l}_\sigma [f_0(\omega_\sigma(\mathbf{k})) + \frac{1}{2}] \quad (95)$$

where $f_0(\omega_\sigma(\mathbf{k})) = 1/(e^{\frac{\hbar\omega_\sigma(\mathbf{k})}{k_B T}} - 1)$ is the Bose distribution function. In the presence of small thermal gradient, the phonon distribution function, $n_\sigma(\mathbf{q})$, can be approximately described by the Boltzmann equation:

$$n_\sigma(\mathbf{q}) = f_0(\omega_\sigma(\mathbf{k})) - t_0(v_\sigma(\mathbf{k}) \cdot \nabla T) \frac{\partial f_0(\omega_\sigma(\mathbf{k}))}{\partial T}, \quad (96)$$

where $v_\sigma(\mathbf{k})$ is the group velocity of the phonon mode σ , and

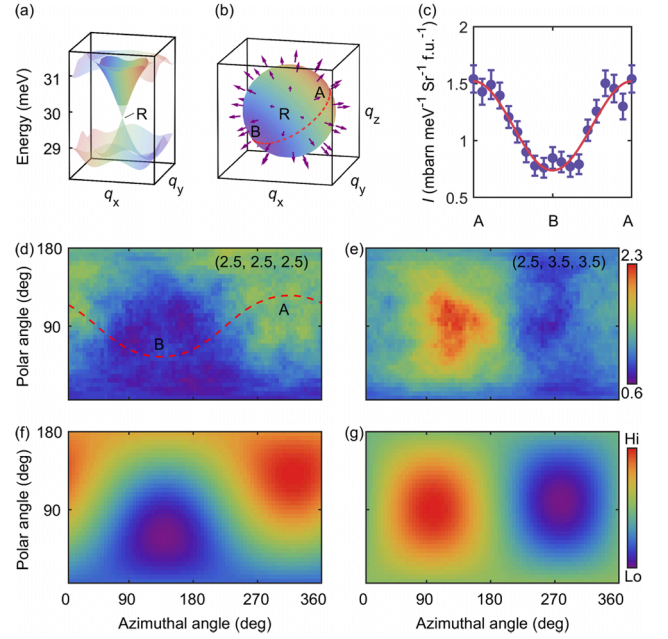


Figure 39 (a) Phonon dispersions near the charge-2 Dirac point in MnSi. Solid color indicates energy integration range (30–32 meV). (b) Pseudospin texture enclosing the R point. (c) INS intensity along the red circle in (b). (d) and (e) INS intensities over \mathbf{q} spheres enclosing the momentum of (2.5, 2.5, 2.5) and (2.5, 3.5, 3.5), respectively. (f) and (g) Fitted-force-constant model calculations according to Eq. (94), for the same \mathbf{q} spheres as in (d) and (e), respectively. Adapted from Ref. (Jin *et al.*, 2022)

t_0 is the relaxation time. Following Eq. (95), the thermal gradient induced total phonon AM is:

$$\delta J_{ph} = \int \frac{d^3\mathbf{k}}{(2\pi)^3} \sum_{\sigma} \mathbf{l}_\sigma(\mathbf{k}) t_0(v_\sigma(\mathbf{k}) \cdot \nabla T) \frac{\omega_\sigma(\mathbf{k})}{T} \frac{\partial n_{eq}(\omega_\sigma(\mathbf{k}))}{\partial \omega_\sigma(\mathbf{k})}. \quad (97)$$

Fundamentally, Eq. (95)-(97) is similar to the Edelstein effect in electronic systems (Einstein, 1915; Frenkel, 1979; Gans, 1916). The presence of thermal gradient will induce mechanical torque, $\tau \sim \frac{\delta J_{ph}}{t_0}$. Recently, using a cantilever-based method, the phonon AM induced mechanical torque has been observed in chiral single crystal Te (Zhang *et al.*, 2024a). The experimentally determined $\tau \sim 5 \times 10^{-11} \text{ N} \cdot \text{m}$ is remarkably consistent with theoretical calculations, supporting phonon AM in chiral crystals.

2. Experimental Evidence of Chiral Phonons Coupled with Magnetism

In real space, chiral phonons correspond to collective circular motions of charged ions. Therefore, chiral phonons can carry finite magnetic moment on the order of $\mu_{ph} \sim e\hbar/(2m_{ion})$, where m_{ion} is the ionic mass that is much larger than the electron mass, m_e , yielding $\mu_{ph}/\mu_B \sim 10^{-3} -$

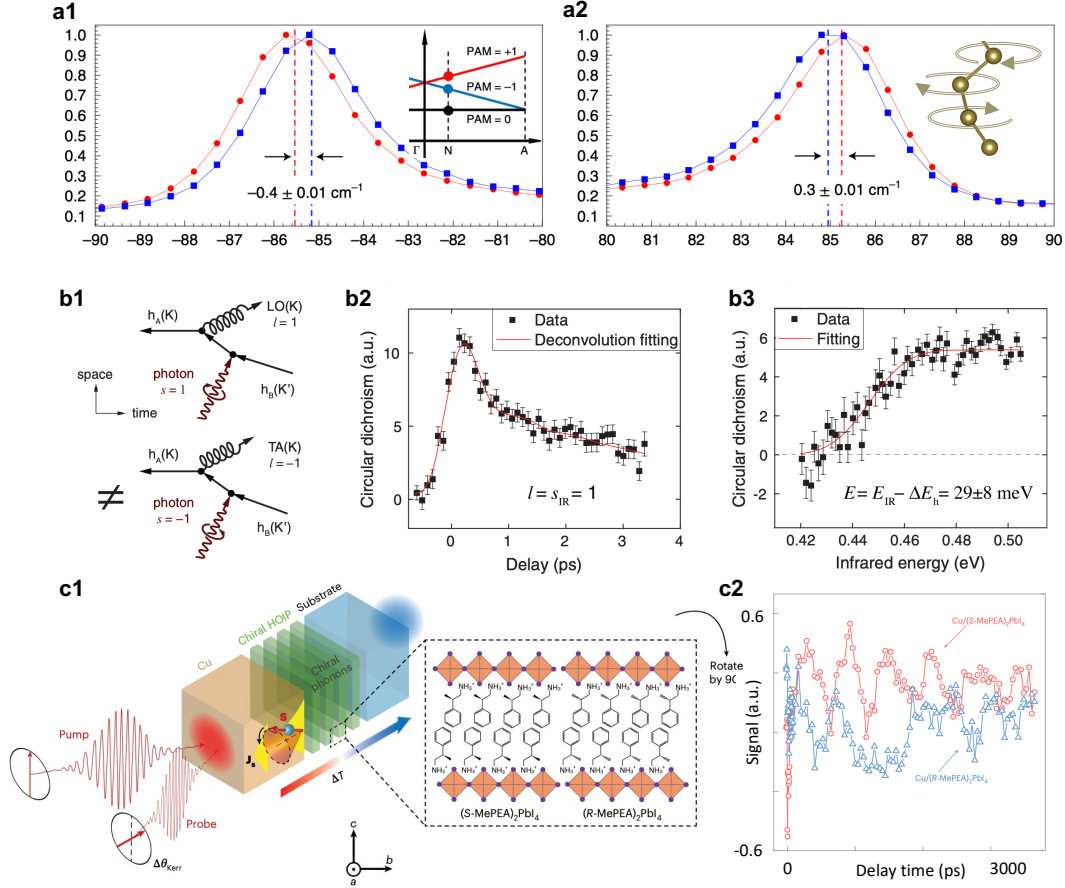


Figure 40 Anti-Stokes (a1) and Stokes (a2) spectra of a doubly degenerate chiral phonon modes in α -HgS. Chiral optical phonons slightly away from the Γ point with PAM=+1 (red) and -1 (blue) are selectively probed under $(\hat{\epsilon}_i, \hat{\epsilon}_f)=(L, R)$ and (R, L) polarization conditions. Here, L and R stand for left and right circular polarization, respectively (Ishito *et al.*, 2023a). (b1)-(b3) show chiral phonon driven circular dichroism (CD) in the indirect optical transitions in WSe₂ (Zhu *et al.*, 2018). $h_A(K)$ and $h_B(K')$ represent holes at the valence band of the K valley and the spin-split band of the K' valley, respectively. The experimentally determined CD at 82 K and transient CD acquired at delay time, $\tau=0.8$ ps [(b2)], are used to estimate a chiral phonon energy 29 ± 8 meV [(b3)], in agreement with first principles calculations. (c1)-(c2) show experimental signature of a chiral-phonon-activated spin Seebeck effect (Kim *et al.*, 2023). Applying transient thermal gradient on left- and right-handed materials [(c1)] yields spin currents with a π -phase difference [(c2)]. Adapted from Ref. (Ishito *et al.*, 2023b; Kim *et al.*, 2023; Zhu *et al.*, 2018)

10^{-5} . Surprisingly, recent experimental studies have shown giant phonon magnetic moments, $g_{ph}\mu_{ph} \sim g\mu_B$, in various semimetals and semiconductors, including CeCl₃, Cd₃As₂, PbTe, and Fe₂Mo₃O₈ (Baydin *et al.*, 2022; Cheng *et al.*, 2020a; Juraschek *et al.*, 2022; Wu *et al.*, 2023). To understand these observations, Ren *et al.* pictured the phonon magnetic moment as electronic orbital magnetization in an adiabatic response to the underlying ionic circular motions (Ren *et al.*, 2021). They reformulated the phonon magnetism by introducing a momentum k -dependent Born effective charge and discovered a topological magnetization term, which arises from the chiral phonon-modified electronic energy with non-trivial Berry curvature. In topological semimetals and insulators, integration of the Berry curvature near the Yang's monopole gives rise to giant phonon magnetic moment, $g_{ph}\mu_{ph} \sim g\mu_B$. Interestingly, a recent time-domain spectroscopy study of $Pb_{1-x}Sn_xTe$ films showed that crossing the topological in-

sulator to trivial insulator phase boundary yields a 3-order of magnitude reduction of $g_{ph}\mu_{ph}$ in agreement with theoretical predictions.

In the presence of spin-orbital coupling, chiral phonons induce spin magnetization via dynamical modulation of electronic states. It is theoretically demonstrated (Hamada and Murakami, 2020a; Yao and Murakami, 2024) that due to the time-dependent Hamiltonian by the chiral phonons, the expectation value of the spin against a Berry-phase term, and becomes nonzero in the presence of chiral phonons. Similarly, in magnets with localized spins, it is theoretically shown that the chiral phonons change the total magnetization by the Berry phase term in the magnon population (Yao and Murakami, 2024).

The coupling between chiral phonon and magnetism has also been suggested in ultrafast optical studies of nonequilibrium states. Figure 40 (c) shows an experimental observation

of a chiral-phonon-activated spin Seebeck effect (CPASS). Shining an ultrafast laser pulse builds a transient temperature gradient across the heterostructure and excite chiral phonons from the non-magnetic 2D hybrid organic-inorganic perovskite (HOIP). It has been argued that the AM of chiral phonons is transferred to electrons in the Cu, resulting in spin currents without external magnetic fields. The generated spin current is then probed by the time-resolved Kerr rotation angle $\Delta\theta_{\text{kerr}}$. By switching the handedness of HOIP from left (S, red) to right (R, blue), the oscillating Kerr signal in the time domain shows a π -phase shift, consistent with the chirality-dependence of the spin current. Intriguingly, Kim et al. estimated the CPASS coefficient in their setup and obtained a value that is 1~3 orders greater than the conventional spin Seebeck coefficient based on magnetic materials (Kim et al., 2023). Another interesting observation showing chiral phonon mediated demagnetization has been reported recently. Recently, another ultrafast diffraction study of magnetic Ni reported evidence of nearly instantaneous but long-lasting chiral phonons (Tauchert et al., 2022). (Stupakiewicz et al., 2021) interpreted their observations as a rapid AM transfer process between electrons and chiral phonons that occurs before the macroscopic rotation happens. This observation provides insights into a fundamental question in ultrafast demagnetization and may help to understand the time-scale of phonon Einstein-de Haas effect.

Chiral phonons have broader interests in the context of quantum information science. It has been predicted the phonon AM can contribute to the phonon Einstein-de Haas effect (Hamada et al., 2018). Applying heat flow through a chiral crystal breaks \mathcal{T} and causes rigid body rotations. (Kong et al., 2022) showed that chiral phonons can selectively light up dark excitons from different valleys of MoSi_2N_4 in the photoexcitation process, yielding a chiral phonon-triggered photoluminescence. Chiral phonons were also considered for non-reciprocal thermal transport (Chen et al., 2020, 2022; Grissonnanche et al., 2020, 2019; Kasahara et al., 2018; Li et al., 2020d, 2023b; Ohe et al., 2024; Qin et al., 2012; Zhang et al., 2019c). More recently, chiral phonons were proposed to detect dark matter through its non-gravitational interaction with standard-model matter (Romao et al., 2023). Furthermore, quasiparticle interactions between topological magnon, polaron, and phonon were predicted to give rise to chiral edge phonon modes for future heat management of microelectronic devices.

VII. CONCLUSIONS AND PERSPECTIVES

We end this review by discussing open questions in this fast-developing field.

Topological Phonons. Like electronic systems, topological phonons can give rise to phononic edge mode. It has been predicted that the double helicoidal surface phonon modes will emerge in transition metal monosilicides, such as FeSi and CoSi (Jin et al., 2022; Miao et al., 2018; Zhang et al.,

2018a), whereas the flat surface phonon modes can be realized in MoB_2 (Zhang et al., 2019b) and high- T_c conventional superconductor MgB_2 (Li et al., 2020c). Experimental observation of these novel topological edge modes will be important for the understanding of topological bosonic excitations and related physical consequences. Surface sensitive probes, such as HR-EELS, will be a powerful technique to resolve this issue. IXS with grazing incident condition may also provide key insights.

Furthermore, the coupling between topological phonon and topological electron remain largely unexplored. These couplings are expected to be important in Weyl semimetals, such as CoSi, where both Weyl phonon and Weyl fermions are crucial for transport properties. The coupling between Weyl electron and phonon can give rise to non-linear Hall effect (Gao et al., 2020; He et al., 2019). The topological quasiparticle interactions can also be important for spontaneous symmetry-breaking orders, such as charge/spin density waves (Luo et al., 2018; Miao et al., 2024; Yang et al., 2024a; Zhang et al., 2024b), quantum Hall effects (Luo et al., 2018), and superconductivity (Gao et al., 2023; Grissonnanche et al., 2020). The localized surface/edge states induced by nontrivial bulk band topology support peculiarly large density of states for both electrons and phonons, which may give rise to enhanced electron-phonon couplings at some interfaces. (Di Miceli et al., 2022) has shown that topological phonons can play important roles in superconductivity. Investigations along this direction may help deepen our understanding about phonon-mediated superconductivity. Understanding of these topological quasiparticle interactions may also pave the way for practical applications, *e.g.*, nonreciprocal transport and enhanced thermoelectric conversion efficiency (Xu et al., 2014).

Chiral Phonons. Previous experimental studies suggest that chiral phonons may couple to magnetic degree of freedom. However, quantitative understanding of the coupling remains unresolved. For instance, it has been known that chiral structure can induce spin polarized current (Göhler et al., 2011; Naaman et al., 2019; Naaman and Waldeck, 2012; Ray et al., 1999). A recent theoretical study showed that this chirality-induced spin selectivity arises from spin-orbital coupling, which polarizes electron spin rather than filters spin (Wolf et al., 2022).

The coupling between chiral phonons and magnetism may also help to shed light in the unusual thermal transport behaviors in correlated and topological materials. As one of the main heat carriers, phonons are critical for thermal conductivity. For a long time, the phonon contribution to the thermal Hall conductivity, κ_{xy} , has been overlooked due to the small phonon magnetic moment and hence negligible responses under magnetic fields. Recently, giant κ_{xy} was observed in many strongly correlated insulators, including the cuprate high- T_c superconductors (Grissonnanche et al., 2020), Kitaev spin liquid candidate $\alpha\text{-RuCl}_3$ (Kasahara et al., 2018), quantum paraelectric SrTiO_3 (Li et al., 2020d). Empirically, THE in these insulators displays two ubiquitous features: (1) longitudinal and transverse thermal conductivity peak at the same temper-

ature, and (2) $\kappa_{xy}/\kappa_{xx} \sim 10^{-3}$ around $B \sim 10$ T. These observations suggest that the unusually large THE has a phonon origin. Phenomenologically, the transverse conductivity can be written as $\kappa_{xy} = \frac{1}{\nu} \sum_{\gamma} C^{\gamma} (v_{xy}^{\gamma} l^{\gamma} + l_{xy}^{\gamma} v^{\gamma})$, where C , v , and l are the specific heat, phonon velocity, and mean-free path, respectively. γ is the index of phonon modes, and ν is a dimension-dependent constant. Like electrons, the phonon THE has intrinsic contribution from phonon Berry curvature (Qin *et al.*, 2012; Zhang *et al.*, 2010) and extrinsic contribution from skew scattering and side-jump (Chen *et al.*, 2020). However, it has been found that the intrinsic effect is usually orders of magnitude smaller than experimental observations. These experimental observations call for further theoretical study of the coupling between phonons and their embedded environments (Chen *et al.*, 2022; Grissonnanche *et al.*, 2019; Li *et al.*, 2023b; Zhang *et al.*, 2019c).

In summary, topological and chiral phonons represent a transformative frontier in condensed matter physics. These unconventional lattice excitations exhibit nontrivial topology and carry (pseudo-)angular momentum that are important to understand light-matter scattering, thermal transport, and emergent symmetry breaking and topological orders. These concepts expand the understanding of symmetry, topology, and transport in crystalline solids, with promising implications for both fundamental science and quantum technologies.

VIII. ACKNOWLEDGEMENTS

T.Z. acknowledges the support from the National Key R&D Project (Grant Nos. 2023YFA1407400 and 2024YFA1400036) and the National Natural Science Foundation of China (Grant Nos. 12374165 and 12047503). Y.L. is supported by the Innovation Program for Quantum Science and Technology (Grant No. 2023ZD0300500), the National Natural Science Foundation of China (Grant No. 12404279), and Shanghai Pujiang Program (Grant No. 23PJ1413000). H.M. is supported by the US Department of Energy, Office of Science, Basic Energy Sciences, Materials Sciences and Engineering Division. S.M. is supported by JSPS KAKENHI Grant Nos. JP22H00108 and JP24H02231.

REFERENCES

- Ahn, Junyeong, Dongwook Kim, Youngkuk Kim, and Bohm-Jung Yang (2018), “Band Topology and Linking Structure of Nodal Line Semimetals with Z_2 Monopole Charges,” *Phys. Rev. Lett.* **121** (10), 106403.
- Ahn, Junyeong, Sungjoon Park, Dongwook Kim, Youngkuk Kim, and Bohm-Jung Yang (2019), “Stiefel–Whitney classes and topological phases in band theory,” *Chin. Phys. B* **28** (11), 117101.
- Altland, Alexander, and Martin R. Zirnbauer (1997), “Nonstandard symmetry classes in mesoscopic normal-superconducting hybrid structures,” *Phys. Rev. B* **55**, 1142–1161.
- Ament, Luuk JP, Michel Van Veenendaal, Thomas P Devereaux, John P Hill, and Jeroen Van Den Brink (2011), “Resonant inelastic x-ray scattering studies of elementary excitations,” *Reviews of Modern Physics* **83** (2), 705–767.
- Ando, Yoichi (2013), “Topological insulator materials,” *Journal of the Physical Society of Japan* **82** (10), 102001.
- Ando, Yoichi, and Liang Fu (2015), “Topological crystalline insulators and topological superconductors: From concepts to materials,” *Annu. Rev. Condens. Matter Phys.* **6** (1), 361–381.
- Armitage, N P, E. J. Mele, and Ashvin Vishwanath (2018), “Weyl and Dirac semimetals in three-dimensional solids,” *Rev. Mod. Phys.* **90** (1), 015001.
- Avron, Joseph E, Ruedi Seiler, and Barry Simon (1983), “Homotopy and quantization in condensed matter physics,” *Physical review letters* **51** (1), 51.
- Barron, Laurence D (2021), “Symmetry and chirality: where physics shakes hands with chemistry and biology,” *Israel Journal of Chemistry* **61** (9-10), 517–529.
- Basov, D N, and T. Timusk (2005), “Electrodynamics of high- T_c superconductors,” *Rev. Mod. Phys.* **77**, 721–779.
- Baydin, Andrey, Felix GG Hernandez, Martin Rodriguez-Vega, Anderson K Okazaki, Fuyang Tay, G Timothy Noe, Ikufumi Katayama, Jun Takeda, Hiroyuki Nojiri, Paulo HO Rappl, *et al.* (2022), “Magnetic control of soft chiral phonons in pbte,” *Physical review letters* **128** (7), 075901.
- Bermudez, A, MA Martin-Delgado, and A Luis (2008), “Chirality quantum phase transition in the Dirac oscillator,” *Physical Review A—Atomic, Molecular, and Optical Physics* **77** (6), 063815.
- Bernevig, B Andrei (2013), *Topological insulators and topological superconductors* (Princeton university press).
- Berry, Michael Victor (1984), “Quantal phase factors accompanying adiabatic changes,” *Proc. R. Soc. Lond. A* **392** (1802), 45–57.
- Borisenko, Sergey, Quinn Gibson, Danil Evtushinsky, Volodymyr Zabolotnyy, Bernd Büchner, and Robert J Cava (2014), “Experimental realization of a three-dimensional Dirac semimetal,” *Physical review letters* **113** (2), 027603.
- Bourgeois, Marc R, Andrew W Rossi, and David J Masiello (2025), “Strategy for direct detection of chiral phonons with phase-structured free electrons,” *Physical Review Letters* **134** (2), 026902.
- Bousquet, Eric, Mauro Fava, Zachary Romestan, Fernando Gómez-Ortiz, Emma E McCabe, and Aldo H Romero (2024), “Structural chirality and related properties in the periodic inorganic solids: Review and perspectives,” *Journal of Physics: Condensed Matter*.
- Bradlyn, Barry, Jennifer Cano, Zhijun Wang, MG Vergniory, C Felser, Robert Joseph Cava, and B Andrei Bernevig (2016), “Beyond Dirac and Weyl fermions: Unconventional quasiparticles in conventional crystals,” *Science* **353** (6299), aaf5037.
- Bradlyn, Barry, Luis Elcoro, Jennifer Cano, Maia G Vergniory, Zhijun Wang, Claudia Felser, Mois I Aroyo, and B Andrei Bernevig (2017), “Topological quantum chemistry,” *Nature* **547** (7663), 298–305.
- Britt, Tristan L, and Bradley J Siwick (2023), “Ultrafast phonon diffuse scattering as a tool for observing chiral phonons in monolayer hexagonal lattices,” *Physical Review B* **107** (21), 214306.
- Brydson, Rik (2020), *Electron energy loss spectroscopy* (Garland Science).
- Burgess, Cliff, and Guy Moore (2007), *The standard model: A primer* (Cambridge University Press).
- Burkov, AA (2016), “Topological semimetals,” *Nature materials* **15** (11), 1145–1148.
- Burkov, AA, MD Hook, and Leon Balents (2011), “Topological nodal semimetals,” *Physical Review B—Condensed Matter and Materials Physics* **84** (23), 235126.
- Cai, Xiangxi, Liping Ye, Chunyin Qiu, Meng Xiao, Rui Yu, Manzhu Ke, and Zhengyou Liu (2020), “Symmetry-enforced

- three-dimensional Dirac phononic crystals,” *Light: Science & Applications* **9** (1), 38.
- Cano, Jennifer, and Barry Bradlyn (2021), “Band Representations and Topological Quantum Chemistry,” *Annu. Rev. Condens. Matter Phys.* (Volume 12, 2021), 225–246.
- Castro Neto, A H, F. Guinea, N. M. R. Peres, K. S. Novoselov, and A. K. Geim (2009), “The electronic properties of graphene,” *Rev. Mod. Phys.* **81** (1), 109–162.
- Chang, Cui-Zu, Chao-Xing Liu, and Allan H MacDonald (2023), “Colloquium: Quantum anomalous Hall effect,” *Reviews of Modern Physics* **95** (1), 011002.
- Chang, Cui-Zu, Jinsong Zhang, Xiao Feng, Jie Shen, Zuocheng Zhang, Minghua Guo, Kang Li, Yunbo Ou, Pang Wei, Li-Li Wang, *et al.* (2013), “Experimental observation of the quantum anomalous Hall effect in a magnetic topological insulator,” *Science* **340** (6129), 167–170.
- Che, Mengqian, Jinxuan Liang, Yunpeng Cui, Hao Li, Bingru Lu, Wenbo Sang, Xiang Li, Xuebin Dong, Shuai Zhang, Tao Sun, *et al.* (2024), “Magnetic order induced truly chiral phonons in a ferromagnetic Weyl semimetal,” arXiv preprint arXiv:2411.03754.
- Chen, Jing-Yuan, Steven A Kivelson, and Xiao-Qi Sun (2020), “Enhanced thermal Hall effect in nearly ferroelectric insulators,” *Physical Review Letters* **124** (16), 167601.
- Chen, Lu, Marie-Eve Boulanger, Zhi-Cheng Wang, Fazel Tafti, and Louis Taillefer (2022), “Large phonon thermal Hall conductivity in the antiferromagnetic insulator CuTeO_6 ,” *Proceedings of the National Academy of Sciences* **119** (34), e2208016119.
- Chen, Xie, Fiona J Burnell, Ashvin Vishwanath, and Lukasz Fidkowski (2015), “Anomalous symmetry fractionalization and surface topological order,” *Physical Review X* **5** (4), 041013.
- Chen, Xing-Qiu, Jiayi Liu, and Jiangxu Li (2021a), “Topological phononic materials: Computation and data,” *Innovation* **2** (3), 2666–6758.
- Chen, Y S, F. F. Huang, P. Zhou, Z. S. Ma, and L. Z. Sun (2021b), “Ideal topological phononic nodal chain in K_2O materials class,” *New J. Phys.* **23** (10), 103043.
- Cheng, Bing, T Schumann, Yucheng Wang, X Zhang, D Barbalas, S Stemmer, and NP Armitage (2020a), “A large effective phonon magnetic moment in a Dirac semimetal,” *Nano letters* **20** (8), 5991–5996.
- Cheng, Hengbin, Yixin Sha, Rongjuan Liu, Chen Fang, and Ling Lu (2020b), “Discovering topological surface states of Dirac points,” *Physical Review Letters* **124** (10), 104301.
- Deng, Yujun, Yijun Yu, Meng Zhu Shi, Zhongxun Guo, Zihan Xu, Jing Wang, Xian Hui Chen, and Yuanbo Zhang (2020), “Quantum anomalous Hall effect in intrinsic magnetic topological insulator MnBi_2Te_4 ,” *Science* **367** (6480), 895–900.
- Devereaux, Thomas P, and Rudi Hackl (2007), “Inelastic light scattering from correlated electrons,” *Rev. Mod. Phys.* **79**, 175–233.
- Di Miceli, Daniele, Chandan Setty, and Alessio Zaccone (2022), “Theory of superconductivity mediated by topological phonons,” *Phys. Rev. B* **106** (5), 054502.
- Ding, Guangqian, Feng Zhou, Zeying Zhang, Zhi-Ming Yu, and Xiaotian Wang (2022), “Charge-two Weyl phonons with type-iii dispersion,” *Physical Review B* **105** (13), 134303.
- Ding, Zhong-Ke, Yu-Jia Zeng, Wangping Liu, Li-Ming Tang, and Ke-Qiu Chen (2024), “Topological Phonons and Thermoelectric Conversion in Crystalline Materials,” *Adv. Funct. Mater.* **34** (33), 2401684.
- Dirac, Paul Adrien Maurice (1928), “The quantum theory of the electron,” *Proc. R. Soc. London A* **117** (778), 610–624.
- Egerton, Ray F (2011), *Electron energy-loss spectroscopy in the electron microscope* (Springer Science & Business Media).
- Einstein, A (1915), “Experimental proof of ampère’s molecular currents,” *Verh Dtsch Phys Ges* **17**, 152.
- Elcoro, Luis, Benjamin J. Wieder, Zhida Song, Yuanfeng Xu, Barry Bradlyn, and B. Andrei Bernevig (2021), “Magnetic topological quantum chemistry,” *Nat. Commun.* **12** (5965), 1–10.
- Fang, Chen, Yige Chen, Hae-Young Kee, and Liang Fu (2015), “Topological nodal line semimetals with and without spin-orbital coupling,” *Phys. Rev. B* **92** (8), 081201.
- Fang, Chen, Matthew J Gilbert, Xi Dai, and B Andrei Bernevig (2012), “Multi-Weyl topological semimetals stabilized by point group symmetry,” *Physical review letters* **108** (26), 266802.
- Fang, Chen, Ling Lu, Junwei Liu, and Liang Fu (2016), “Topological semimetals with helicoid surface states,” *Nature Physics* **12** (10), 936–941.
- Feigin, LA, Dmitri Iwanowitsch Svergun, *et al.* (1987), *Structure analysis by small-angle X-ray and neutron scattering*, Vol. 1 (Springer).
- Fischer, Martin C, Jesse W Wilson, Francisco E Robles, and Warren S Warren (2016), “Invited review article: pump-probe microscopy,” *Review of Scientific Instruments* **87** (3).
- Fransson, Jonas (2023), “Chiral phonon induced spin polarization,” *Physical Review Research* **5** (2), L022039.
- Frenkel, Viktor Ya (1979), “On the history of the einstein–de haas effect,” *Soviet Physics Uspekhi* **22** (7), 580.
- Fu, Hua-Hua, Gui-Fang Du, Dan-Dan Wu, Qing-Bo Liu, and Ruqian Wu (2019), “Spin-orbit coupling induced robust spin-seebeck effect and pure thermal spin currents in achiral molecule systems,” *Physical Review B* **100** (8), 085407.
- Fu, Liang (2011), “Topological crystalline insulators,” *Physical review letters* **106** (10), 106802.
- Fu, Liang, and Charles L Kane (2007), “Topological insulators with inversion symmetry,” *Physical Review B—Condensed Matter and Materials Physics* **76** (4), 045302.
- Fu, Liang, Charles L Kane, and Eugene J Mele (2007), “Topological insulators in three dimensions,” *Physical review letters* **98** (10), 106803.
- Fushitani, Mizuho (2008), “Applications of pump-probe spectroscopy,” *Annual Reports Section “C”(Physical Chemistry)* **104**, 272–297.
- Gans, R (1916), “Über paramagnetismus,” *Annalen der Physik* **355** (10), 163–198.
- Gao, Yang, Furu Zhang, and Wei Zhang (2020), “Second-order nonlinear Hall effect in Weyl semimetals,” *Physical Review B* **102** (24), 245116.
- Gao, Yi, Yang Pan, Jun Zhou, and Lifa Zhang (2023), “Chiral phonon mediated high-temperature superconductivity,” *Physical Review B* **108** (6), 064510.
- Ghaemi, Pouyan, Jérôme Cayssol, Donna N Sheng, and Ashvin Vishwanath (2012), “Fractional topological phases and broken time-reversal symmetry in strained graphene,” *Physical review letters* **108** (26), 266801.
- Göhler, B, V Hamelbeck, TZ Markus, M Kettner, GF Hanne, Zeev Vager, Ron Naaman, and H Zacharias (2011), “Spin selectivity in electron transmission through self-assembled monolayers of double-stranded dna,” *Science* **331** (6019), 894–897.
- Grissonnanche, G, S Thériault, A Gourgout, M-E Boulanger, E Lefrançois, A Ataei, F Laliberté, M Dion, J-S Zhou, S Pyon, *et al.* (2020), “Chiral phonons in the pseudogap phase of cuprates,” *Nature Physics* **16** (11), 1108–1111.
- Grissonnanche, Gaël, Anaëlle Legros, Sven Badoux, Etienne Lefrançois, Victor Zatzko, Maude Lizaire, Francis Laliberté, Adrien Gourgout, J-S Zhou, Sunseng Pyon, *et al.* (2019), “Giant thermal Hall conductivity in the pseudogap phase of cuprate superconductors,” *Nature* **571** (7765), 376–380.

- Haldane, F D M, and S. Raghu (2008), “Possible Realization of Directional Optical Waveguides in Photonic Crystals with Broken Time-Reversal Symmetry,” *Phys. Rev. Lett.* **100** (1), 013904.
- Haldane, F Duncan M (1988), “Model for a quantum Hall effect without landau levels: Condensed-matter realization of the “parity anomaly”,” *Physical review letters* **61** (18), 2015.
- Hamada, Masato, Emi Minamitani, Motoaki Hirayama, and Shuichi Murakami (2018), “Phonon angular momentum induced by the temperature gradient,” *Phys. Rev. Lett.* **121**, 175301.
- Hamada, Masato, and Shuichi Murakami (2020a), “Conversion between electron spin and microscopic atomic rotation,” *Physical Review Research* **2** (2), 023275.
- Hamada, Masato, and Shuichi Murakami (2020b), “Phonon rotoelectric effect,” *Physical Review B* **101** (14), 144306.
- Hangyo, M, M Tani, and T Nagashima (2005), “Terahertz time-domain spectroscopy of solids: a review,” *International journal of infrared and millimeter waves* **26**, 1661–1690.
- Hansen, Jean Pierre, and Michael L Klein (1976), “Dynamical structure factor $s(q \rightarrow, \omega)$ of rare-gas solids,” *Physical Review B* **13** (2), 878.
- Hasan, M Z, and C. L. Kane (2010), “Colloquium: Topological insulators,” *Rev. Mod. Phys.* **82** (4), 3045–3067.
- Hasan, M Zahid, and Joel E Moore (2011), “Three-dimensional topological insulators,” *Annu. Rev. Condens. Matter Phys.* **2** (1), 55–78.
- Hatsugai, Yasuhiro (1993), “Chern number and edge states in the integer quantum Hall effect,” *Physical review letters* **71** (22), 3697.
- He, LP, XC Hong, JK Dong, J Pan, Z Zhang, J Zhang, and SY Li (2014), “Quantum transport evidence for the three-dimensional Dirac semimetal phase in Cd_3As_2 ,” *Physical review letters* **113** (24), 246402.
- He, Pan, Steven S-L Zhang, Dapeng Zhu, Shuyuan Shi, Olle G Heinonen, Giovanni Vignale, and Hyunsoo Yang (2019), “Nonlinear planar Hall effect,” *Physical review letters* **123** (1), 016801.
- Healy, WP (1977), “A generalization of the kramers-heisenberg dispersion formula,” *Physical Review A* **16** (4), 1568.
- Hernandez, Felix GG, Andrey Baydin, Swati Chaudhary, Fuyang Tay, Ikufumi Katayama, Jun Takeda, Hiroyuki Nojiri, Anderson K Okazaki, Paulo HO Rappl, Eduardo Abramof, *et al.* (2023), “Observation of interplay between phonon chirality and electronic band topology,” *Science advances* **9** (50), ead4074.
- Higgins, Julia S, and Ann Maconnachie (1986), “Neutron scattering,” *Polymers in Solution* **2** (3), 183.
- Hu, Lun-Hui, Jiabin Yu, Ion Garate, and Chao-Xing Liu (2021), “Phonon helicity induced by electronic berry curvature in Dirac materials,” *Physical review letters* **127** (12), 125901.
- Huang, F F, P. Zhou, W. Q. Li, S. D. He, R. Tan, Z. S. Ma, and L. Z. Sun (2023), “Phononic second-order topological phase in the C_3N compound,” *Phys. Rev. B* **107** (13), 134104.
- Huang, Shin-Ming, Su-Yang Xu, Ilya Belopolski, Chi-Cheng Lee, Guoqing Chang, BaoKai Wang, Nasser Alidoust, Guang Bian, Madhab Neupane, Chenglong Zhang, *et al.* (2015), “A Weyl Fermion semimetal with surface Fermi arcs in the transition metal monophosphide TaAs class,” *Nature communications* **6** (1), 7373.
- Huber, Sebastian D (2016a), “Topological mechanics,” *Nature Physics* **12** (7), 621–623.
- Huber, Sebastian D (2016b), “Topological mechanics,” *Nat. Phys.* **12**, 621–623.
- Ibach, Harald, and Douglas L Mills (2013), *Electron energy loss spectroscopy and surface vibrations* (Academic press).
- Imhof, Stefan, Christian Berger, Florian Bayer, Johannes Brehm, Laurens W Molenkamp, Tobias Kiessling, Frank Schindler, Ching Hua Lee, Martin Greiter, Titus Neupert, *et al.* (2018), “Topolectrical-circuit realization of topological corner modes,” *Nature Physics* **14** (9), 925–929.
- Ishito, Kyosuke, Huiling Mao, Kaya Kobayashi, Yusuke Kousaka, Yoshihiko Togawa, Hiroaki Kusunose, Jun-ichiro Kishine, and Takuya Satoh (2023a), “Chiral phonons: circularly polarized raman spectroscopy and ab initio calculations in a chiral crystal tellurium,” *Chirality* **35** (6), 338–345.
- Ishito, Kyosuke, Huiling Mao, Yusuke Kousaka, Yoshihiko Togawa, Satoshi Iwasaki, Tiantian Zhang, Shuichi Murakami, Jun-ichiro Kishine, and Takuya Satoh (2023b), “Truly chiral phonons in α -hgs,” *Nature Physics* **19** (1), 35–39.
- Ishito, Kyosuke, Huiling Mao, Yusuke Kousaka, Yoshihiko Togawa, Satoshi Iwasaki, Tiantian Zhang, Shuichi Murakami, Jun-ichiro Kishine, and Takuya Satoh (2023c), “Truly chiral phonons in α -hgs,” *Nature Physics* **19** (1), 35–39.
- Jin, Y J, Z. J. Chen, B. W. Xia, Y. J. Zhao, R. Wang, and H. Xu (2018a), “Ideal intersecting nodal-ring phonons in bcc C_8 ,” *Phys. Rev. B* **98** (22), 220103.
- Jin, Yuanjun, Rui Wang, and Hu Xu (2018b), “Recipe for Dirac Phonon States with a Quantized Valley Berry Phase in Two-Dimensional Hexagonal Lattices,” *Nano Lett.* **18** (12), 7755–7760.
- Jin, Zhendong, Biaoyan Hu, Yiran Liu, Yangmu Li, Tiantian Zhang, Kazuki Iida, Kazuya Kamazawa, Alexander I Kolesnikov, Matthew B Stone, Xiangyu Zhang, *et al.* (2022), “Chern numbers of topological phonon band crossing determined with inelastic neutron scattering,” *Physical Review B* **106** (22), 224304.
- Juraschek, Dominik M, Tomáš Neuman, and Prineha Narang (2022), “Giant effective magnetic fields from optically driven chiral phonons in 4 f paramagnets,” *Physical Review Research* **4** (1), 013129.
- Kagan, Yu, and LA Maksimov (2008), “Anomalous Hall effect for the phonon heat conductivity in paramagnetic dielectrics,” *Physical review letters* **100** (14), 145902.
- Kane, C L, and E. J. Mele (2005), “Quantum Spin Hall Effect in Graphene,” *Phys. Rev. Lett.* **95** (22), 226801.
- Kane, Charles L, and Tom C Lubensky (2014), “Topological boundary modes in isostatic lattices,” *Nature Physics* **10** (1), 39–45.
- Kargarian, Mehdi, Mohit Randeria, and Yuan-Ming Lu (2016), “Are the surface fermi arcs in Dirac semimetals topologically protected?” *Proceedings of the National Academy of Sciences* **113** (31), 8648–8652.
- Kasahara, Yuichi, Tsuneya Ohnishi, Yuta Mizukami, Osamu Tanaka, Sixiao Ma, Kaori Sugii, Nobuyuki Kurita, Hidekazu Tanaka, Joji Nasu, Yukitoshi Motome, *et al.* (2018), “Majorana quantization and half-integer thermal quantum Hall effect in a kitaev spin liquid,” *Nature* **559** (7713), 227–231.
- Khanikaev, Alexander B, S Hossein Mousavi, Wang-Kong Tse, Mehdi Kargarian, Allan H MacDonald, and Gennady Shvets (2013), “Photonic topological insulators,” *Nature materials* **12** (3), 233–239.
- Khanikaev, Alexander B, and Gennady Shvets (2017), “Two-dimensional topological photonics,” *Nature photonics* **11** (12), 763–773.
- Kim, Heejae, Hengbin Cheng, Ling Lu, and Shuichi Murakami (2021), “Theoretical analysis of glide- z 2 magnetic topological photonic crystals,” *Optics Express* **29** (20), 31164–31178.
- Kim, Kyunghoon, Eric Vetter, Liang Yan, Cong Yang, Ziqi Wang, Rui Sun, Yu Yang, Andrew H Comstock, Xiao Li, Jun Zhou, *et al.* (2023), “Chiral-phonon-activated spin seebeck effect,” *Nature Materials* **22** (3), 322–328.
- King-Smith, R D, and David Vanderbilt (1993), “Theory of polarization of crystalline solids,” *Phys. Rev. B* **47** (3), 1651–1654(R).
- Kishine, J, AS Ovchinnikov, and AA Tereshchenko (2020), “Chirality-induced phonon dispersion in a noncentrosymmetric

- micropolar crystal,” *Physical Review Letters* **125** (24), 245302.
- Kitaev, Alexei (2009), “Periodic table for topological insulators and superconductors,” in *AIP conference proceedings*, Vol. 1134 (American Institute of Physics) pp. 22–30.
- Kittel, Charles, and Paul McEuen (2018), *Introduction to solid state physics* (John Wiley & Sons).
- Koch, Martin, Daniel M Mittleman, Jan Ornik, and Enrique Castro-Camus (2023), “Terahertz time-domain spectroscopy,” *Nature Reviews Methods Primers* **3** (1), 48.
- Kojevnikov, Alexei B (2004), *Stalin’s great science: The times and adventures of Soviet physicists*, Vol. 2 (World Scientific).
- Komiyama, Hisayoshi, and Shuichi Murakami (2021), “Universal features of canonical phonon angular momentum without time-reversal symmetry,” *Physical Review B* **103** (21), 214302.
- Komiyama, Hisayoshi, Tiantian Zhang, and Shuichi Murakami (2022), “Physics of phonons in systems with approximate screw symmetry,” *Physical Review B* **106** (18), 184104.
- Kong, Mingran, Shuichi Murakami, and Tiantian Zhang (2022), “A comprehensive study of complex non-adiabatic exciton dynamics in mosi_2n_4 ,” *Materials Today Physics* **27**, 100814.
- Kotani, Akio, and Shik Shin (2001), “Resonant inelastic x-ray scattering spectra for electrons in solids,” *Reviews of Modern Physics* **73** (1), 203.
- Kruthoff, Jorrit, Jan De Boer, Jasper Van Wezel, Charles L Kane, and Robert-Jan Slager (2017), “Topological classification of crystalline insulators through band structure combinatorics,” *Physical Review X* **7** (4), 041069.
- Le, Congcong, Xianxin Wu, Shengshan Qin, Yinxian Li, Ronny Thomale, Fu-Chun Zhang, and Jiangping Hu (2018), “Dirac semimetal in β -cui without surface fermi arcs,” *Proceedings of the National Academy of Sciences* **115** (33), 8311–8315.
- Leijnse, Martin, and Karsten Flensberg (2012), “Introduction to topological superconductivity and majorana fermions,” *Semiconductor Science and Technology* **27** (12), 124003.
- Levin, Michael, and Ady Stern (2009), “Fractional topological insulators,” *Physical review letters* **103** (19), 196803.
- Levin, Michael, and Ady Stern (2012), “Classification and analysis of two-dimensional abelian fractional topological insulators,” *Physical Review B—Condensed Matter and Materials Physics* **86** (11), 115131.
- Li, Haoxiang, Tiantian Zhang, A Said, Y Fu, Gilberto Fabbris, Daniel G Mazzone, Jie Zhang, Jason Lapano, Ho Nyung Lee, HC Lei, *et al.* (2021a), “Observation of a chiral wave function in the twofold-degenerate quadruple Weyl system BaPtGe ,” *Physical Review B* **103** (18), 184301.
- Li, Hui, Hongtao He, Hai-Zhou Lu, Huachen Zhang, Hongchao Liu, Rong Ma, Zhiyong Fan, Shun-Qing Shen, and Jiannong Wang (2016), “Negative magnetoresistance in Dirac semimetal Cd_3As_2 ,” *Nature communications* **7** (1), 10301.
- Li, Jiade, Jiangxu Li, Jilin Tang, Zhiyu Tao, Siwei Xue, Jiaxi Liu, Hailin Peng, Xing-Qiu Chen, Jiandong Guo, and Xuetao Zhu (2023a), “Direct observation of topological phonons in graphene,” *Physical Review Letters* **131** (11), 116602.
- Li, Jiangxu, Jiaxi Liu, Stanley A Baronett, Mingfeng Liu, Lei Wang, Ronghan Li, Yun Chen, Dianzhong Li, Qiang Zhu, and Xing-Qiu Chen (2021b), “Computation and data driven discovery of topological phononic materials,” *Nature communications* **12** (1), 1204.
- Li, Jiangxu, Jiaxi Liu, Stanley A. Baronett, Mingfeng Liu, Lei Wang, Ronghan Li, Yun Chen, Dianzhong Li, Qiang Zhu, and Xing-Qiu Chen (2021c), “Computation and data driven discovery of topological phononic materials,” *Nat. Commun.* **12** (1204), 1–12.
- Li, Jiangxu, Lei Wang, Jiaxi Liu, Ronghan Li, Zhenyu Zhang, and Xing-Qiu Chen (2020a), “Topological phonons in graphene,” *Phys. Rev. B* **101** (8), 081403.
- Li, Jiangxu, Qing Xie, Jiaxi Liu, Ronghan Li, Min Liu, Lei Wang, Dianzhong Li, Yiyi Li, and Xing-Qiu Chen (2020b), “Phononic Weyl nodal straight lines in MgB_2 ,” *Phys. Rev. B* **101** (2), 024301.
- Li, Jiangxu, Qing Xie, Jiaxi Liu, Ronghan Li, Min Liu, Lei Wang, Dianzhong Li, Yiyi Li, and Xing-Qiu Chen (2020c), “Phononic Weyl nodal straight lines in mgB_2 ,” *Physical Review B* **101** (2), 024301.
- Li, Jiangxu, Qing Xie, Sami Ullah, Ronghan Li, Hui Ma, Dianzhong Li, Yiyi Li, and Xing-Qiu Chen (2018), “Coexistent three-component and two-component Weyl phonons in TiS , ZrSe , and hTe ,” *Physical Review B* **97** (5), 054305.
- Li, Xiao, Jinxin Zhong, Jinluo Cheng, Hao Chen, Huiqian Wang, Jun Liu, Dali Sun, Lifa Zhang, and Jun Zhou (2024), “Chiral phonon activated spin seebeck effect in chiral materials,” *Science China Physics, Mechanics & Astronomy* **67** (3), 237511.
- Li, Xiaokang, Benoît Fauqué, Zengwei Zhu, and Kamran Behnia (2020d), “Phonon thermal Hall effect in strontium titanate,” *Physical review letters* **124** (10), 105901.
- Li, Xiaokang, Yo Machida, Alaska Subedi, Zengwei Zhu, Liang Li, and Kamran Behnia (2023b), “The phonon thermal Hall angle in black phosphorus,” *Nature Communications* **14** (1), 1027.
- Lin, C, Tao Fang, Zhang Tai-yong, Niu Shi-wen, Gou Cheng, and Shi Zhong-jian (1985), “A study of acoustical activity of $\text{BiPb}_2\text{GeO}_{10}$,” *Solid state communications* **54** (9), 803–806.
- Liu, Chao-Xing, Xiao-Liang Qi, Xi Dai, Zhong Fang, and Shou-Cheng Zhang (2008), “Quantum anomalous Hall effect in $\text{Hg}_{1-y}\text{Mn}_y\text{Te}$ quantum wells,” *Physical review letters* **101** (14), 146802.
- Liu, Chao-Xing, Shou-Cheng Zhang, and Xiao-Liang Qi (2016), “The quantum anomalous Hall effect: theory and experiment,” *Annual Review of Condensed Matter Physics* **7** (1), 301–321.
- Liu, Guang, Yuanjun Jin, Zhongjia Chen, and Hu Xu (2021a), “Symmetry-enforced straight nodal-line phonons,” *Phys. Rev. B* **104** (2), 024304.
- Liu, Jian, Wenjie Hou, En Wang, Shengjie Zhang, Jia-Tao Sun, and Sheng Meng (2019), “Ideal type-II Weyl phonons in wurtzite CuI ,” *Physical Review B* **100** (8), 081204.
- Liu, Jian-Wei, Fu-Long Shi, Xin-Tao He, Guo-Jing Tang, Wen-Jie Chen, Xiao-Dong Chen, and Jian-Wen Dong (2021b), “Valley photonic crystals,” *Advances in Physics: X* **6** (1), 1905546.
- Liu, Qing-Bo, Hua-Hua Fu, and Ruqian Wu (2021c), “Topological phononic nodal hexahedron net and nodal links in the high-pressure phase of the semiconductor CuCl ,” *Phys. Rev. B* **104** (4), 045409.
- Liu, Qing-Bo, Yuting Qian, Hua-Hua Fu, and Zhijun Wang (2020a), “Symmetry-enforced Weyl phonons,” *npj Computational Materials* **6** (1), 95.
- Liu, Qing-Bo, Zhe-Qi Wang, and Hua-Hua Fu (2021d), “Ideal topological nodal-surface phonons in RbTeAu -family materials,” *Phys. Rev. B* **104** (4), L041405.
- Liu, Qing-Bo, Zhijun Wang, and Hua-Hua Fu (2021e), “Charge-four Weyl phonons,” *Physical Review B* **103** (16), L161303.
- Liu, Yizhou, Xiaobin Chen, and Yong Xu (2020b), “Topological phononics: from fundamental models to real materials,” *Advanced Functional Materials* **30** (8), 1904784.
- Liu, Yizhou, Chao-Sheng Lian, Yang Li, Yong Xu, and Wenhui Duan (2017a), “Pseudospins and topological effects of phonons in a kékulé lattice,” *Physical review letters* **119** (25), 255901.
- Liu, Yizhou, Yong Xu, and Wenhui Duan (2018), “Berry phase and topological effects of phonons,” *National Science Review* **5** (3), 314–316.
- Liu, Yizhou, Yong Xu, Shou-Cheng Zhang, and Wenhui Duan (2017b), “Model for topological phononics and phonon diode,” *Physical Review B* **96** (6), 064106.

- Liu, Yizhou, Nianlong Zou, Sibao Zhao, Xiaobin Chen, Yong Xu, and Wenhui Duan (2022), “Ubiquitous Topological States of Phonons in Solids: Silicon as a Model Material,” *Nano Lett.* **22** (5), 2120–2126.
- Liu, ZK, Jianzhong Jiang, Bo Zhou, ZJ Wang, Yi Zhang, HM Weng, Dharmalingam Prabhakaran, Sung Kwan Mo, Han Peng, Pavel Dudin, *et al.* (2014a), “A stable three-dimensional topological Dirac semimetal Cd₃As₂,” *Nature materials* **13** (7), 677–681.
- Liu, ZK, Bo Zhou, Yong Zhang, ZJ Wang, HM Weng, Dharmalingam Prabhakaran, S-K Mo, ZX Shen, Zhong Fang, Xi Dai, *et al.* (2014b), “Discovery of a three-dimensional topological Dirac semimetal, na₃bi,” *Science* **343** (6173), 864–867.
- Lu, Jiuyang, Chunyin Qiu, Weiye Deng, Xueqin Huang, Feng Li, Fan Zhang, Shuqi Chen, and Zhengyou Liu (2018), “Valley topological phases in bilayer sonic crystals,” *Physical review letters* **120** (11), 116802.
- Lu, Ling, Chen Fang, Liang Fu, Steven G Johnson, John D Joannopoulos, and Marin Soljačić (2016a), “Symmetry-protected topological photonic crystal in three dimensions,” *Nature Physics* **12** (4), 337–340.
- Lu, Ling, John D Joannopoulos, and Marin Soljačić (2014), “Topological photonics,” *Nature photonics* **8** (11), 821–829.
- Lu, Ling, John D Joannopoulos, and Marin Soljačić (2016b), “Topological states in photonic systems,” *Nature Physics* **12** (7), 626–629.
- Lu, Ling, Zhiyu Wang, Dexin Ye, Lixin Ran, Liang Fu, John D Joannopoulos, and Marin Soljačić (2015), “Experimental observation of Weyl points,” *Science* **349** (6248), 622–624.
- Luo, Kaifa, and Xi Dai (2023), “Transverse peierls transition,” *Physical Review X* **13** (1), 011027.
- Luo, Kaifa, Rui Yu, and Hongming Weng (2018), “Topological nodal states in circuit lattice,” *Research*.
- Lv, BQ, T Qian, and H Ding (2021), “Experimental perspective on three-dimensional topological semimetals,” *Reviews of Modern Physics* **93** (2), 025002.
- Lv, BQ, HM Weng, BB Fu, X Ps Wang, Hu Miao, Junzhang Ma, P Richard, XC Huang, LX Zhao, GF Chen, *et al.* (2015a), “Experimental discovery of Weyl semimetal TaAs,” *Physical Review X* **5** (3), 031013.
- Lv, BQ, N Xu, HM Weng, JZ Ma, P Richard, XC Huang, LX Zhao, GF Chen, CE Matt, F Bisti, *et al.* (2015b), “Observation of Weyl nodes in TaAs,” *Nature Physics* **11** (9), 724–727.
- Ma, Da-Shuai, Kejun Yu, Xiao-Ping Li, Xiaoyuan Zhou, and Rui Wang (2023), “Obstructed atomic insulators with robust corner modes,” *Physical Review B* **108** (10), L100101.
- Ma, Guancong, Meng Xiao, and C. T. Chan (2019a), “Topological phases in acoustic and mechanical systems,” *Nat. Rev. Phys.* **1**, 281–294.
- Ma, Guancong, Meng Xiao, and Che Ting Chan (2019b), “Topological phases in acoustic and mechanical systems,” *Nature Reviews Physics* **1** (4), 281–294.
- Maciejko, Joseph, and Gregory A Fiete (2015), “Fractionalized topological insulators,” *Nature Physics* **11** (5), 385–388.
- Mangeolle, Léo, Leon Balents, and Lucile Savary (2022), “Phonon thermal Hall conductivity from scattering with collective fluctuations,” *Physical Review X* **12** (4), 041031.
- Mankovsky, Sergiy, Svitlana Polesya, Hannah Lange, Markus Weissenhofer, Ulrich Nowak, and Hubert Ebert (2022), “Angular momentum transfer via relativistic spin-lattice coupling from first principles,” *Physical Review Letters* **129** (6), 067202.
- McClarty, Paul A (2022), “Topological magnons: A review,” *Annual Review of Condensed Matter Physics* **13** (1), 171–190.
- McLellan, AG (1988), “Angular momentum states for phonons and a rotationally invariant development of lattice dynamics,” *Journal of Physics C: Solid State Physics* **21** (7), 1177.
- Miao, H, J. Bouaziz, G. Fabbri, W. R. Meier, F. Z. Yang, H. X. Li, C. Nelson, E. Vescovo, S. Zhang, A. D. Christianson, H. N. Lee, Y. Zhang, C. D. Batista, and S. Blügel (2024), “Spontaneous chirality flipping in an orthogonal spin-charge ordered topological magnet,” *Phys. Rev. X* **14**, 011053.
- Miao, H, T. T. Zhang, L. Wang, D. Meyers, A. H. Said, Y. L. Wang, Y. G. Shi, H. M. Weng, Z. Fang, and M. P. M. Dean (2018), “Observation of Double Weyl Phonons in Parity-Breaking FeSi,” *Phys. Rev. Lett.* **121** (3), 035302.
- Michel, L, and J. Zak (2001), “Elementary energy bands in crystals are connected,” *Phys. Rep.* **341** (1), 377–395.
- Migliori, Albert (2016), *Resonant ultrasound spectroscopy*, Tech. Rep. (Los Alamos National Laboratory (LANL), Los Alamos, NM (United States)).
- Moore, Joel E (2010), “The birth of topological insulators,” *Nature* **464** (7286), 194–198.
- Mu, Haimen, Bing Liu, Tianyi Hu, and Zhengfei Wang (2022), “Kekulé Lattice in Graphdiyne: Coexistence of Phononic and Electronic Second-Order Topological Insulator,” *Nano Lett.* **22** (3), 1122–1128.
- Murakami, Shuichi (2007), “Phase transition between the quantum spin Hall and insulator phases in 3d: emergence of a topological gapless phase,” *New Journal of Physics* **9** (9), 356.
- Naaman, Ron, Yossi Paltiel, and David H Waldeck (2019), “Chiral molecules and the electron spin,” *Nature Reviews Chemistry* **3** (4), 250–260.
- Naaman, Ron, and David H Waldeck (2012), “Chiral-induced spin selectivity effect,” *The journal of physical chemistry letters* **3** (16), 2178–2187.
- Nash, Lisa M, Dustin Kleckner, Alismari Read, Vincenzo Vitelli, Ari M Turner, and William TM Irvine (2015), “Topological mechanics of gyroscopic metamaterials,” *Proceedings of the National Academy of Sciences* **112** (47), 14495–14500.
- Neupane, Madhab, Su-Yang Xu, Raman Sankar, Nasser Alidoust, Guang Bian, Chang Liu, Ilya Belopolski, Tay-Rong Chang, Horng-Tay Jeng, Hsin Lin, *et al.* (2014), “Observation of a three-dimensional topological Dirac semimetal phase in high-mobility Cd₃As₂,” *Nature communications* **5** (1), 3786.
- Ningyuan, Jia, Clai Owens, Ariel Sommer, David Schuster, and Jonathan Simon (2015), “Time- and site-resolved dynamics in a topological circuit,” *Physical Review X* **5** (2), 021031.
- Nova, Tobia F, Andrea Cartella, Alice Cantaluppi, Michael Först, Davide Bossini, Rostislav V Mikhaylovskiy, Aleksei V Kimel, Roberto Merlin, and Andrea Caviglioli (2017), “An effective magnetic field from optically driven phonons,” *Nature Physics* **13** (2), 132–136.
- Ohe, Kazuki, Hiroaki Shishido, Masaki Kato, Shoyo Utsumi, Hiroyasu Matsuura, and Yoshihiko Togawa (2024), “Chirality-induced selectivity of phonon angular momenta in chiral quartz crystals,” *Physical Review Letters* **132** (5), 056302.
- Oshikawa, Masaki, and T Senthil (2006), “Fractionalization, topological order, and quasiparticle statistics,” *Physical review letters* **96** (6), 060601.
- Owerre, SA (2016), “A first theoretical realization of honeycomb topological magnon insulator,” *Journal of Physics: Condensed Matter* **28** (38), 386001.
- Ozawa, Tomoki, Hannah M Price, Alberto Amo, Nathan Goldman, Mohammad Hafezi, Ling Lu, Mikael C Rechtsman, David Schuster, Jonathan Simon, Oded Zilberberg, *et al.* (2019), “Topological photonics,” *Reviews of Modern Physics* **91** (1), 015006.
- Pal, Palash B (2011), “Dirac, majorana, and Weyl fermions,” *American Journal of Physics* **79** (5), 485–498.

- Pal, Raj Kumar, Marshall Schaeffer, and Massimo Ruzzene (2016), “Helical edge states and topological phase transitions in phononic systems using bi-layered lattices,” *J. Appl. Phys.* **119** (8), 084305.
- Pan, Mingxiang, and Huaqing Huang (2022), “Phononic Stiefel-Whitney topology with corner vibrational modes in two-dimensional Xenos and ligand-functionalized derivatives,” *Phys. Rev. B* **106** (20), L201406.
- Park, Sungjoon, Yoonseok Hwang, Hong Chul Choi, and Bohm-Jung Yang (2021), “Topological acoustic triple point,” *Nat. Commun.* **12** (6781), 1–9.
- Peters, Laurens DM, Tanner Culpitt, Erik I Tellgren, and Trygve Helgaker (2022), “Magnetic-translational sum rule and approximate models of the molecular berry curvature,” *The Journal of Chemical Physics* **157** (13).
- Po, Hoi Chun, Ashvin Vishwanath, and Haruki Watanabe (2017), “Symmetry-based indicators of band topology in the 230 space groups,” *Nature communications* **8** (1), 50.
- Prodan, Emil, and Camelia Prodan (2009a), “Topological Phonon Modes and Their Role in Dynamic Instability of Microtubules,” *Phys. Rev. Lett.* **103** (24), 248101.
- Prodan, Emil, and Camelia Prodan (2009b), “Topological phonon modes and their role in dynamic instability of microtubules,” *Physical review letters* **103** (24), 248101.
- Qi, Xiao-Liang, and Shou-Cheng Zhang (2010a), “The quantum spin Hall effect and topological insulators,” *Physics Today* **63** (1), 33–38.
- Qi, Xiao-Liang, and Shou-Cheng Zhang (2010b), “The quantum spin Hall effect and topological insulators,” *Phys. Today* **63** (1), 33–38.
- Qi, Xiao-Liang, and Shou-Cheng Zhang (2011), “Topological insulators and superconductors,” *Rev. Mod. Phys.* **83** (4), 1057–1110.
- Qian, Shifeng, Yongpan Li, and Cheng-Cheng Liu (2023), “Stable higher-order topological Dirac semimetals with $z/2$ monopole charge in alternating-twist multilayer graphene and beyond,” *Physical Review B* **108** (24), L241406.
- Qin, Peiyao, Guang Liu, Peng Wu, and Hu Xu (2024), “Diverse degeneracy types in topological phonons: A perspective,” *Appl. Phys. Lett.* **124** (3), 10.1063/5.0186917.
- Qin, Tao, Jianhui Zhou, and Junren Shi (2012), “Berry curvature and the phonon Hall effect,” *Physical Review B—Condensed Matter and Materials Physics* **86** (10), 104305.
- Raghu, Srinivas, and Frederick Duncan Michael Haldane (2008), “Analogues of quantum-Hall-effect edge states in photonic crystals,” *Physical Review A—Atomic, Molecular, and Optical Physics* **78** (3), 033834.
- Ray, K, SP Ananthavel, DH Waldeck, and Ron Naaman (1999), “Asymmetric scattering of polarized electrons by organized organic films of chiral molecules,” *Science* **283** (5403), 814–816.
- Rebane, Yu T (1983), “Faraday effect produced in the residual ray region by the magnetic moment of an optical phonon in an ionic crystal,” *Zh. Eksp. Teor. Fiz* **84**, 2323.
- Ren, Yafei, Cong Xiao, Daniyar Saparov, and Qian Niu (2021), “Phonon magnetic moment from electronic topological magnetization,” *Physical review letters* **127** (18), 186403.
- Romao, Carl P, Riccardo Catena, Nicola A Spaldin, and Marek Matas (2023), “Chiral phonons as dark matter detectors,” *Physical Review Research* **5** (4), 043262.
- Romao, Carl P, and Dominik M Juraschek (2024), “Phonon-induced geometric chirality,” *ACS nano* **18** (43), 29550–29557.
- Ryu, Shinsei, Andreas P Schnyder, Akira Furusaki, and Andreas WW Ludwig (2010), “Topological insulators and superconductors: tenfold way and dimensional hierarchy,” *New Journal of Physics* **12** (6), 065010.
- Saparov, Daniyar, Bangguo Xiong, Yafei Ren, and Qian Niu (2022), “Lattice dynamics with molecular berry curvature: Chiral optical phonons,” *Physical Review B* **105** (6), 064303.
- Sato, Masatoshi, and Yoichi Ando (2017), “Topological superconductors: a review,” *Reports on Progress in Physics* **80** (7), 076501.
- Schaack, Gerhard (1976), “Observation of circularly polarized phonon states in an external magnetic field,” *Journal of Physics C: Solid State Physics* **9** (11), L297.
- Senthil, T, and Matthew PA Fisher (2001a), “Fractionalization in the cuprates: Detecting the topological order,” *Physical review letters* **86** (2), 292.
- Senthil, Todadri, and Matthew PA Fisher (2001b), “Fractionalization, topological order, and cuprate superconductivity,” *Physical Review B* **63** (13), 134521.
- Seradjeh, Babak, JE Moore, and Marcel Franz (2009), “Exciton condensation and charge fractionalization in a topological insulator film,” *Physical review letters* **103** (6), 066402.
- Shen, Shun-Qing (2012), *Topological insulators*, Vol. 174 (Springer).
- Sheng, L, DN Sheng, and CS Ting (2006), “Theory of the phonon Hall effect in paramagnetic dielectrics,” *Physical review letters* **96** (15), 155901.
- Shiozaki, Ken, and Masatoshi Sato (2014), “Topology of crystalline insulators and superconductors,” *Physical Review B* **90** (16), 165114.
- Shirley, Wilbur, Kevin Slagle, and Xie Chen (2019), “Fractional excitations in foliated fracton phases,” *Annals of Physics* **410**, 167922.
- Singh, Sobhit, QuanSheng Wu, Changming Yue, Aldo H. Romero, and Alexey A. Soluyanov (2018), “Topological phonons and thermoelectricity in triple-point metals,” *Phys. Rev. Mater.* **2** (11), 114204.
- Song, Hao, and Michael Hermele (2015), “Space-group symmetry fractionalization in a family of exactly solvable models with $z/2$ topological order,” *Physical Review B* **91** (1), 014405.
- Song, Zhida, Tiantian Zhang, and Chen Fang (2018), “Diagnosis for nonmagnetic topological semimetals in the absence of spin-orbital coupling,” *Physical Review X* **8** (3), 031069.
- Stern, Ady (2016), “Fractional topological insulators: a pedagogical review,” *Annual Review of Condensed Matter Physics* **7** (1), 349–368.
- Stupakiewicz, A, CS Davies, K Szerenos, D Afanasiev, KS Rabinovich, AV Boris, Andrea Caviglia, AV Kimel, and A Kirilyuk (2021), “Ultrafast phononic switching of magnetization,” *Nature Physics* **17** (4), 489–492.
- Su, Zhaoxian, Wenlong Gao, Bingyi Liu, Lingling Huang, and Yongtian Wang (2022), “Three-dimensional Dirac semimetal metamaterial enabled by negative couplings,” *New Journal of Physics* **24** (3), 033025.
- Sun, Kai, and Xiaoming Mao (2021), “Fractional excitations in non-euclidean elastic plates,” *Physical Review Letters* **127** (9), 098001.
- Süsstrunk, Roman, and Sebastian D Huber (2015), “Observation of phononic helical edge states in a mechanical topological insulator,” *Science* **349** (6243), 47–50.
- Süsstrunk, Roman, and Sebastian D. Huber (2016), “Classification of topological phonons in linear mechanical metamaterials,” *Proc. Natl. Acad. Sci. U.S.A.* **113** (33), E4767–E4775.
- Tang, Feng, Hoi Chun Po, Ashvin Vishwanath, and Xiangang Wan (2019a), “Comprehensive search for topological materials using symmetry indicators,” *Nature* **566** (7745), 486–489.
- Tang, Feng, Hoi Chun Po, Ashvin Vishwanath, and Xiangang Wan (2019b), “Comprehensive search for topological materials using symmetry indicators,” *Nature* **566**, 486–489.

- Tang, Feng, Hoi Chun Po, Ashvin Vishwanath, and Xiangang Wan (2019c), “Efficient topological materials discovery using symmetry indicators,” *Nat. Phys.* **15**, 470–476.
- Tang, Feng, Hoi Chun Po, Ashvin Vishwanath, and Xiangang Wan (2019d), “Topological materials discovery by large-order symmetry indicators,” *Sci. Adv.* **5** (3), 10.1126/sciadv.aau8725.
- Tang, Feng, and Xiangang Wan (2024), “Group-theoretical study of band nodes and the emanating nodal structures in crystalline materials,” *Quantum Front.* **3** (1), 1–20.
- Tauchert, Sonja R, Mikhail Volkov, Dominik Ehberger, D Kazenwadel, Martin Evers, Hannah Lange, Andreas Donges, Alexander Book, W Kreuzpaintner, U Nowak, *et al.* (2022), “Polarized phonons carry angular momentum in ultrafast demagnetization,” *Nature* **602** (7895), 73–77.
- Thouless, D J, M. Kohmoto, M. P. Nightingale, and M. Den Nijs (1982a), “Quantized Hall Conductance in a Two-Dimensional Periodic Potential,” *Phys. Rev. Lett.* **49** (6), 405–408.
- Thouless, David J, Mahito Kohmoto, M Peter Nightingale, and Marcel den Nijs (1982b), “Quantized Hall conductance in a two-dimensional periodic potential,” *Physical review letters* **49** (6), 405.
- Tokura, Yoshinori, Kenji Yasuda, and Atsushi Tsukazaki (2019), “Magnetic topological insulators,” *Nature Reviews Physics* **1** (2), 126–143.
- Tsirkín, Stepan S, Ivo Souza, and David Vanderbilt (2017), “Composite Weyl nodes stabilized by screw symmetry with and without time-reversal invariance,” *Physical Review B* **96** (4), 045102.
- Ueda, Hiroki, Mirian García-Fernández, Stefano Agrestini, Carl P. Romao, Jeroen van den Brink, Nicola A. Spaldin, Ke-Jin Zhou, and Urs Staub (2023), “Chiral phonons in quartz probed by x-rays,” *Nature* **618** (7967), 946–950.
- Vaezi, Abolhassan (2013), “Fractional topological superconductor with fractionalized majorana fermions,” *Physical Review B—Condensed Matter and Materials Physics* **87** (3), 035132.
- Vergniory, M G, L. Elcoro, Claudia Felser, Nicolas Regnault, B. Andrei Bernevig, and Zhijun Wang (2019a), “A complete catalogue of high-quality topological materials,” *Nature* **566**, 480–485.
- Vergniory, MG, L Elcoro, Claudia Felser, Nicolas Regnault, B Andrei Bernevig, and Zhijun Wang (2019b), “A complete catalogue of high-quality topological materials,” *Nature* **566** (7745), 480–485.
- Wan, Xiangang, Ari M Turner, Ashvin Vishwanath, and Sergey Y Savrasov (2011), “Topological semimetal and fermi-arc surface states in the electronic structure of pyrochlore iridates,” *Physical Review B—Condensed Matter and Materials Physics* **83** (20), 205101.
- Wang, Pai, Ling Lu, and Katia Bertoldi (2015a), “Topological phononic crystals with one-way elastic edge waves,” *Physical review letters* **115** (10), 104302.
- Wang, Xiaotian, Tie Yang, Zhenxiang Cheng, Gokhan Surucu, Jianhua Wang, Feng Zhou, Zeying Zhang, and Gang Zhang (2022), “Topological nodal line phonons: Recent advances in materials realization,” *Applied Physics Reviews* **9** (4).
- Wang, Yao-Ting, Pi-Gang Luan, and Shuang Zhang (2015b), “Coriolis force induced topological order for classical mechanical vibrations,” *New J. Phys.* **17** (7), 073031.
- Wang, Zhijun, Yan Sun, Xing-Qiu Chen, Cesare Franchini, Gang Xu, Hongming Weng, Xi Dai, and Zhong Fang (2012), “Dirac semimetal and topological phase transitions in a 3 bi ($a = na, k, rb$),” *Physical Review B—Condensed Matter and Materials Physics* **85** (19), 195320.
- Wang, Zhijun, Hongming Weng, Quansheng Wu, Xi Dai, and Zhong Fang (2013), “Three-dimensional Dirac semimetal and quantum transport in $cd\ 3\ as\ 2$,” *Physical Review B—Condensed Matter and Materials Physics* **88** (12), 125427.
- Wen, Xiao-Gang (1995), “Topological orders and edge excitations in fractional quantum Hall states,” *Advances in Physics* **44** (5), 405–473.
- Weng, Hongming, Chen Fang, Zhong Fang, B Andrei Bernevig, and Xi Dai (2015), “Weyl semimetal phase in noncentrosymmetric transition-metal monophosphides,” *Physical Review X* **5** (1), 011029.
- Wolf, Yotam, Yizhou Liu, Jiewen Xiao, Noejung Park, and Binghai Yan (2022), “Unusual spin polarization in the chirality-induced spin selectivity,” *ACS nano* **16** (11), 18601–18607.
- Wu, Fangliang, Song Bao, Jing Zhou, Yunlong Wang, Jian Sun, Jinsheng Wen, Yuan Wan, and Qi Zhang (2023), “Fluctuation-enhanced phonon magnetic moments in a polar antiferromagnet,” *Nature Physics* **19** (12), 1868–1875.
- Wu, Long-Hua, and Xiao Hu (2015), “Scheme for Achieving a Topological Photonic Crystal by Using Dielectric Material,” *Phys. Rev. Lett.* **114** (22), 223901.
- Wu, Xiaoxiao, Yan Meng, Jingxuan Tian, Yingzhou Huang, Hong Xiang, Dezhan Han, and Weijia Wen (2017), “Direct observation of valley-polarized topological edge states in designer surface plasmon crystals,” *Nature communications* **8** (1), 1304.
- Xia, Baizhan, Jie Zhang, Liang Tong, Shengjie Zheng, and Xianfeng Man (2022), “Topologically valley-polarized edge states in elastic phononic plates yielded by lattice defects,” *International Journal of Solids and Structures* **239**, 111413.
- Xia, BW, R Wang, ZJ Chen, YJ Zhao, and Hu Xu (2019), “Symmetry-protected ideal type-ii Weyl phonons in $cdte$,” *Physical review letters* **123** (6), 065501.
- Xiao, Di, Ming-Che Chang, and Qian Niu (2010), “Berry phase effects on electronic properties,” *Rev. Mod. Phys.* **82** (3), 1959–2007.
- Xiao, Meng, and Shanhui Fan (2017), “Topologically charged nodal surface,” *arXiv preprint arXiv:1709.02363*.
- Xiao, Meng, Guancong Ma, Zhiyu Yang, Ping Sheng, Z. Q. Zhang, and C. T. Chan (2015), “Geometric phase and band inversion in periodic acoustic systems,” *Nat. Phys.* **11**, 240–244.
- Xie, Chengwu, Hongkuan Yuan, Ying Liu, and Xiaotian Wang (2022), “Two-nodal surface phonons in solid-state materials,” *Phys. Rev. B* **105** (5), 054307.
- Xie, Chengwu, Hongkuan Yuan, Ying Liu, Xiaotian Wang, and Gang Zhang (2021), “Three-nodal surface phonons in solid-state materials: Theory and material realization,” *Phys. Rev. B* **104** (13), 134303.
- Xiong, Jun, Satya K Kushwaha, Tian Liang, Jason W Krizan, Max Hirschberger, Wudi Wang, Robert Joseph Cava, and Nai Phuan Ong (2015), “Evidence for the chiral anomaly in the Dirac semimetal na_3bi ,” *Science* **350** (6259), 413–416.
- Xu, Mingran, Jorge Puebla, Florent Auvray, Bivas Rana, Kouta Kondou, and Yoshichika Otani (2018), “Inverse edelstein effect induced by magnon-phonon coupling,” *Physical Review B* **97** (18), 180301.
- Xu, Su-Yang, Ilya Belopolski, Nasser Alidoust, Madhab Neupane, Guang Bian, Chenglong Zhang, Raman Sankar, Guoqing Chang, Zhujun Yuan, Chi-Cheng Lee, *et al.* (2015), “Discovery of a Weyl fermion semimetal and topological fermi arcs,” *Science* **349** (6248), 613–617.
- Xu, Yong, Zhongxue Gan, and Shou-Cheng Zhang (2014), “Enhanced Thermoelectric Performance and Anomalous Seebeck Effects in Topological Insulators,” *Phys. Rev. Lett.* **112** (22), 226801.
- Xu, Yuanfeng, Luis Elcoro, Zhi-Da Song, Benjamin J. Wieder, M. G. Vergniory, Nicolas Regnault, Yulin Chen, Claudia Felser, and B. Andrei Bernevig (2020), “High-throughput calculations of magnetic topological materials,” *Nature* **586**, 702–707.

- Xu, Yuanfeng, M. G. Vergniory, Da-Shuai Ma, Juan L. Mañes, Zhi-Da Song, B. Andrei Bernevig, Nicolas Regnault, and Luis Elcoro (2024a), “Catalog of topological phonon materials,” *Science* **384**, 6696.
- Xu, Yuanfeng, MG Vergniory, Da-Shuai Ma, Juan L Mañes, Zhi-Da Song, B Andrei Bernevig, Nicolas Regnault, and Luis Elcoro (2024b), “Catalog of topological phonon materials,” *Science* **384** (6696), eadf8458.
- Xue, Haoran, Yihao Yang, and Baile Zhang (2022), “Topological acoustics,” *Nat. Rev. Mater.* **7**, 974–990.
- Xue, Rui, Zhenhua Qiao, Yang Gao, and Qian Niu (2025), “Extrinsic mechanisms of phonon magnetic moment,” arXiv preprint arXiv:2501.03204.
- Yan, Binghai, and Claudia Felser (2017), “Topological materials: Weyl semimetals,” *Annual Review of Condensed Matter Physics* **8** (1), 337–354.
- Yang, FZ, KF Luo, Weizhe Zhang, Xiaoyu Guo, WR Meier, H Ni, HX Li, P Mercado Lozano, G Fabbri, AH Said, *et al.* (2024a), “Incommensurate transverse peierls transition,” arXiv preprint arXiv:2410.10539.
- Yang, R, Y-Y Zhu, M Steigleder, X-G Qiu, T-T Zhang, and M Dressel (2024b), “Inherent circular dichroism of phonons in magnetic Weyl semimetal $\text{Co}_3\text{Sn}_2\text{S}_2$,” arXiv preprint arXiv:2410.21775.
- Yang, Tie, Jianhua Wang, Xiao-Ping Li, Xiaotian Wang, Zhenxiang Cheng, Wenhong Wang, and Gang Zhang (2024c), “Topological nodal-point phononic systems,” *Matter* **7** (2), 320–350.
- Yang, Tie, Chengwu Xie, Hong Chen, Xiaotian Wang, and Gang Zhang (2022), “Phononic nodal points with quadratic dispersion and multifold degeneracy in the cubic compound Ta_3Sn ,” *Phys. Rev. B* **105** (9), 094310.
- Yang, Zhaoju, Fei Gao, Xihang Shi, Xiao Lin, Zhen Gao, Yidong Chong, and Baile Zhang (2015), “Topological acoustics,” *Physical review letters* **114** (11), 114301.
- Yao, Dapeng, and Shuichi Murakami (2024), “Conversion of chiral phonons into magnons in ferromagnets and antiferromagnets,” *Journal of the Physical Society of Japan* **93** (3), 034708.
- Yao, Dapeng, and Shuichi Murakami (2025), “Theory of spin magnetization driven by chiral phonons,” *Physical Review B* **111** (13), 134414.
- Yao, Wang, Di Xiao, and Qian Niu (2008), “Valley-dependent optoelectronics from inversion symmetry breaking,” *Physical Review B—Condensed Matter and Materials Physics* **77** (23), 235406.
- Yi, Hemian, Zhijun Wang, Chaoyu Chen, Youguo Shi, Ya Feng, Aiji Liang, Zhuojin Xie, Shaolong He, Junfeng He, Yingying Peng, *et al.* (2014), “Evidence of topological surface state in three-dimensional Dirac semimetal Cd_3As_2 ,” *Scientific Reports* **4** (1), 6106.
- Yukitake, Taiki, Daisuke Hara, and Shuichi Murakami (2025a), “Double-helical surface states in Dirac semimetals protected by glide-time-reversal symmetry,” arXiv preprint arXiv:2503.11152.
- Yukitake, Taiki, Tiantian Zhang, Daisuke Hara, and Shuichi Murakami (2025b), “Redefinition of Z_2 charge for GT-protected topological semimetals,” to be appear on arXiv.
- Zak, J (1989), “Berry’s phase for energy bands in solids,” *Phys. Rev. Lett.* **62** (23), 2747–2750.
- Zhang, Heda, N Peshcherenko, Fazhi Yang, TZ Ward, P Raghuvanshi, L Lindsay, Claudia Felser, Y Zhang, J-Q Yan, and H Miao (2024a), “Observation of phonon angular momentum,” arXiv preprint arXiv:2409.13462.
- Zhang, Lifa, and Qian Niu (2014), “Angular momentum of phonons and the einstein–de haas effect,” *Phys. Rev. Lett.* **112**, 085503.
- Zhang, Lifa, and Qian Niu (2015), “Chiral phonons at high-symmetry points in monolayer hexagonal lattices,” *Phys. Rev. Lett.* **115**, 115502.
- Zhang, Lifa, Jie Ren, Jian-Sheng Wang, and Baowen Li (2010), “Topological Nature of the Phonon Hall Effect,” *Phys. Rev. Lett.* **105** (22), 225901.
- Zhang, Lifa, Jie Ren, Jian-Sheng Wang, and Baowen Li (2013), “Topological magnon insulator in insulating ferromagnet,” *Physical Review B—Condensed Matter and Materials Physics* **87** (14), 144101.
- Zhang, Qicheng, Daehun Lee, Lu Zheng, Xuejian Ma, Shawn I Meyer, Li He, Han Ye, Ze Gong, Bo Zhen, Keji Lai, *et al.* (2022a), “Gigahertz topological valley Hall effect in nanoelectromechanical phononic crystals,” *Nature Electronics* **5** (3), 157–163.
- Zhang, Ruihan, Haohao Sheng, Junze Deng, Zhong Fang, Zhilong Yang, and Zhijun Wang (2023a), “Unconventional phonon spectra and obstructed edge phonon modes,” *Science China Physics, Mechanics & Astronomy* **67** (4), 246811.
- Zhang, Shuai, Zhiheng Huang, Muchen Du, Tianping Ying, Luojun Du, and Tiantian Zhang (2025a), “The chirality of phonons: Definitions, symmetry constraints, and experimental observation,” arXiv:2503.22794 [cond-mat.mtrl-sci].
- Zhang, Shuai, Kaifa Luo, and Tiantian Zhang (2024b), “Understanding chiral charge-density wave by frozen chiral phonon,” arXiv:2407.08982 [cond-mat.mtrl-sci].
- Zhang, Tiantian, Daisuke Hara, and Shuichi Murakami (2022b), “Z₂ Dirac points with topologically protected multihelical surface states,” *Physical Review Research* **4** (3), 033170.
- Zhang, Tiantian, Zhiheng Huang, Zitian Pan, Luojun Du, Guangyu Zhang, and Shuichi Murakami (2023b), “Weyl phonons in chiral crystals,” *Nano Letters* **23** (16), 7561–7567.
- Zhang, Tiantian, Yi Jiang, Zhida Song, He Huang, Yuqing He, Zhong Fang, Hongming Weng, and Chen Fang (2019a), “Catalogue of topological electronic materials,” *Nature* **566** (7745), 475–479.
- Zhang, Tiantian, Ling Lu, Shuichi Murakami, Zhong Fang, Hongming Weng, and Chen Fang (2020a), “Diagnosis scheme for topological degeneracies crossing high-symmetry lines,” *Physical Review Research* **2** (2), 022066.
- Zhang, Tiantian, and Shuichi Murakami (2021), “Predicting topological materials: symmetry-based indicator theories and beyond,” *Journal of Physics D: Applied Physics* **54** (41), 414002.
- Zhang, Tiantian, and Shuichi Murakami (2022), “Chiral phonons and pseudoangular momentum in nonsymmorphic systems,” *Physical Review Research* **4** (1), L012024.
- Zhang, Tiantian, and Shuichi Murakami (2023), “Parallel and antiparallel helical surface states for topological semimetals,” *Scientific Reports* **13** (1), 9239.
- Zhang, Tiantian, Shuichi Murakami, and Hu Miao (2025b), “Weyl phonons: The connection of topology and chirality,” .
- Zhang, Tiantian, Zhida Song, A. Alexandradinata, Hongming Weng, Chen Fang, Ling Lu, and Zhong Fang (2018a), “Double-Weyl Phonons in Transition-Metal Monosilicides,” *Phys. Rev. Lett.* **120** (1), 016401.
- Zhang, Tiantian, Ryo Takahashi, Chen Fang, and Shuichi Murakami (2020b), “Twofold quadruple Weyl nodes in chiral cubic crystals,” *Physical Review B* **102** (12), 125148.
- Zhang, Tiantian, T Yilmaz, Elio Vescovo, HX Li, Rob G Moore, Ho Nyung Lee, Hu Miao, Shuichi Murakami, and Micheal A McGuire (2022c), “Endless Dirac nodal lines in kagome-metal $\text{Ni}_3\text{In}_2\text{S}_2$,” *npj Computational Materials* **8** (1), 155.
- Zhang, Tingfeng, Tianyi Hu, Yongqi Zhang, and Zhengfei Wang (2023c), “Pseudospin Polarized Dual-Higher-Order Topology in Hydrogen-Substituted Graphdiyne,” *Nano Lett.* **23** (17), 8319–8325.
- Zhang, TT, H Miao, Q Wang, JQ Lin, Y Cao, G Fabbri, AH Said, X Liu, HC Lei, Z Fang, *et al.* (2019b), “Phononic helical nodal lines with PT protection in MoB_2 ,” *Physical Review Letters*

- 123** (24), 245302.
- Zhang, Xiaou, Yinhan Zhang, Satoshi Okamoto, and Di Xiao (2019c), “Thermal Hall effect induced by magnon-phonon interactions,” *Physical review letters* **123** (16), 167202.
- Zhang, Xiu, Lu Zhang, Junzhi Zhu, Tingxiao Qin, Haiyun Huang, Baixu Xiang, Haiyun Liu, and Qihua Xiong (2025c), “Ultrafast chirality-dependent dynamics from helicity-resolved transient absorption spectroscopy,” *Nanoscale*.
- Zhang, Xiujuan, Hai-Xiao Wang, Zhi-Kang Lin, Yuan Tian, Biye Xie, Ming-Hui Lu, Yan-Feng Chen, and Jian-Hua Jiang (2019d), “Second-order topology and multidimensional topological transitions in sonic crystals,” *Nature Physics* **15** (6), 582–588.
- Zhang, Xiujuan, Meng Xiao, Ying Cheng, Ming-Hui Lu, and Johan Christensen (2018b), “Topological sound,” *Communications Physics* **1** (1), 97.
- Zhang, Zhiwang, Ye Tian, Yihe Wang, Shuxiang Gao, Ying Cheng, Xiaojun Liu, and Johan Christensen (2018c), “Directional acoustic antennas based on valley-Hall topological insulators,” *Advanced Materials* **30** (36), 1803229.
- Zheng, Shengjie, Guiju Duan, and Baizhan Xia (2020), “Underwater acoustic positioning based on valley-chirality locked beam of sonic system,” *International Journal of Mechanical Sciences* **174**, 105463.
- Zhong, Mingmin, Ying Liu, Feng Zhou, Minquan Kuang, Tie Yang, Xiaotian Wang, and Gang Zhang (2021), “Coexistence of phononic sixfold, fourfold, and threefold excitations in the ternary antimonide $\text{Zr}_3\text{Ni}_3\text{Sb}_4$,” *Phys. Rev. B* **104** (8), 085118.
- Zhu, Hanyu, Jun Yi, Ming-Yang Li, Jun Xiao, Lifa Zhang, Chih-Wen Yang, Robert A Kaindl, Lain-Jong Li, Yuan Wang, and Xiang Zhang (2018), “Observation of chiral phonons,” *Science* **359** (6375), 579–582.